Online ISSN : 2395-602X
Print ISSN : 2395-6011
www.ijsrst.com

TECHNO SCIENCE ACADEMY
THE INTERNATIONAL OPEN ACCESS PUBLISHER

IJSRST

# International e-Conference on Recent Trends in Nano-Materials and Its Applications

## RTNA-2022

Organized By
Department of Physics,
Sangola Taluka Shetkari Shikshan Prasarak
Mandal Sangola's, Vidnyan Mahavidyalaya, Sangola
Tal-Sangola, Dist-Solapur, MH-413307, India
Collaboration with
Internal Quality Assurance Cell (IQAC)

VOLUME 9, ISSUE 11, MARCH-APRIL-2022

# INTERNATIONAL JOURNAL OF SCIENTIFIC RESEARCH IN SCIENCE AND TECHNOLOGY

Email : editor@ijsrst.com Website : http://ijsrst.com

# International e-Conference on Recent Trends in Nano-Materials and Its Applications
# (RTNA-2022)

**22nd-23rd April, 2022**

Organised by

Department of Physics in Collaboration with Internal Quality Assurance Cell (IQAC)
Sangola Taluka Shetkari Shikshan Prasarak Mandal Sangola's
Vidnyan Mahavidyalaya, Sangola
Tal-Sangola, Dist-Solapur, MH-413307, India
Affiliated to Punyashlok Ahilyadevi Holkar Solapur University,
Solapur, Maharashtra, India
In Association with
International Journal of Scientific Research in Science and Technology

Print ISSN: 2395-6011 Online ISSN : 2395-602X
Volume 9, Issue 11, March-April-2022
International Peer Reviewed, Open Access Journal
Published By
Technoscience Academy
(The International Open Access Publisher)

website: www.technoscienceacademy.com

## Resource Persons

**Prof. Jae Cheol Shin**
Dongguk University,
**South Korea**

**Dr. Sreekanth TVM**
Yeungnam University,
**South Korea**

**Dr. M. Vasudeva Reddy**
Yeungnam University,
**South Korea**

**Dr. Sonaimuthu Mohandoss**
Yeungnam University,
**South Korea**

## Chief Patron

**Hon'ble Mr. Chandrakant Deshmukh**
**Director, STSSPM**

**Hon'ble Mr. Vitthalrao Shinde**
**Secretary, STSSPM**

## Organizing Committee

| | | | |
|---|---|---|---|
| **Dr. R. A. Fule**<br>**(Acting Principal)** | **Mr. B. B. Navale**<br>**(Head of Dept.)** | **Dr. S. S. Dhasade,**<br>**(Convener)** | **Dr. J. V. Thombare**<br>**(Organizing Secretary)** |
| **Mr. A. M. Kambale**<br>**(Treasurer)** | **Dr. D. K. Bandgar**<br>**(Member)** | **Dr. S. M. Mane**<br>**(South Korea)** | **Dr. S. T. Navale**<br>**(Spain)** |

# About US

The Institution,Sangola Taluka Shetkari Shikshan Prasarak Mandal Sangola,was established in 23-Sep-1991,with the aim of giving availibility and facility of education to socially backward society, to Bahujan society including Harijan,Girijan,farmers,labours and socially deprived from progress in the region of sangola taluka since it's establishment, the sansthas has started highschool department,professional cources of +2 section and vidnyan mahavidyalay,etc . vidnyan mahavidyalay was established 23rd septmber 1991. There is the facility of B .C .S,B.C.A (degree cources), Bsc(comp) & Msc education in the college. The college has started M.A (english)cource from the year 2004 & Msc (comp science) from 2009 from 2012 since its establishment the college has been progressing ahead and has now become an importent academic center in the region of sangola taluka the college is accredited by NAAC with Grade "B" in the year 2004 Along with an intellectual & all round development of students, to develop their academic carrier , there are various departments under Arts & Science College faculities During the last year the no. of students in this college were 1600 . The big building of the college , with its large play ground , is near by S.T stand.

# CONTENTS

International e-Conference on Recent Trends in Nano-Materials and Its Applications
In Association with International Journal of Scientific Research in Science and Technology
Volume 9 | Issue 11 | Print ISSN: 2395-6011 | Online ISSN: 2395-602X (www.ijsrst.com)

# Variation of Magnetic Susceptibility of Nanoparticle Sized Copper Cobalt Ferrites

**S. S. Karande[1], M. S. Kavale[1], B. R. Karche[2]**
[1]Department of Physics, Sangameshwar College, Solapur, Maharashtra, India
[2]Material Science and Thin Film Laboratory, Shankarrao Mohite Mahavidyalaya, Akluj, Dist. Solapur, Maharashtra, India

## ABSTRACT

The polycrystalline aluminium substituted nano-particle sized copper cobalt ferrite samples CuxCo1-xFe2-2yAl2yO4 (where x= 0.0, 0.2, 0.4, 0.6, 0.8, 1.0; y= 0.05, 0.15 and 0.25) have been prepared by standard ceramic technique. Phase formation is investigated using X-ray diffraction, Infrared absorption technique and Scanning electron microscope technique. The lattice constants of the all samples are evaluated from x-ray diffraction data. The Magnetic susceptibility decreases with aluminium and copper content.

**Keywords:** Polycrystalline, nanoparticle size, standard ceramic technique and Inverse cubic spinel, Magnetic susceptibility

## I. INTRODUCTION

In a way, every material utilized today is a composite. Composite materials are a physical mixture of two or more compatible micro or macro constituent particles which differ in form and chemical composition and are essentially insoluble in each other. Composite materials are best suited for scientific applications which could not be achieved by any one component acting on its own. Ferrite / ferroelectric composites are termed as magneto electric (ME) composites due to the coupling between the electric and magnetic fields in the materials. The conversion of magnetic to electric fields in such ME composite originates from the elastic interaction between ferrite and ferroelectric subsystems [1]. In the presence of the magnetic field, the magnetostriction in the ferrite phase gives rise to mechanical stresses that are transferred to the ferroelectric phase, resulting in electric polarization of the ferroelectric phase owing to its magneto electric effect. ME materials find applications as smart materials in actuators, sensors, magnetic probes, phase inverters, rectifiers, modulators, and transducers in solid state microelectronics and microwave devices [2,3].

Spinel ferrite nanoparticles are being intensively investigated in recent years because of their remarkable electrical and magnetic properties and wide practical applications in information storage system, ferro-fluid technology, magnetiocaloric refrigeration and medical diagnosis [4]. Among the spinels, mixed Zn ferrites and especially Ni–Zn ferrites are widely used in applications like transformer cores, chokes, coils, noise filters recording heads etc. [5]. While Ni–Zn ferrite posses higher resistivity and saturation magnetization, cobalt ferrite possess high cubic magneto crystalline anisotropy and hence high coercivity. The high coercivity is driven by large anisotropy of the cobalt ions due to its important spin orbit coupling. It is ferromagnetic with a Curie temperature ($T_c$) around 520°C, [6] and shows a relatively large magnetic hysteresis which distinguishes it from rest of the spinels. The synthesis of ultra fine magnetic particles has been extensively investigated in recent years because of their potential applications in high density magnetic recording and magnetic fluids [7]. Among the current methods for synthesis of mixed ferrite the combustion reaction method stands out as an alternative and highly promising method for the synthesis of these ferrites [8]. Magnetic properties measured at room temperature by vibrating sample magnetometer (VSM) reveal an increase in saturation magnetization with increase in cobalt concentration [9].

## II. EXPERIMENTAL

**Materials:**

High purity starting materials are used as Cobalt Oxide (CoO):- 74.9326 gm, Copper Oxide (CuO):- 74.5454 gm, Ferric oxide($Fe_2O_3$):- 159.6922 gm, Aluminum Oxide ($Al_2O_3$):- 101.9612 gm

**Preparation of ferrite**:

Nano crystalline powder samples of $Cu_xCo_{1-x}Fe_{2-2y}Al_{2y}O_4$ (where x= 0.0, 0.2, 0.4, 0.6, 0.8, 1.0; y = 0.05, 0.15 and 0.25) were prepared by the standard ceramic technique. Starting materials CuO, CoO, $Fe_2O_3$ and $Al_2O_3$ of AR grade obtained from Sigma – Aldrich, India were used. These samples were heated at ramping rate of 80 $^0$C hr $^{-1}$ at 1000$^0$C for 48 hours. XRD and IR analysis revealed the cubic spinel structure of the synthesized samples and functional groups in the samples respectively. The absence of any extra line confirms the formation of single phase ferrite. The average particle size 'D' was determined from line broadening (311) reflection using the Debye Scherer formula discussed elsewhere [10]. Calculations of lattice constant, physical density, X-ray density, porosity, site radii and ionic bond lengths on both sites were calculated by using formulae discussed elsewhere [11] and graphically shown in fig.4. Infrared absorption spectra of powdered samples were recorded in the range 350-800 cm$^{-1}$ using Perkin-Elmer FTIR spectrum and spectrometer by KBr pellet technique and presented in (fig.2). The scanning electron microscopes are shown in fig.3

## III. RESULTS AND DISCUSSION

The X-ray diffraction patterns of the samples are presented in (fig.1). Powder X-ray diffractometer of the ferrite samples reveals the single phase spinel structure, as well defined reflection is observed without any ambiguity. The diffraction peaks are corresponding to (200), (311), (400), (422), (333/511), (440) and (533) planes. The lattice constants ‘a’ and ‘c’ for all prepared samples are calculated by using prominent (311) XRD peak. The calculated and observed values of inter planer distance (d) are found in good agreement with each other for all reflections. The physical density (dB), x-ray density (dx), and porosity (p), are calculated from the formulae given by Gadkari et.al [12].

From the calculations of lattice constants ‘a’ and ‘c’ for all the prepared ferrites it is observed that c >a and tetragonality ratio (c/a) is found in the range of 1.03 to 1.07. This result is in good agreement with previous report [13-14].In this present report tetragonality ratio for copper ferrite is 1.06. It means 70% copper resides on B site and it exhibits prorate type distortions in the crystal lattice. The previous report [15] well supports the present results reported this communication. Both $Fe^{3+}$ and $Cu^{2+}$ are John-Teller ion which produces prolate type distortions on (B) site and hence c >a and (c/a) = 1.06. Therefore copper ferrite exhibits tetragonal spinel structure in host crystal lattice of cobalt ferrite. In addition of copper content in tetragonality ratio is found increasing but due to addition of aluminium tetragonality ratio deceases. It means that $Al^{3+}$ and copper suppress the tetragonal prolate type.

The crystallite sizes (t) of all the prepared samples were computed by Scherer rule utilizing the peak width at one-half intensity of the maximum intensity peak (311).

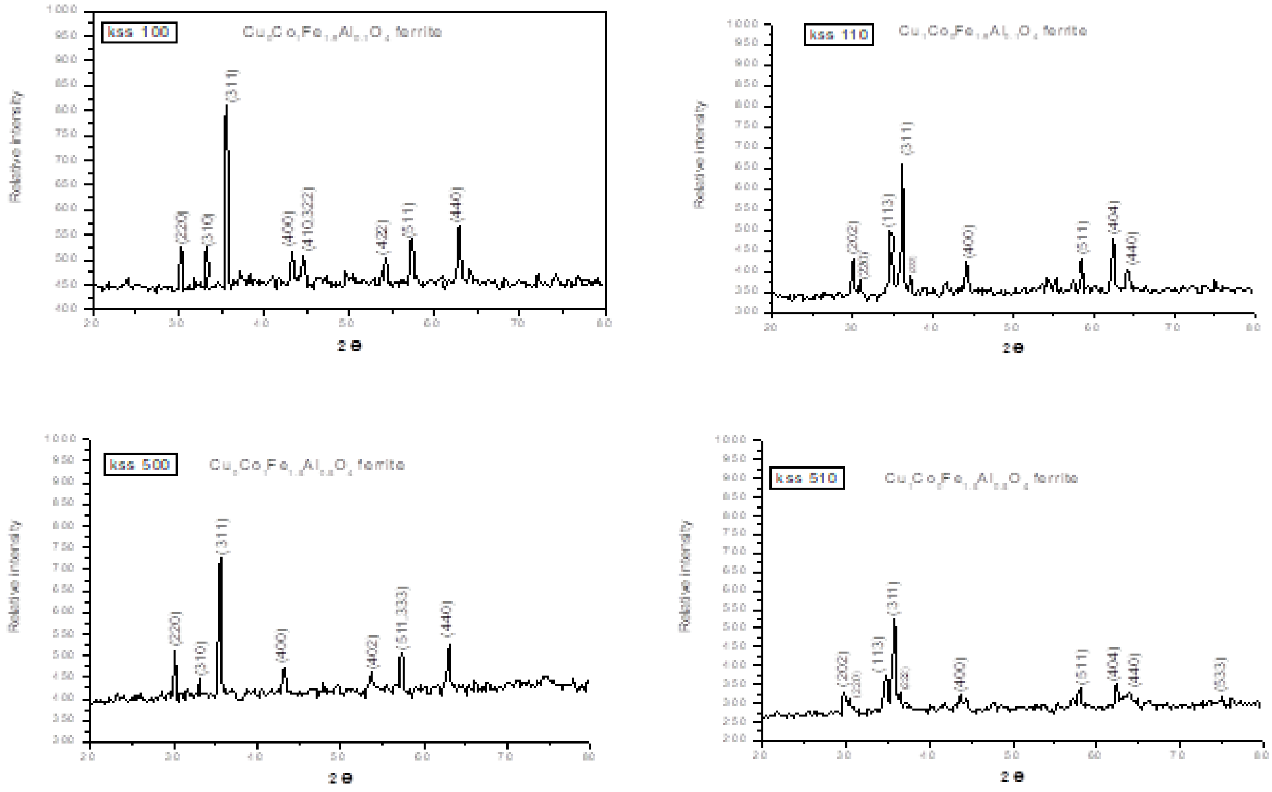

**Fig: 1 XRD patterns of system $Cu_xCo_{1-x}Fe_{2-2y}Al_{2y}O_4$**

The Al (y = 0.05-0.25) doped copper cobalt ferrite samples show a higher grain growth and the crystallite size (t) lies in the extent of 52.53-94.4 nm. The mean particle size calculated from diffractograms is in the range of 50 to 100 nm. That suggest the particles in the ferrites samples are fine and there is continuous grain growth in all compositions. It gives the confirmation of suitable microstructure formation in all compositions.

The width of the reflection peak (311) for all the compositions is approximately the same due to the nearly equal particle size.

The infrared absorption spectra are showing two distinct absorption bands $\nu_1$ due to tetrahedral (A) site interstitial voids near 600 $cm^{-1}$ and other $\nu_2$ due to octahedral (B) site interstitials voids near 400 $cm^{-1}$. Our results in this present communication are well supported by previous reports [16, 17].

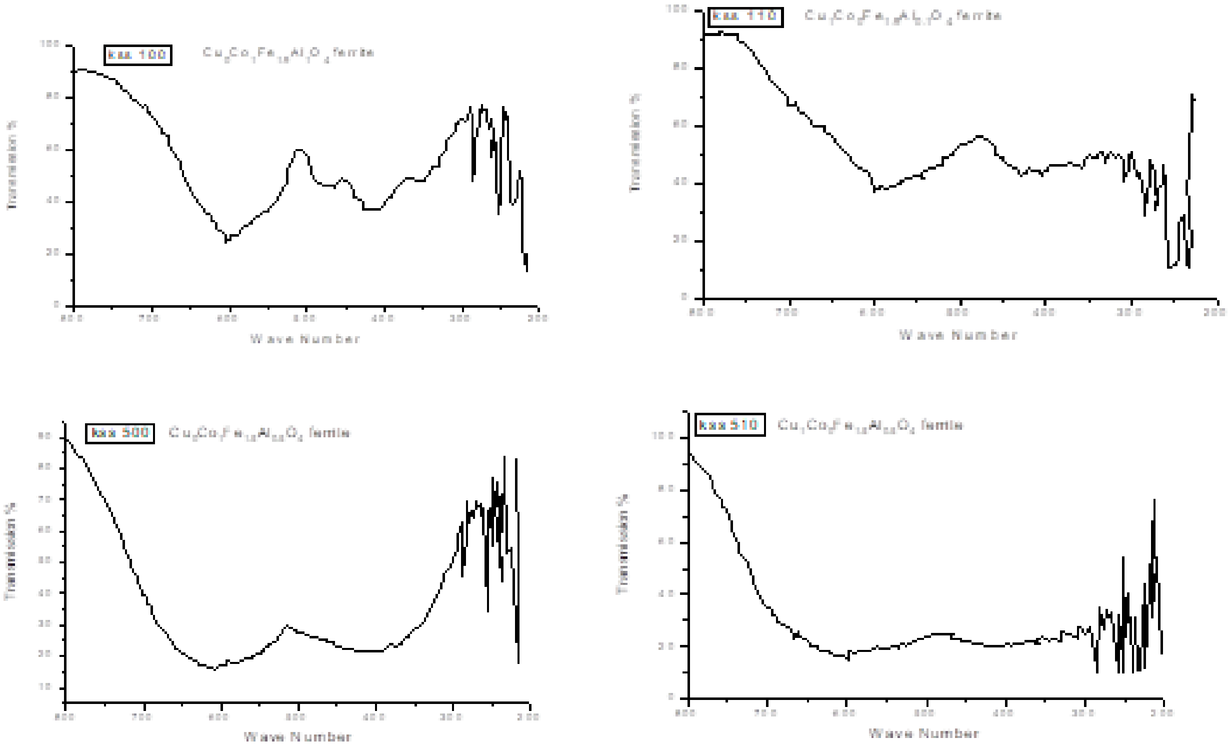

**Figure 2: Absorption spectra for system $Cu_xCo_{1-x}Fe_{2-2y}Al_{2y}O_4$**

The close inspection of all micrographs revealed that there is continuous grain growth with well – defined grain boundaries formed. The present system shows multi domain behavior. No exaggerated grain growth is observed in any composition. The average grain size is found to decrease with increase in Al content in copper cobalt ferrite. However in the present system the grain growth shows generally a decreasing trend with aluminum content, which is rather expected because of multi-domain behavior of these compositions in copper cobalt ferrite. Grain growth is almost accompanied with grain size, which is increasing with copper and aluminum content. So it appears that copper and aluminum content favors the grain growth. The scanning electron micrographs shown below

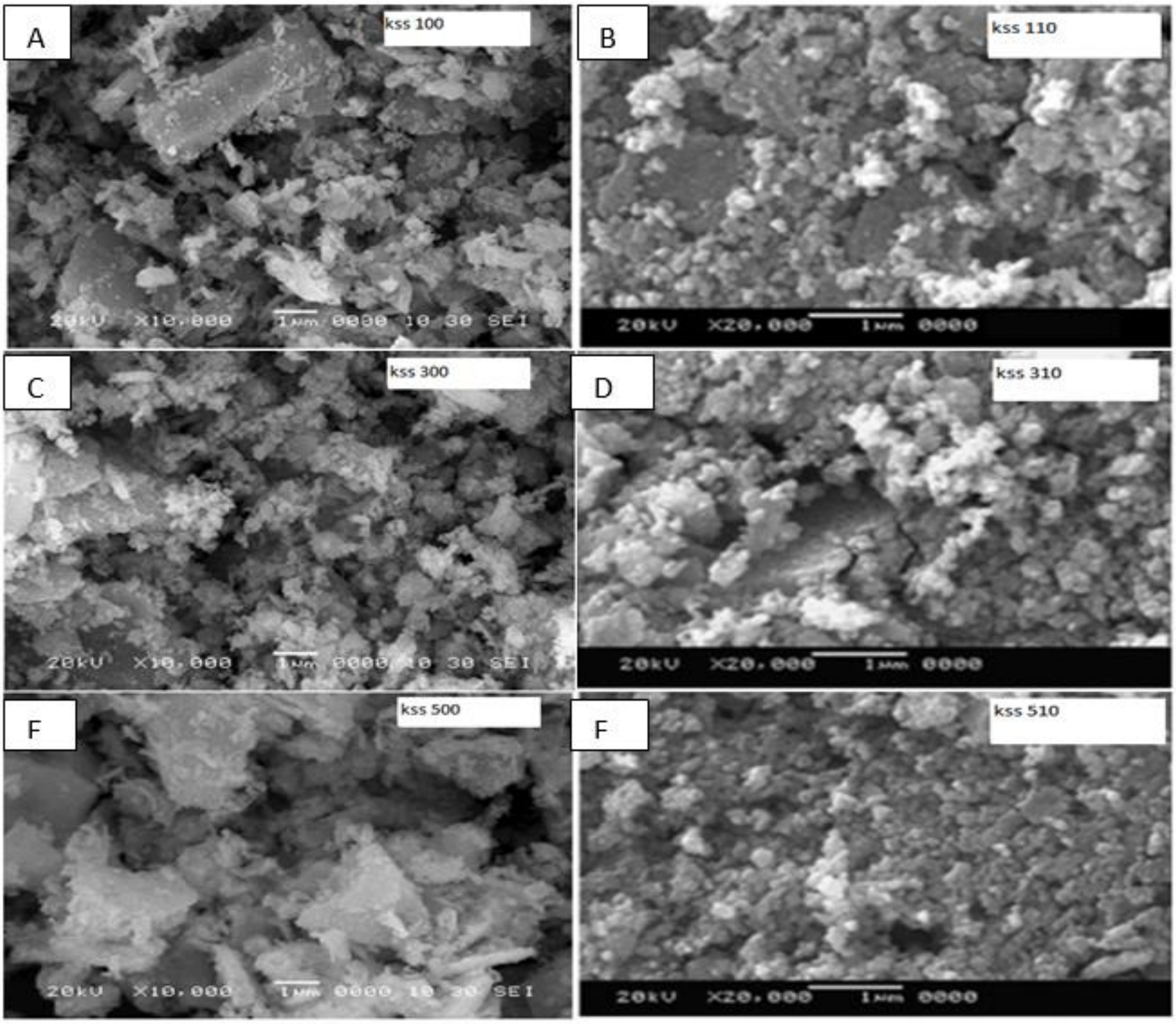

**Fig: 3 (A) to (F) scanning electron microscopes of $Cu_xCo_{1-x}Fe_{2-2y}Al_{2y}O_4$ :**

**(A) KSS 100-$Cu_0Co_1Fe_{1.9}Al_{0.1}O_4$, (B) KSS 110- $Cu_1Co_0Fe_{1.9}Al_{0.1}O_4$,**

**(C) KSS 300- $Cu_0Co_1Fe_{1.7}Al_{0.3}O_4$, (D) KSS 310- $Cu_1Co_0Fe_{1.7}Al_{0.3}O_4$,**

**(E) KSS 500- $Cu_0Co_1Fe_{1.5}Al_{0.5}O_4$ & (F) KSS 510- $Cu_1Co_0Fe_{1.5}Al_{0.5}O_4$**

The susceptibility is measured at room temperature [Fig. 2(a)] then susceptibility is found increasing up to 20 % of copper content and thereafter decreases. The susceptibility is measured at various temperatures [Fig. 2(b)], the compositions shows gradual decrease in normalized susceptibility with temperature which suggest that they exhibit super paramagnetic (SP) structure having fine particles. The susceptibility is decreases and curie temperature also shifts towards minimum value as copper as well as aluminum content increases.

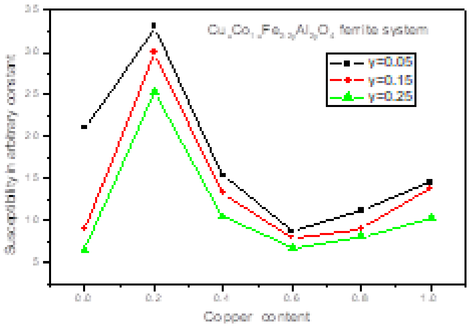

Fig. 4(a)

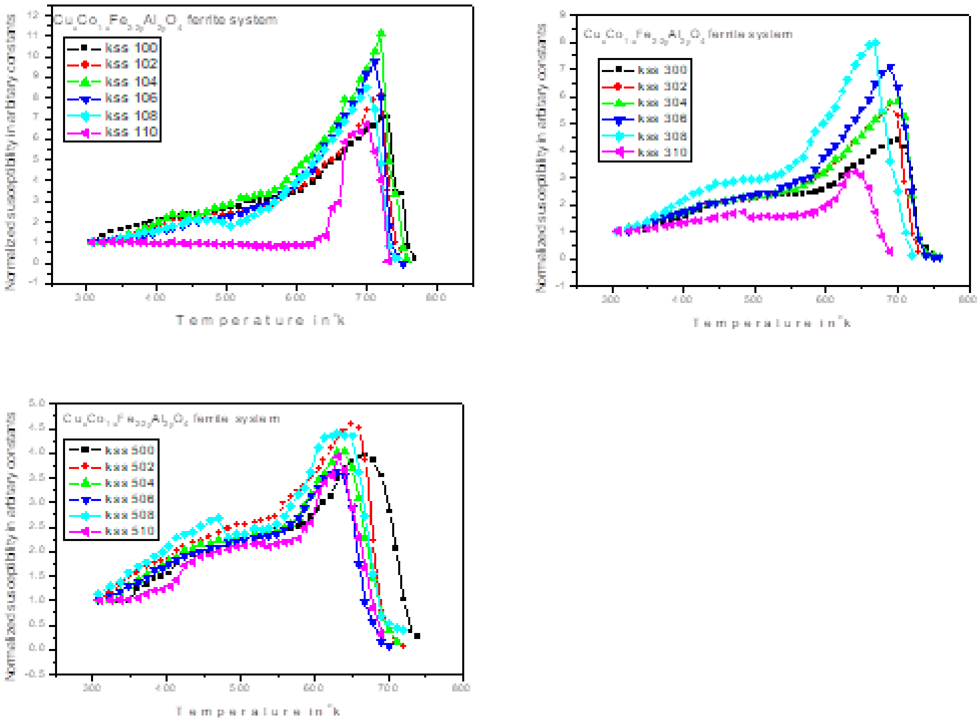

Fig. 4(b)

**Fig 4: Variation of A. C. susceptibility with copper and aluminum content at room temperature and various temperature for $Cu_xCo_{1-x}Fe_{2-2y}Al_{2y}O_4$ ferrite system**

## IV. CONCLUSIONS

Copper cobalt ferrite is partially inverse spinel ferrite. Addition of $Al^{3+}$ ions replaces $Fe^{3+}$ on (B) site resulting in increase of lattice constant a, decrease in ionic radii($R_A$) and bond length(O-A). The lattice constant obtained from XRD data shows increases. The A. C. susceptibility goes on decreasing with copper and aluminum content.

## V. REFERENCES

[1]. R. S. Devan, S. A. Lokare, S. S. Chougule, D. R. Patil, Y. D. Kolekar, andB. K. Chougule, J. Phys. Chem. Solids 67, 1524 (2006).

[2]. K. Zhao, K. Chen, Y. R. Dai, J. G. Wan, and J. S. Zhu, Appl. Phys. Lett. 87, 162901 (2005).

[3]. S. R. Kulkarni, C. M. Kanamadi, and B. K. Chougule, Mater. Res. Bull. 40, 2064 (2005).

[4]. Zhao L, Yang H, Yu L, Cui Y, Zhao X, Zou B, Feng SJ. MagnMagn Mater2006;301:445–51.

[5]. Rath C, Sahu KK, Anand S, Date SK, Mishra NC, Das RP. J MagnMagn Mater 1999;202:77–84.

[6]. Rajendran M, Pullar RC, Bhattacharya AK, Das D, Chintalapudi SN, Majumdar CK. J MagnMagn Mater 2001;232:71–83.

[7]. Ozaki M. Mater Res Bull 1989;12:35–43.

[8]. Costa ACM, Tortella E, Morelli MR, Kaufman M, Kiminami RHGA. J Mater Sci2002;37:3569–72.

[9]. M.M. Mallapur, B.K. Chougule; Materials Letters; Vol. 64 (2010); P. 231–234.

[10].H. P. Klug, L. E. Alexander, X-ray diffraction procedure for polycrystalline and amorphous materials, Willey N.Y, 1997, 637.

[11].A. B. Gadkari, T. J. Shinde, P. N. Vasambekar, J. Mater Sci: Mater Electron 21 2010, 96 , 103.

[12].Prince E., Treuting R.G; Acta Crystallographica, 1956, 9, 1025.

[13].Sagal K., Tabellen F. Rontegenstrukturanalyse, Springer, Berlin, 1958.

[14].Borisenko A., Toropov N. A; Z. Prikl Chem, 1950, 23, 1165.

[15].Goodenough J.B and Loeb A. L ,Phys. Rev., 1955, 98, 391.

[16].Waldron R.D, Phy. Rev, 1955, 99(6), 1727.

[17].K. V. S. Badarinath, Phys. Stat. Solidi (a) 1985, 91, 19-23.

International e-Conference on Recent Trends in Nano-Materials and Its Applications
In Association with International Journal of Scientific Research in Science and Technology
Volume 9 | Issue 11 | Print ISSN: 2395-6011 | Online ISSN: 2395-602X (www.ijsrst.com)

# DC Resistivity of La3+ Substituted Mg-Zn Ferrite Nanoparticles by Co-Precipitation Method

**R.A. Bugad[1]*, B.G. Pawar[1], B.B. Navale[2], P.G. Pawar[3]**
[1]Department of Science, Sangola Mahavidyalaya, Sangola, Dist. Solapur 413307, Maharashtra, India
[2]Department of Science, Vidnyan Mahavidyalaya, Sangola, Dist. Solapur 413307, Maharashtra, India
[3]Department of Science, Shivaji Polytechnic College, Sangola, Dist. Solapur 413307, Maharashtra, India

## ABSTRACT

Lanthanum (La) substituted magnesium zinc ferrite nanoparticles with general formula Mg0.6Zn0.4La2yFe2-2yO4 (where y = 0.00, 0.05, 0.10, 0.15, 0.20 and 0.25) have been synthesized by co-precipitation method. The XRD analysis was carried out to confirm the single –phase cubic structure of La3+ substituted Mg-Zn ferrite. The nature of DC resistivity of ferrite was studied with substitution of La3+ content. The effects of La3+ substitution in Mg-Zn ferrite on structural and electric properties were studied.

**Keywords:** Lanthanum, Mg-Zn ferrites, Co-precipitation, DC Resistivity,

## I. INTRODUCTION

Ferrites are usually non-conductive ferrimagnetic ceramic material. Most of the ferrites have a spinel structure [1]. The general formula of a spinel can be written as $AB_2O_4$. Nano-particles of mixed spinel ferrites have been the subject of current interest because of their interesting electric, optical and magnetic properties, which are considerably different from that of their bulk ferrites [2]. The ferrites are also widely used in high frequency cores, antennas, high frequency transformers, deflecting coil, motor generator and microwave devices such as modulators, phase shifter and circulators etc.[3]. The coercive force is related with saturation magnetization, anisotropy, internal stresses and porosity. The ferrites having low coercive force (HC) is known as Soft ferrites [4]. Generally, soft ferrite shows high electrical resistivity, superior magnetic and structural properties and hence they have low eddy current losses at high frequency [5]. Demand for electronic and computer components with high density and light weight performance is greatly increasing, which step up the demand for soft ferrites with high performance and thus contributes to the development of soft magnetic ferrites on the direction of higher frequency and lower power consumption [6].

## II. EXPERIMENTAL

### 2.1. Synthesis of $La^{3+}$ substituted Mg-Zn ferrite

The $Mg_{0.6}Zn_{0.4}La_{2y}Fe_{2-2y}O_4$ (where y= 0.00, 0.05, 0.10, 0.15, 0.20 & 0.25) have been prepared by the oxalate co-precipitation method as per reported in earlier literature [7]. The high purity AR grade starting materials $MgSO_4.7H_2O$, $ZnSO_4.7H_2O$, $LaSO_4.7H_2O$ and $Fe_2SO_4.7H_2O$ were used for preparation of samples. These chemicals were weighted in desired stoichiometric proportion and dissolved in distilled water. The pH of the solution was maintained at 4.8 by drop wise addition of concentrated $H_2SO_4$. The resulting solution was heated at 80 $^0$C for 1 h in order to complete the ionization of metal sulfates. The precipitating regent was prepared in distilled water by adding required proportion of AR grade ammonium oxalate. Ammonium oxalate was taken in burette and was added drop by drop until the precipitation was formed. The co-precipitate product was dried and calcined at 450 $^0$C for 5h in air. The calcined powders were milled in an agate mortar with AR grade acetone as a base. The powders were pre-sintered at 700 $^0$C for 5h.The pre-sintered powders were pressed under hydraulic pressure of 5 tones /$cm^3$ to form pellet using polyvinyl alcohol as binder. Then pellets were finally sintered at 900 $^0$C for 12h.

### 2.2. Characterization Techniques

XRD patterns of lanthanum substituted magnesium zinc ferrites sintered at 900$^0$C for 12h were recorded by Philips X-Ray Diffractometer model PW 1710 using Cu Ka radiation ( $\lambda$ = 1.5405 A$^0$ ). Two probe method was used for measurement of the dc electrical resistivity of ferrite in the temperature range 25$^0$C to 575$^0$C. The resistivity was obtained by using formula $\rho = \frac{\pi r^2}{t} \times \frac{V}{I} = \frac{\pi r^2\ R}{t}$ , Where, t is thickness and r is radius of the pellet in cm.

## III. RESULTS AND DISCUSSIONS

### 3.1. XRD studies

The XRD patterns of $Mg_{0.6}Zn_{0.4}La_{2y}Fe_{2-2y}O_4$ (where y = 0.00, 0.05, 0.10, 0.15, 0.20, 0.25) ferrite system sintered at temperature 900$^0$C for 12h are shown in Fig. 1. The XRD patterns reveals the well resolved, sharp and intense peaks corresponding to planes (220), (311), (222), (400), (422), (511), (440), (620) and (533). The peaks obtained in the diffractogram closely match the data in the JCPDS file card number (04-002-5442). The XRD peak pattern corresponds to all allowed planes, which hint outs single phase cubic structure with the traces of secondary phase. Moreover, the peak at $2\theta$= 32.10$^\circ$ corresponds to plane (121) which is attributed to secondary phase for $LaFeO_3$ indexed as per ICDD file No. 01-74-9045. With increase in La content, intensity of characteristics peak (311) for $Fe_2O_4$ gradually decreases, while intensity of peak (121) of $LaFeO_3$ increases. It implies that the substituted $La^{3+}$ ion has a solubility limit in the spinel lattice.

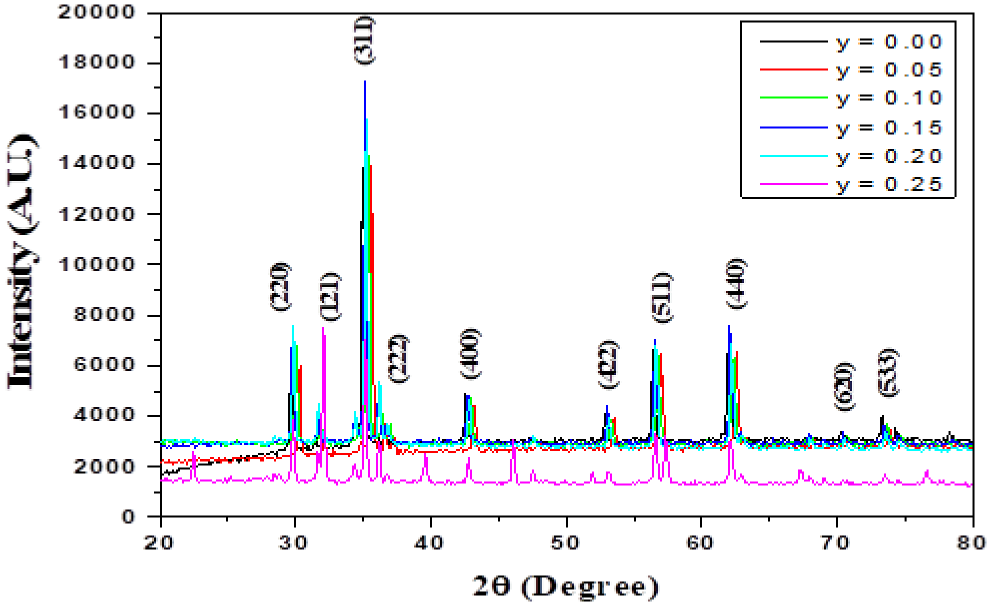

**Fig.1** : XRD patterns of $Mg_{0.6}Zn_{0.4}La_{2y}Fe_{2-2y}O_4$ ferrite system

The degree of substitution of $Fe^{3+}$by $La^{3+}$ ion is limited in the spinel lattice due to larger ionic radii of $La^{3+}$ ions compared to $Fe^{3+}$ions. There is always some $La^{3+}$ ions do not enter into spinel lattice. These $La^{3+}$ ions react with $Fe^{3+}$ ions and form second phase $LaFeO_3$ usually locating at the grain boundaries. Similar observation have been reported in lanthanum substituted nickel [8], Cadmium [9] and Ni-Zi ferrites [10, 11].

## 3.2. DC Resistivity study

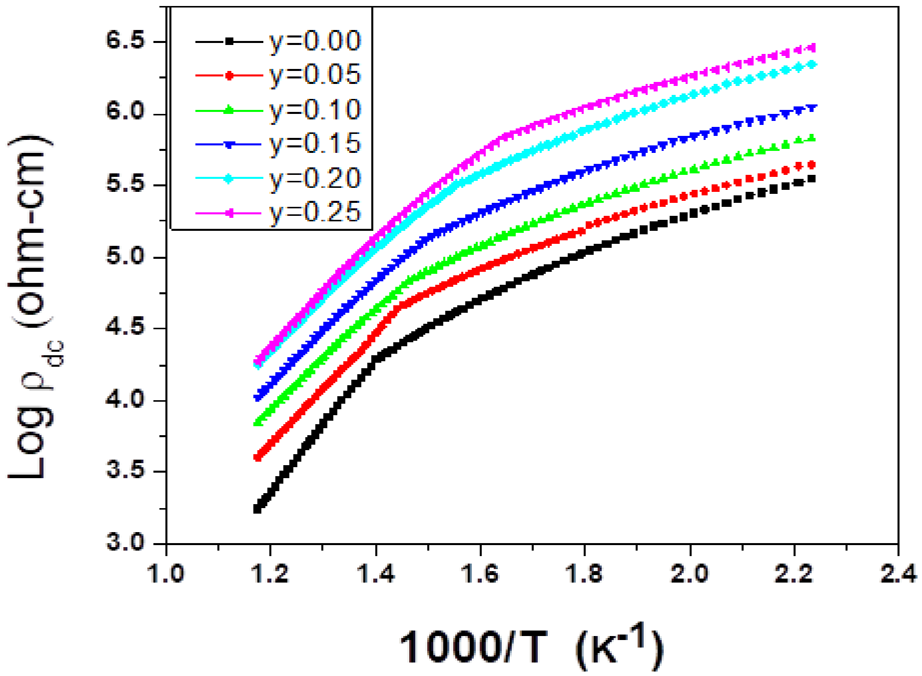

**Fig.2:** Variation of dc resistivity with inverse temperature for $Mg_{0.6}Zn_{0.4}La_{2y}Fe_{2-2y}O_4$ ferrite system

The variation of log of dc electrical resistivity (log$\rho_{dc}$) as a function of inverse of temperature (1000/T) for various composition of $Mg_{0.6}Zn_{0.4}La_{2y}Fe_{2-2y}O_4$ ferrite is shown in Fig.2, The dc resistivity of the ferrites gets decreased with an increase in temperature indicates semiconducting behavior of the ferrites. All the samples show the break at Curie temperatures due to the change in conduction mechanism [12]. The slope change at Curie temperature corresponds to the samples transform from an ordered ferrimagnetic state to disordered paramagnetic state [13]. The value of Curie temperature obtained from the graph of log$\rho_{dc}$ verses 1/T is calculated. The Curie temperature decreases with increase of $La^{3+}$ content. It is due to the nonmagnetic nature of $La^{3+}$ ions, which may break linkage between magnetic cations [14]. Rare earth $La^{3+}$ ions have a strong preference to occupy on octahedral site and therefore replace $Fe^{3+}$ ions at octahedral site (B) in spinel lattice by $La^{3+}$. Upon increase in the $La^{3+}$ ions in B-site, A-B interaction weakens. Thus the decrease in Curie temperature is probably due to weakening of the A-B interaction. Similar observations have also been reported by Patil et al. [15]. The conduction phenomenon in polycrystalline ferrites was explained on the basis of Verwey and de Boer mechanism [16]. The conduction in ferrites is due to hopping of electrons between $Fe^{2+}$ and $Fe^{3+}$ ions on the octahedral (B) sites. In addition of lanthanum in Mg-Zn ferrite, it found that, $Zn^{2+}$ ion have strong tendancy to occupy A-site and $Mg^{2+}$ ion have strong preference to occupy B-site, While $La^{3+}$ preferencelly occupy to octahedral B site, where it replaced $Fe^{3+}$ ions in the B-site as per the modified cation distribution in magnetic study. The resistivity of the ferrite is controlled by $Fe^{3+}$ concentration on B-site. The increase in resistivity with $La^{3+}$ content is due to overall decrease in $Fe^{3+}$ ions concentration on B-site. It causes decrease in hopping of electrons between $Fe^{2+}$ and $Fe^{3+}$ ions, results in decrease in conduction in ferrite with increase of resistivity [17]. Several researchers have been reported that resistivity of ferrites increases with the substitution of rare earth [18]. Gul and Ahmed also reported the effect of grain size, porosity and grain boundary area on resistivity of ferrite [19]. It is found that one of the factors for higher resistivity in ferrite is the decrease in grain size upon the addition of lanthanum. Smaller grain size produces larger number of insulating grain boundaries which produces inhomogeneous structure and greater energy is required for electron conduction which affects on AC and DC resistivity of ferrites [20].

## IV. CONCLUSIONS

In conclusion, we report the preparation of lanthanum substituted magnesium zinc ferrites by co-precipitation method. A study on DC resistivity shows all sample have semiconducting behavior and break at Curie temperature. The conduction phenomenon in polycrystalline ferrites was explained on the basis of Verwey and de Boer mechanism. The increase in DC resistivity is due to low concentration of $Fe^{2+}$ ions, which is responsible for decrease in electronic polarization. The increase of dc resistivity with La content was mainly attributed to decreases in drift mobility with lanthanum content. This study reveals that Lathanum substitution alters the structural and electric properties of Mg-Zn ferrites.

## V. REFERENCES

[1]. M. Kaur, B.S. Randhawa, J. Singh, D. Utreja , Thermolysis studies on magnesium zinc bis(citrato)ferrate pentahydrate precursor for synthesis of ferrite nanoparticles, J. Ceramics Int., 39 (2013) 325-328.

[2]. V. Provenzano, & R. L. Holtz, Nanocomposites for high temperature applications. Mat.Sci. and Eng. A, 204(1-2) (1995)125-134.

[3]. S. R. Hoh, “Evaluation of High Performance Core Materials”, Tele. Tech. 2 (1953) 86.

[4]. E.W. Lee, Soft magnetic material, Advances in Physics, 8 (1959) 292.

[5]. E.E. Richards and A.C. Lynch, “Soft Magnetic Materials for Telecommunications”, Pergamon Press Ltd. (1953).

[6]. A. Sharma, K.S. Pallavi, R. Sharma, “Optical Properties of Tin Oxide Nanoparticles”, ISST Journal of Applied Physics, 2(2)(2011) 13-14.

[7]. R. A. Bugad, T. R. Mane, B. B. Navale, J. V. Thombare, A. R. Babar, B. R. Karche, Structural, morphological and compositional properties of La3+ substituted Mg-Zn ferrite interlocked nanoparticles by co-precipitation method, J. Mater. Sci.: Mater. Electron. 28 (2017) 1590-1596.

[8]. S. E. Shirsath, B. G. Toksha, K. M. Jadhav, Structural and Magnetic properties of La^(3+) substituted NiFe2O4, Mater. Chem. Phys. 117(2009)163-168.

[9]. A. Gadkari, T. Shinde, P. Vasambekar, Influence of rare-earth ions on structural and Magnetic properties of CdFe2O4, Rare Metal, 29(2) (2010)148.

[10].Y. K. Dasan, B. H. Guan, M. H. Zahari, L. K. Chuan, Influence of La^(3+) substitution on structure, Morphology and Magnetic properties of Nanocrystalline Ni-Zn ferrite, PLoS ONE 12(1) (2017)75.

[11].M. Soka, M. Usakova, R. Dosoudil, E. Usak, J. Lokaj, Effect of lanthanum substitution on structural and magnetic properties of nickel zinc ferrites, AIP Advances 8 (2018) 047802.

[12].D. Ravinder, B. Ravikumar, A study on elastic behaviour of rare earth substituted Mn–Zn ferrites, Mater. Lett. 57 (2003) 4471-4473.

[13].A.A. Sattar, Egypt., Temperature Dependence of the Electrical Resistivity and Thermoelectric Power of Rare Earth Substituted Cu-Cd ferrite J. Sol., 26(2003)113.

[14].A. I. Ali, M. A. Ahmed, N. Okashad, M. Hammam, J. Y. Son, Effect of the La3+ ions substitution on the magnetic properties of spinal Li-Zn-ferrites at low temperature, J. Mater. Res. Technol. 2 (2013) 356–361.

[15].S. B. Patil, R. P. Patil, J. S. Ghodake, B. K. Chougule, Temperature and frequency dependent dielectric properties of Ni–Mg–Zn–Co ferrites, J. Magn. Magn. Mater. 350 (2014) 179-182.

[16].E. J. W. Verwey, F. de Boer and J.H. Van Santen, Cation Arrangement in Spinels, J. Chem. Phys. 16 (1948) 1091.

[17].K. Torkar & O. Fredriksen, The effect of grain size on saturation magnetization of barium ferrite powders, J. Powder Metallurgy, (2014) 105-107.

[18].G. L. Sun, J. B. Li, J. J. Sun, X-Z Yang, The influences of Zn2+ and some rare-earth ions on the magnetic properties of nickel–zinc ferrites, J. Magn. Magn. Mater. 281 (2004)173.

[19].I. H. Gul, W. Ahmed and A. Maqsood, Electrical and magnetic characterization of nanocrystalline Ni–Zn ferrite synthesis by co-precipitation route, J. Magn. Magn. Mater. 320 (2008) 270-275.

[20].T. J. Shinde, A. B. Gadkari, P. N. Vasembekar, Effect of Nd3+ substitution on structural electrical properties of nanocrystalline zinc ferrite, J. Magn. Magn. Mater. 322(2010) 2777–2781.

International e-Conference on Recent Trends in Nano-Materials and Its Applications
In Association with International Journal of Scientific Research in Science and Technology
Volume 9 | Issue 11 | Print ISSN: 2395-6011 | Online ISSN: 2395-602X (www.ijsrst.com)

# Self-Focusing of Gaussian Laser Beam in Collision less Plasma with Linear Absorption

**K.Y. Khandale[1], P.T. Takale[1], T.U. Urunkar[1], S.S. Patil[2], P.P. Nikam[2], M.B. Mane[2], V.S. Pawar[2], S.D. Patil[2], M.V. Takale[1]**

[1]Department of Physics, Shivaji University, Kolhapur 416 004, Maharashtra, India

[2]Department of Physics, Devchand College, Arjunnagar, Kolhapur 591 237, Maharashtra, India

## ABSTRACT

In the present work, authors have studied the effect of linear absorption on the self-focusing of Gaussian laser beam propagating in the collisionless plasma. The non-linear dependence of the dielectric constant inside collisionless plasma is mainly due to the ponderomotive force. The field distribution in the medium is expressed in terms of linear absorption coefficient as well as beam-width parameter. By following Akhmanov's parabolic equation approach under Wentzel-Kramers-Brillouin (WKB) approximation and Paraxial approximations, the differential equation is set up for the beam width parameter f which is solved numerically. It is noticed that the absorption coefficient plays an important role in propagation of Gaussian laser beam in collisionless plasma. The graphical results are presented and are discussed at the end.

**Keywords:** Gaussian laser beam, Collisionless Plasma, Linear absorption, Self-focusing.

## I. INTRODUCTION

With the invention of laser nearly six decades (1960-2020) ago, a fascinating new field of research known by the name "Nonlinear Optics" is introduced to the scientific community. Nonlinear optics has its origin when researchers P.A. Fraken and his co-workers in 1961 noticed that a weak optical signal at 3472 Å could be generated in quartz crystal when the material is illuminated with a high power Ruby laser at 6943 Å on optical second-harmonic generation in 1961 the theoretical work of J.A. Armstrong and his co-workers on optical wave mixing in 19621–3. Self-focusing is one of the phenomena in which the intense beam of laser light incident on material medium changes the optical properties in such a way that beam comes to focus within the medium. There are three major mechanisms that lead to a change in the dielectric constant of plasma in laser-plasma interaction, as follows: (i) the relativistic effect (ii) the collisional and (iii) the ponderomotive force4–6.

With the availability of high power laser beams, a large number of interesting nonlinear phenomena have been studied, both theoretically and experimentally. The redistribution of carriers is caused by the pondermotive force and is mainly important in collisionless plasmas. When an intense laser beam propagates through collisionless plasma, the drift velocity of electrons is relativistic so that their mass is intensity dependant but for long pulse experiments, the relativistic effects can be ignored and ponderomotive force of the beam nonlinearity perturbs electron density resulting in the excitation of electron plasma wave7,8. Light absorption has played an important role in studies on the self-focusing of laser beams in different situations. The contribution of light absorption has been ignored in the most of investigations on self-focusing of laser beams in plasmas9–14. Furthermore, Navare et al.15, M. A. Wani et al.16, L. Ouahid et al.17, R. Kashyap et al.18, T. U. Urunkar et al.19, K. M. Gavade et al.20, B. D. Vhanmore et al.21 and S. D. Patil et al.22–25 have investigated the effect of linear absorption on the self-focusing of a Gaussian, Chirped Gaussian, Airy–Gaussian, q-Gaussian, Gaussian, Cosh-Gaussian, elegant Hermite-cosh-Gaussian, Cosh-Gaussian, Gaussian laser beam respectively by considering the different nonlinearities in different situations. The aim of the present investigation is to study the effect of linear absorption on the self-focusing of Gaussian laser beam propagating in the collisionless plasma. The present analysis is carried through parabolic equation approach under WKB and paraxial approximations.

## II. THEORETICAL FRAMEWORK

Consider the propagation of Gaussian laser beam in homogeneous collisionless plasma along the z-direction, initial intensity distribution of Gaussian laser beam at z = 0 can be expressed as

$$\bar{E}\bar{E}^* = E_0^2 \exp\left(-\frac{r^2}{{r_0}^2}\right), \qquad (1)$$

where E_0 is the amplitude of Gaussian intensity distribution, r is the radial coordinate of cylindrical coordinate system, r_0 is the initial beam width of the laser beam. The wave equation governing the electric field Ē of the laser beam in homogeneous plasma along with the effective dielectric constant ε, in the cylindrical co-ordinate system is given by,

$$\frac{\partial^2 \bar{E}}{\partial z^2} + \frac{\partial^2 \bar{E}}{\partial r^2} + \frac{1}{r}\frac{\partial \bar{E}}{\partial r} + \frac{\omega^2}{c^2}\varepsilon\, \bar{E} = 0 \qquad (2)$$

When a laser beam propagates through homogeneous gaseous plasma, the effective dielectric constant changes significantly and can be, in general represented as5

$$\varepsilon = \varepsilon_0 + \phi\,(EE^*) - i\varepsilon_i\,, \qquad (3)$$

where ε_0= 1-( 〖ω_p〗 ^2/ ω^2 ) is linear part and ϕ is nonlinear part of the dielectric constant, ω_p is the plasma frequency 〖ω_p〗 ^2=(4π n_e e^2/ m_0) , here e, m_0 and n_e are the charge of electron, rest mass of electron and density of plasma electrons in the absence of laser beam respectively and ε_i takes care of absorption. The second term in the equation (3) is the nonlinear dielectric constant for collisionless plasma can be represented as5

$$\phi\,(EE^*) = \frac{{\omega_p}^2}{\omega^2}\left[1 - \exp\left(-\frac{3m\,\alpha EE^*}{4M}\right)\right], \qquad (4)$$

with $\alpha = \left(\frac{e^2 M}{6\,k_B T_0 \omega^2 m^2}\right),$

where M, m, k_B and T_0 are mass of ion, mass of electron, Boltzmann constant and equilibrium plasma temperature respectively. By using WKB and paraxial approximations the coupled equations in terms of eikonal S and intensity of laser beam A_0^2 can be expressed as

$$2\,\frac{\partial S}{\partial z}+\left(\frac{\partial S}{\partial r}\right)^2=\frac{\omega_p{}^2}{\varepsilon_0\,\omega^2}\left[1-\exp\left(-\frac{3m\,\alpha EE^*}{4M}\right)\right]+\frac{1}{k^2A_0}\,\nabla_\perp{}^2A_0 \tag{5}$$

And

$$\frac{\partial A_0^2}{\partial z}+\frac{\partial S}{\partial r}\,\frac{\partial A_0^2}{\partial r}+\left(\frac{\partial^2 S}{\partial r^2}+\frac{1}{r}\frac{\partial S}{\partial r}-\,k\,\frac{\varepsilon_i}{\varepsilon_0}\right)A_0^2=0. \tag{6}$$

The solution for equations (5) and (6) which satisfies the initial conditions for a Gaussian beam's intensity distribution is as follows:

$$S=\frac{r^2}{2\,f}\,\frac{\partial f}{\partial z}+\,\phi(z), \tag{7}$$

And

$$A_0^2=\frac{E_0^2}{f^2}\,\exp\left(-\frac{r^2}{r_0{}^2\,f^2}-\,2k_iz\right), \tag{8}$$

where ϕ is the axial phase and k_i is the absorption coefficient. By following the approach given by Akhmanov et al.4 and its simple extension by Sodha et al.5 the dimensionless beamwidth parameter f is obtained as,

$$\frac{d^2f}{d\xi^2}=\frac{1}{f^3}-\frac{3m\,p\,\rho_0\,e^{-\frac{3m\,p\,e^{-2k_i'\xi}}{4Mf}-\,4k_i'\,\xi}}{4\,M\,f^3} \tag{9}$$

where ξ= z/ R_d known as dimensionless distance of propagation, p = αE02 is the initial intensity parameter, R_d=k r_0^2 is known as Rayleigh diffraction length, ρ_0= (ω_p r_0)/c is the normalized equilibrium beam radius and k_i^'=k_i R_d is the normalized absorption coefficient. The equation (9) can be solved numerically with appropriate boundary conditions such as f = 1, ξ=0 and ∂f/∂z=0. By using critical condition in equation (9) one may obtain equilibrium beam radius as follows. Here p is known as critical beam power.

$$\rho_0=\sqrt{\frac{4M}{3m\,p\,e^{-\frac{3m\,p\,e^{-2k_i{}'\xi}}{4M}-\,4\,k_i{}'\xi}}} \tag{10}$$

## III. RESULT AND DISCUSSION

Equation (9) is a nonlinear, ordinary second order differential equation which shows the variation of dimensionless beam-width parameter f with respect to normalized propagation distance ξ into the collisionless plasma. First term on the right hand side of the equation (9) is the diffraction divergence which is responsible for defocusing and second term is the convergence arising from the collisionless nonlinearity and also depends on normalized absorption coefficient k_i^' which is responsible for self-focusing of the beam. The equation (9) is a second order nonlinear ordinary differential equation and is solved numerically by choosing following laser-plasma parameters: ω_p= 1.7760 × 1015 rad/s, r_0 = 20 × 10-4 cm, c = 3 × 1010 cm/s, n0 = 1018 cm–3, ρ_0=65, p = αE0 2 = 10, to study the effect of linear absorption on the self-focusing of the beam in collisionless plasma.

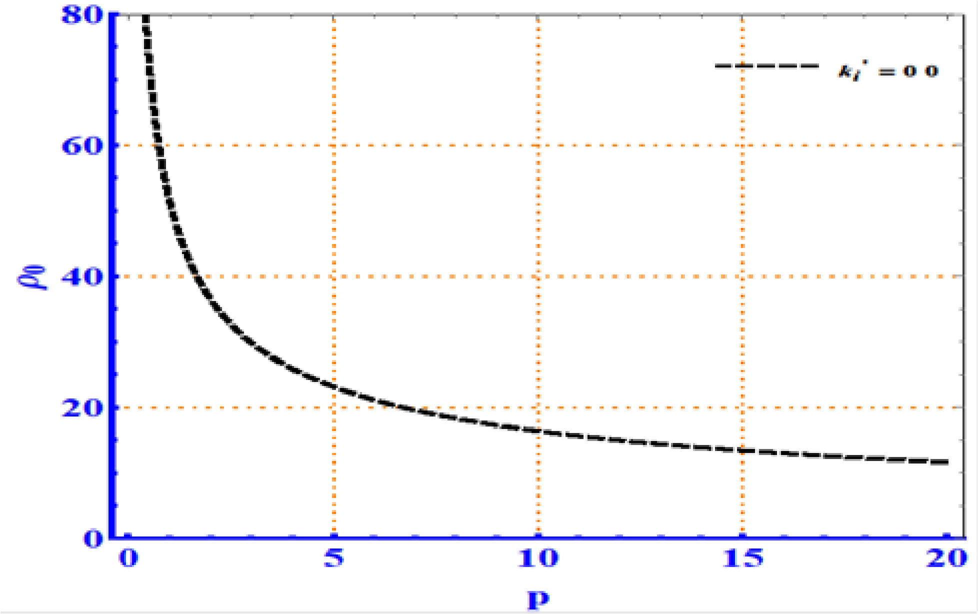

Figure 1: Dependence of normalized equilibrium beam radius ρ_0 as a function of initial intensity parameter p. ω_p = 1.7760 × 1015 rad/s,   r_0 = 20 × 10-4 cm,   n0 = 1018 cm–3,   ρ_0=65,  p = αE0 2  = 10.

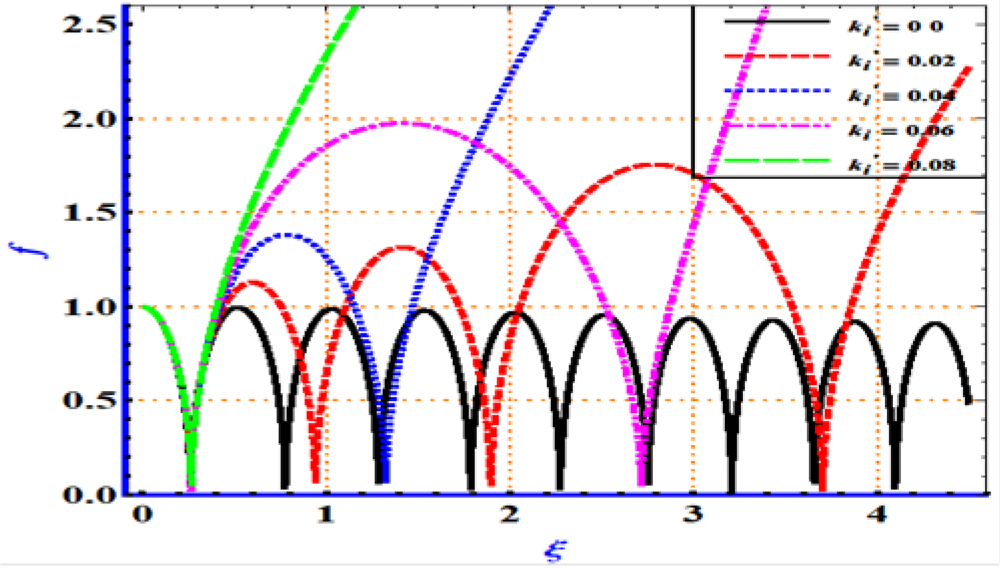

Figure 2: Variation of beam-width parameter f as a function of normalized propagation distance  for different linear absorption coefficients in collisionless plasma (k_i^'=0.00,0.02,0.04,0.06,0.08).

Figure 1 shows critical curve which is plotted from Equation (10). In figure 1 three distinct regions are observed. The region above the critical curve (supercritical region) corresponds to self-focusing region while the region below the critical curve (subcritical region) corresponds to defocusing region and for any point on the critical curve the self-trapping of the laser beam is observed. Figure 2 shows the variation of beam-width parameter f as a function of normalized propagation distance  for different absorption coefficients in collisionless plasma (k_i^'=0.00,0.02,0.04,0.06 and 0.06). In figure 2 for k_i^'=0.00, i.e. in the absence of linear absorption, the oscillatory self-focusing of the laser beam in collisionless plasma is observed. By taking into consideration the absorption, the self-focusing of the laser beam gets destroyed. As a result, the linear absorption defeats the effect of self-focusing, and the beam subsequently becomes too weak to control diffraction, resulting in quick divergence due to high energy attenuation. The longer propagation of laser beam in plasmas decreases due to absorption. In presence of absorption alone the energy of the beam decreases as 〖 exp〗⁡(- 2k_i z), which is equivalent to a weakening of the nonlinearity effect.

## IV. CONCLUSION

We have studied the effect of linear absorption on the self-focusing of Gaussian laser beam propagating through collisionless plasma by using parabolic equation approach under WKB and paraxial approximations. The following important conclusions are drawn from the present analysis:

- In the propagation dynamics of the laser beam in collisionless plasma, the controlling factors such as linear absorption coefficient, equilibrium beam radius, and initial intensity parameter play a vital role.
- With an increase in linear absorption in collisionless plasma, the self-focusing effect weakens.

The present results are of importance in various laser-plasma applications, where propagation of laser beam with confined energy over several Rayleigh lengths is required.

Acknowledgement: Authors are thankful to DST-PURSE Phase-II (2018-2023) and UGC DSA -Phase II (2018-2023) Programme for providing research facilities at Dept. of Physics, Shivaji University, Kolhapur, M.S., India.

## V. REFERENCES

[1]. Prof. Franken, P. A., Hill, A. E., Peters, C. W. and Weinreich, G. Phys. Rev. Lett. 7, 118–119 (1961).
[2]. Armstrong, J. A., Bloembergen, N., Ducuing, J. and Pershan, P. S., Phys. Rev. 127, 1918–1939 (1962).
[3]. Sodha, M. S., Ghatak, A. K. and Tripathi, V. K., Tata McGraw-Hill, New Delhi, (1974).
[4]. Akhmanov, S. A., Sukhorukov, A. P. and Khokhlov, R. V. , Sov. Phys. Uspekhi 10, 609–636 (1968).
[5]. Sodha, M. S., Ghatak, A. K. and Tripathi, V. K. , Prog. Opt. 13, 169–265 (1976).
[6]. Nayyar, V. P. and Soni, V. S., J. Phys. D. Appl. Phys. 12, 239–247 (1979).
[7]. Takale. M.V, Navare. S.T, Patil. S.D, Fulari. V.J. & Dongare. M.B, Opt. Commun. 282, 3157–3162 (2009).
[8]. Valkunde. A.T., Vhanmore. B.D., Urunkar. T.U., Gavade. K.M., Patil. S.D. and Takale. M.V., AIP Conf. Proc. 1953, 140088, (2018).
[9]. Sodha. M. S. and Sharma, A., Phys. Plasmas 13, 053105 (2006).
[10].Patil. S.D, Takale. M.V, Fulari. V. J., Gupta. D. N. and Suk. H., Appl. Phys. B Lasers Opt. 111, 1–6 (2013).
[11].Patil, S.D., Takale, M.V., Navare, S. T., Dongare, M. B. and Fulari, V. J., Optik 124, 180–183 (2013).
[12].Patil, S.D. and Takale, M.V. , Phys. Plasmas 20, 072703 (2013).
[13].Patil, S.D. and Takale, M.V., Phys. Plasmas 20, 083101 (2013).
[14].Aggarwal, M., Kumar, H. and Kant, N., Optik 127, 2212–2216 (2016).

[15].Navare. S.T, Takale. M.V, Patil. S.D, Fulari. V.J. & Dongare. M.B, Opt. Lasers Eng.50,1316–1320 (2012).

[16].Wani. M.A. and Kant. N., Commun. Theor. Phys. 66, 349–354 (2016).

[17].Ouahid. L., Dalil-Essakali, L. and Belafhal, A., Opt. Quantum Electron. 50, (2018).

[18].Kashyap. R, Aggarwal. M, Gill. T.S, Arora. N.S, Kumar. H. and Deepshikha. M., Optik 182, 1030–1038 (2019).

[19].Urunkar. T.U., Gavade. K.M., Vhanmore, B.D., Valkunde. A.T., Patil. S.D. and Takale. M.V., AIP Conf. Proc. 2142, (2019).

[20].Gavade. K.M., Vhanmore. B.D., Valkunde. A.T., Urunkar. T.U., Patil. S.D. and Takale. M.V., AIP Conf. Proc. 2142, 110016 (2019).

[21].Vhanmore. B.D., Takale. M.V. and Patil. S.D., Phys. Plasmas 27, 063104, (2020).

[22].Patil. S.D., Navare. S.T., Takale. M.V. and Dongare. M.B., Opt. Lasers Eng. 47, 604–606 (2009).

[23].Patil. S.D., Takale. M.V. and Gill, T.S., Eur. Phys. J. D 69: 163, (2015).

[24].Patil. S.D. and Takale. M.V., AIP Conf. Proc. 1728, 020129 (2016).

[25].Patil. S.D., Valkunde. A.T., Vhanmore. B.D., Urunkar. T.U., Gavade. K.M., Takale. M.V., AIP Conf. Proc. 1953, 140046 (2018).

International e-Conference on Recent Trends in Nano-Materials and Its Applications
In Association with International Journal of Scientific Research in Science and Technology
Volume 9 | Issue 11 | Print ISSN: 2395-6011 | Online ISSN: 2395-602X (www.ijsrst.com)

# Simulations Commercial BJT with Temperature for Space and Radiation Rich Environment Applications

**C M Dinesh[1]*, K S Krishna Kumar[2], M Sathish[3], R. Chandrashekar[1], Shivaprakash Y[4]**
[1]Department of Physics, Govt. First Grade College and PG centre, Chintamani-563125, Karnataka, India
[2]Department of Physics, Raja Rajeshwari College of Engineering, Bengaluru-560074, Karnataka, India
[3]Department of Physics, Govt. First Grade College, Doddaballapur – 561203, Karnataka, India
[4]Department of Physics, Govt. First Grade College, Devanahalli – 562110, Karnataka, India

## ABSTRACT

The temperature variations on electronic circuits employed to onboard plays a significant impact. In this investigation silicon NPN BJT response to irradiation has been studied at room temperature and temperature variation. A temperature variation dependent analytical model for total ionising dose induced excess base current in BJT's is tested. In this model base current dependent on temperature in irradiation parts have been captured. During irradiation all the three terminals of the devices are grounded. After irradiation, the base current is captured and the concentrations of oxide defects like oxide trapped charges and interface traps created during irradiations are calculated using simulated monte-carlo programming. The base current and defect density resulting from room temperature irradiations are used as inputs to simulations and analytical model experimental data obtained from measurements at room temperature and high temperature on irradiation parts are compared with the simulated results. This work shows that the simulations can support qualifications of the chosen devices for space applications and are functional at various temperatures.

**Keywords:** Bipolar Transistor, NPN, Temperature, Total ionizing dose, Base current.

## I. INTRODUCTION

Bipolar circuits used for comparators and regulators used for large percentage of a space system's are important to understand as a part invention. The operation of the components used for these circuits can be significantly degraded by Total Ionizing Dose (TID) [1]. It has been observed that Low Dose Rate (LDR) Irradiation causes more degradation than High Dose Rate (HDR) Irradiation, for the same TID [2]. Space is a Low Radiation Dose Rate (LDR) environment. Since LDR exposures required long test time, part qualification at this rate can introduce prohibitively high costs to mission assurance. Due to this, the identification of numeral models, accelerated techniques, and test method to assist in the characterization of LDR sensitivity in linear bipolar circuits [3] has been proposed. BJT's and Bipolar circuits show degradation mainly due to emitter – base interface traps ($N_{IT}$) and passivation layer oxide trapped charge ($N_{OT}$) defect build up in oxides.

These build up defects in BJTs can increase recombination at the bipolar base surface can lead to an increasing in the base current ($I_B$)[3].

In this paper we describe the temperature dependence of BJTs current voltage characteristics after the irradiation with 108 MeV Si$^{8+}$ ions. We also calculate the defects produced in the irradiation region using Monte-Carlo code (SRIM- Stopping and range of ions in matter). These results has been correlated to electrical degradation.

## II. EXPERIMENTAL METHODS

### BJTs Device and Oxide Defects

The transistors considered for this study are of vertical NPN BJTs the experimental devices were fabricated in BEL (Bharath Electronics Limited, India). Radiation-induced degradation due to defects that build up in base bipolar oxides alter surface recombination, which results in the increase of base current in NPN BJTs. These defects are net positive oxide trapped charge ($N_{DT}$) and interface trap ($N_{IT}$). The data obtained from (SRIM) and data from the transistors were used to extract Non Ionising Energy Loss (NIEL) calculations as a function of TID.

### SRIM Data

**Table 1** SRIM simulated results for 110 MeV Si ion irradiation on silicon target.

| **Parameter** | **Value** |
|---|---|
| R (μm) | 39.62 |
| $S_e$ (MeV cm$^2$/mg) | 10.21 |
| $S_n$ (MeV cm$^2$/mg) | $7.698\times10^{-03}$ |
| NIEL up to R (MeV cm$^2$/g) | 42.67 |

| **Fluence (ions/cm$^2$)** | **5x10$^9$** | **1x10$^{11}$** | **1x10$^{12}$** | **1x10$^{13}$** |
|---|---|---|---|---|
| TID (rad) | 0.8174 | 16.348 | 163.482 | 1634.82 |
| $D_d$ (rad) | 3143.4 | 68268 | $6.8268\times10^5$ | $6.8268\times10^6$ |

Table 1 depicts that the nuclear energy loss of 110 MeV Si$^{8+}$ ion is much smaller than the electronic energy loss (3 orders of magnitude, Table. 1) in a Si-target material due to smaller elastic scattering cross-section. Therefore the maximum energy deposited to the material is expected mainly due to the electronic energy loss during its passage through the Si-material [5]. The device suffers non-uniform irradiation effects as the projected ion range (39.46 μm) is lower than the device thickness (~ 600 μm) and it is expected to implant at base-collector region. The damage caused due to the linear energy transfer [LET = $S_e + S_n$ ~ 10.2177 MeV/(mg/cm$^2$)] in the Si target is obtained using TRIM calculations. LET dependent TID and NIEL dependent $D_d$ are tabulated in table 1.

### Pre-and post-irradiation test results

Radiation testing was performed at Inter University accelerating Centre (IUAC) New Delhi, India. Three devices were irradiated at room temperature (RT) LDR irradiation was performed 1PNA (particle nano ampere current) to get desired irradiation fluence. The energy of irradiating ion as choosing so that it could penetrate into emitter base junction.

The fluence has been calculated by counting the charge collected at the Faraday cup placed at the target. The anther advantage of selecting low irradiation current is that BJTs are not damage due to the loss of irradiated ion energy (110 MeV $Si^{8+}$ heavy ion) in the BJTs, (Heating effect will not be produced/the heat produced during the irradiation get transferred to the target).

Figure.1 show the base current $I_B$ responses exposed at 110 MeV $Si^{8+}$ ions for NPN BJTs. The data in these plots were collected at room temperature, 50 and 100 $^0$C. The increase in base current with radiation can be fit approximately to

$$\Delta I_B = I_{SE}\exp\left(\frac{q|VBE|}{n_E\, kT}\right), \qquad (1)$$

Where $I_{SE}$ is the radiation-induced change in low-injection base leakage current, $n_E$ is the change in the low injection ideality factor, k is Boltzmann's constant , T is the junction temperature, and q is the magnitude of electronic charge. Plots of $I_B$ and $V_{BE}$ at constant $V_{CE}$=4V.

**Temperature data on BJT devices**

Figure 1 – 3 shows the temperature dependent base current as a function of base – emitter voltage measured for un-irradiated and irradiated NPN BJTs to characterize the impact of thermal variation prior to and after ionizing radiation dose. The temperature testing was performed approximately 300 months after the radiation tests. No significant change was observed in the electrical response at room temperature between the end of the radiation testing and temperature testing. This showed that the defects produced during irradiations are permanent. Pre- and post unirradiated and irradiated devices were placed in a thermal chamber (hot air oven) with an internal thermocouple to automatically monitor the temperature near the devices during the tests. Temperature response testing was performed from 27 °C up to a maximum temperature of 100 °C in order to avoid annealing effects. Temperatures above 100 °C may lead to the annealing of some oxide defects (both interface and oxide traps) and a reduction in the excess base current measured for BJT [4]. Electrical measurements are performed a few minutes after the temperature is fixed in order to ensure thermal equilibrium during measurement. Each devices has been tested for electrical measurements before and after irradiation in order to test the effect of irradiation, it has been observed all devices show approximately same I-V characteristics before and after irradiation. Hence one devices were tested for each condition, electrical characterization at room temperature were performed after each temperature step in order to ensure no significant temperature dependent annealing of the parts of NPN BJTs [5].

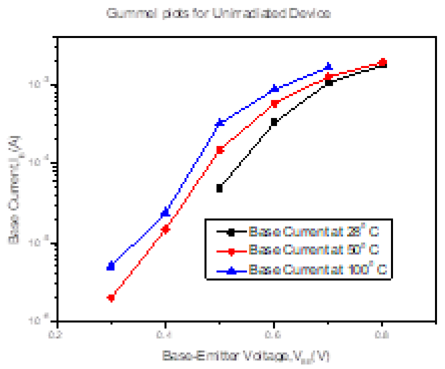

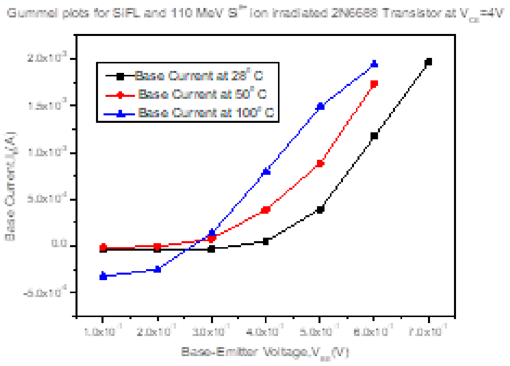

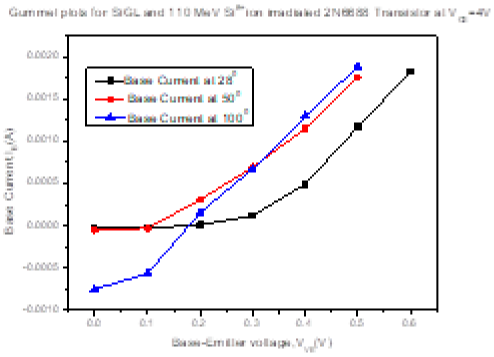

Figure. 1, 2 and 3 show the pre-irradiation, 1×10$^{11}$ and 1×10$^{12}$ ions/cm$^2$ LDR irradiated base currents for NPN BJTs over the specified temperature range (27$^0$, 50$^0$C 100$^0$C).

It can be observed that both the pre- and post-irradiated PNP BJTs show similar trends, i.e., a monotonic increase in base current with increasing temperature. Similar trend can be observed for the pre- and post-irradiated NPN BJTs. Most of the earlier studies have indicated that the impact of displacement damage is marginal compaed with the total dose effect. However, it has been shown that total – dose irradiation may indirectly affect the silicon substrate by reducing the active p-type base dopant concentration, may lead to an increase in base current as shown in figure 4.

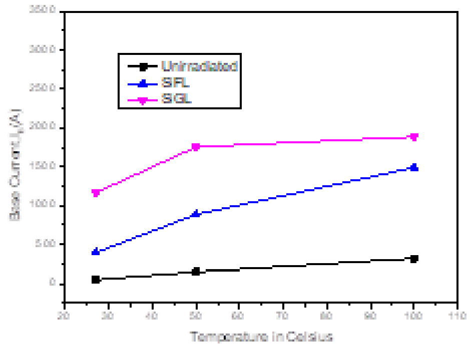

Figure. 4 show the base currents at |$VBE$| = 0.5 V as a function of temperature for un-irradiated and irradiated NPN BJTs respectively.

Table 2: Variation in base current, $I_B$ of BJT tested for different fluence of 110 MeV $Si^{8+}$ ions at specified temperature range ($27^0$, $50^0$C $100^0$C)

| **Temperature** | | **$I_B$(A)** | | |
|---|---|---|---|---|
| **$^0$C** | **Un irradiated** | **$5\times10^9$** | **$1\times10^{11}$** | **$1\times10^{12}$** |
| **27** | **48.66** | **126.666** | **394.66** | **1165.66** |
| **50** | **147** | **161** | **884** | **1755** |
| **100** | **317.66** | **3200** | **1488.33** | **1885.333** |

The enhabced $I_B$ is related to an increase in the surface recombination velocity, as the density of electrons and holes is coming more comparable, due to base neutralization. From the figure we can also see that there are large increase in the base current tested at higher temperatures ($50^0$C and $100^0$C) due to increased surface recombination current at the base surface. An increase in the midgap-lavel interface-trap density in the low-field, thick oxide over the p-type base increases the recombination current, more importantly an increase in the positive-oxide-charge density modulates the base surface potential to even more strongly increases the surfaces recombination current [6-9].

The current gain of modern bipolar transistors in an ionizing radiation environment decreases due to increased recombination in the emitter-base depletion region [7-8,10-11]. The recombination centers are related to the net charge introduced into the oxide by ionizing radiation, since it is positive the depletion region spreads on the p-side of a PN junction. For NPN transistors, this means that the deplition region seperatres into relatively lightly dopped P-type base region. As the deplition region increases in size, recombination current increases at the oxide interface over the base and in the newly-deplitted silicon bulk. In BJTs the excess basee current depends on the number of interface states (recombination centers) near midgap and threshold. The excess base current due to changes in surface potential depends on the total radiation induced oxide charge at the bias condition these variations in excess base current is as shown in table 2.

## III. CONCLUSIONS

This work reports the effect of 110MeV $Si^{8+}$ ion irradiation on silicon NPN transistors devices with fluences of $5\times10^9$ ions $cm^{-2}$ to $1\times10^{13}$ ions $cm^{-2}$. An effort is made successfully to correlate the electrical degradation with the non –ionizing energy deposition due to MeV ion irradiation using TRIM Monte Carlo Code. Fluence dependent TID and $D_d$is calculated for 100 MeV silicon ion in silicon target. The shift in collector saturation current and collector emitter voltage is mainly due to the total displacement dose. In addition to these shifts, Si-ion irradiation causes increase in forward resistance of the collector emitter region.

The current gain of the transistors decreases with increases in silicon ion fluences. It has in addition been observed that the base current increases with increase in TID and test temperature. The excess base current due to changes in surface potential depends on the total radiation induced oxide charge at the bais condition. This is again related to the reduction of the base doping concentration after exposure. In BJTs the excess base current depends on number of interface traps (recombition centres) near the midgap. At higher total doses, sufficient charge as the accumulated in the oxide to cause significant recombination to occur through-out the lightly doped based region. The swift heavy ion irradiation on silicon will result in increase in lattice temperature. Hence in the present device case the transistor performance is severely affected due to silicon ion irradiation. The switching time of the transistor may decrease due to an increased base currents as a function of silicon ion fluence.

## IV. REFERENCES

[1]. H.J. Barnaby, R.D. Schrimpf, R.L. Pease, P Cole, T.Turflinger, J.Krieg, J.T.Titus, D. Emily, M. Gehlhausen, S.C. Witczak, M.C. Maher, D.Van Nort, Identification of degradation mechanisms in a bipolar linear voltage comparator through correalation of transistor circuit response, IEEE Trans, Nucl. Sci. 46(6)(Dec.1999) 1666-1673.

[2]. A.H. Johnston, B.G. Rax, C.I. Lee, Enhanced damage in linear bipolar integrated circuits at low dose rate, IEEE Trans. Nucl.Sci. 42(6)(Dec 1995)1650-1659.

[3]. P.C. Adell, R.L. Pease, H.J. Barnby, B.Rax, X.J. Chen, S.McClure, Irradiation with molecular hydrogen as an accelerator total dose hardness occurrence test method for bipolar linear circuits, IEEE Trans. Nucl. Sci. 56(6)(Dec.2009) 3326-3333.

[4]. X.Li,W.Lu, Q.Guo, D.M. Fleetwood, C.He, X.Wang, X.Yu, J.Sun, M.Liu, S.Yao, Temperature-switching during irradiation as a test for ELDRS in linear bipolar devices, IEEE trans. Nucl. Sci.66(1)(Jan. 2019)199-206.

[5]. H.J. Barnaby, B.Vermeire, M.J. Campola, Improved model for increased surface recombination current in irradiated bipolar junction transistors, IEEE Trans Nucl. Sci.62(4)(Aug.2015) 1658-1664.

[6]. B.S. Tolleson, P.G. Adell, B.Rax, H.J. Barnaby, A.Privat, X.Han, A.Mahmud, I.Livingston, Improved model for excess base current in irradiated lateral PNP bipolar junction transistors, IEEE Trans. Nucl.sci, Aug,2018.

[7]. C. M. Dinesh, Ramani, M. C. Radhakrishna et al., Nucl. Instr. and Meth. in Phys. Res. B 266, (2008) 1713.

[8]. K.S. Krishnakumar, C.M. Dinesh, KV Madhu, et al., Carbon ion irradiation damage effects on electrical characteristics of silicon PNP power BJTs, IEEE Trans. On Device and Mat. Relia. 15 (1), (2015), 101-108.

[9]. R. Nathan Nowlin, D. M. Fleetwood, and R. D. Schrimpf, IEEE Trans. Nucl. Sci. 41, (6), (1994) 2637.

[10]. R. L. Pease, R. M. Turfler, D. Platteter, D. Emily, and R. Blice, IEEE Trans. Nucl. Sci. NS-30, (1983) 4216.

[11]. A. R. Hart, J. B. Smyth Jr. V. A. J van Lint, D. P. Snowden, and R. E. Leadon, IEEE Trans. Nucl. Sci. NS-25, (1978) 1502.

[12]. J. Boch, F. Faigne, T. Maurel, F. Giustino, L. Dusseau, R.D. Schrimpf, K.F. Galloway, J. P. David, R. Ecoffet, J. Fesquet et.al. IEEE Trans. Nucl. Sci. 49, (3), (2002) 1474.

International e-Conference on Recent Trends in Nano-Materials and Its Applications
In Association with International Journal of Scientific Research in Science and Technology
Volume 9 | Issue 11 | Print ISSN: 2395-6011 | Online ISSN: 2395-602X (www.ijsrst.com)

# Green Synthesis and Characterization of CDS Quantum Dots Mediated by Aegle Marmelos Leaves

**M.D. Dhiware1, T.R. Deore2, S.B. Nahire3, A.B. Gawande2***
[1]Department of Physics, KVNN Arts, Commerce and Science College, Nashik, Maharashtra, India
[2]Department of Physics, K.S.K.W. Arts, Science and Commerce College, CIDCO, Nashik, Maharashtra, India
[3]Department of Physics, National Senior College, Nashik, Maharashtra, India

## ABSTRACT

Herein, we report the green synthesis of CdS quantum dots (QDs) by Aegle Marmelos leaves extract. Green synthesis method is novel, simple, eco-friendly, nontoxic compared to conventional physical and chemical methods. Aegle Marmelos used as a capping and reducing agent owing to their extraordinary medical applications. The synthesized CdS QDs characterized by various characterization techniques Such as X-Ray Diffraction (XRD) showing cubic structure with average particle size about 4 nm determined by using Debye Scherrer formula. Field emission scanning electron microscope (FE-SEM) reveals a spherical shape of CdS QDs.

## I. INTRODUCTION

In past two decades green synthesis method is drawing more attention owing to its facile, nontoxic, eco-friendly and low temperature characteristics compared other methods. Green synthesis approach uses bioactive agents such as plant materials, microorganism and various biogases etc. The various nanomaterials are synthesized by green method such as CdS, $CeO_2$, Ag, ZnS, SnO2 etc.[1-5]. There are different methods are used for synthesis of CdS QDs by like chemical deposition [6], Hydrothermal [7], Sol-Gel [8], etc. In this method uses the collides with harmful chemicals. These can be avoiding if we used green synthesis plant extract approach.

Cadmium sulfide (CdS) is a direct band gap semiconductor with energy band gap $E_g = 2.42$ eV. The colour tunability of semiconductor QDs as a function of size is one of their most attractive characteristics. CdS is a promising material because of their applications in optoelectronics, photocatalysts, x-ray detectors, nonlinear optical material and as a window material for hetro-junction solar cells [9].

*Aegle Marmelos* leaves contains broadly alkoids, prphynols, terepnoids and other polyphenols, which are well recognized for their healing power toward variety of bacterial and fungal infections [10]. In the present research work we report green synthesis of CdS QDs mediated by *Aegle Marmelos*.

## II. MATERIALS AND METHODS

Cadmium Chloride ($CdCl_2.H_2O$), Sodium sulphide ($Na_2S.H_2O$) and Ethanol are easily available commercial materials. *Aegle Marmelos* leaves were gathered from local trees. Distilled water used as solvent in the method.

### 2.1 Synthesis of CdS QDs:

CdS QDs synthesized greens approach, typical synthesis in 5 ml extract of *Aegle Marmelos* leaves added 90 ml of distilled water in the proceeding step 0.2 gm of $CdCl_2$ was added and placed on hot plate with magnetic stirring at temperature 100°C for 2 hrs. After that 0.078 gm of $Na_2S$ was added in the mixture and again kept for constant magnetic stirring for 2 hrs. Then final yellow colour product was filtered, centrifuged and finally dried at room temperature 12 Hrs. The final yellow powder was used for further characterisation.

## III. RESULT AND DISCUSSION

### X-ray Diffraction (XRD):

XRD pattern as shown in the figure 1. X-ray diffraction used to study crystal structure, nanoparticle size, interplanar spacing. The XRD peaks was found to be very broad which indicates formation of very small size QDs The diffraction peaks assigns at $2\theta = 26.9^\circ$, $46.78^\circ$ and $53.5^\circ$ which corresponds to the miller indices for the crystal plane of (111), (220) and (311) with cubic crystalline structures of synthesized CdS QDs, respectively, (JCPDS Card no.00-010-0454). XRD of prepared sample materials was found to be in good agreement with (JCPDS file no.00-010-0454). The average particle size was found to be 4 nm which was determined by using the Debye Scherrer formula i. e. nanoparticle size $(D) = (k\ \lambda)/\ (d\cos\theta)$ Where, D is the particle in nm, K is crystallite shape factor a good approximation is 0.9 for spherical shape nanoparticles, $\lambda$ is the X-ray wavelength used for X-ray diffraction, d is the full width at half the maximum (FWHM) in radians of the X-ray diffraction peak and $\theta$ is the Braggs' angle (deg.). [11]

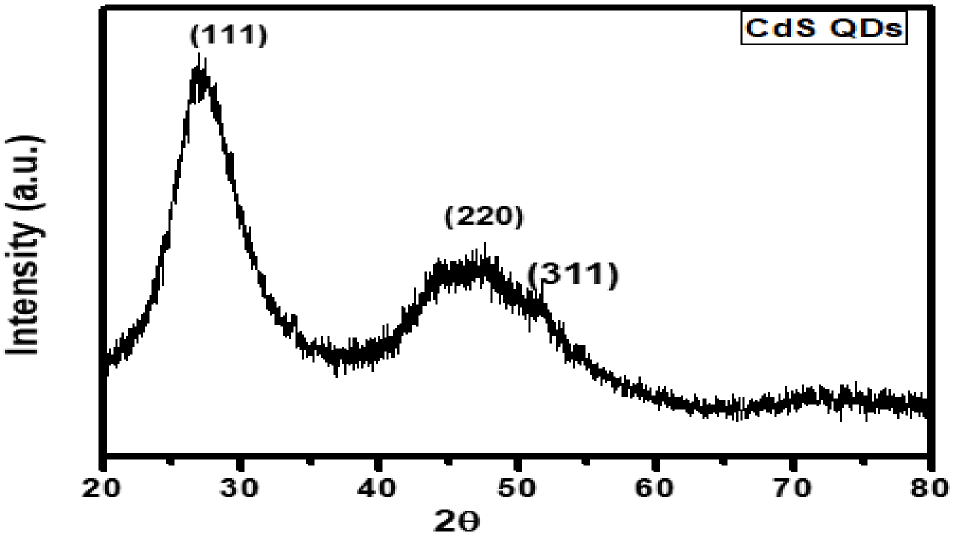

Figure 1: XRD pattern of CdS QDs

**Field Emission Scanning Electron Microscope (FESEM) study:**

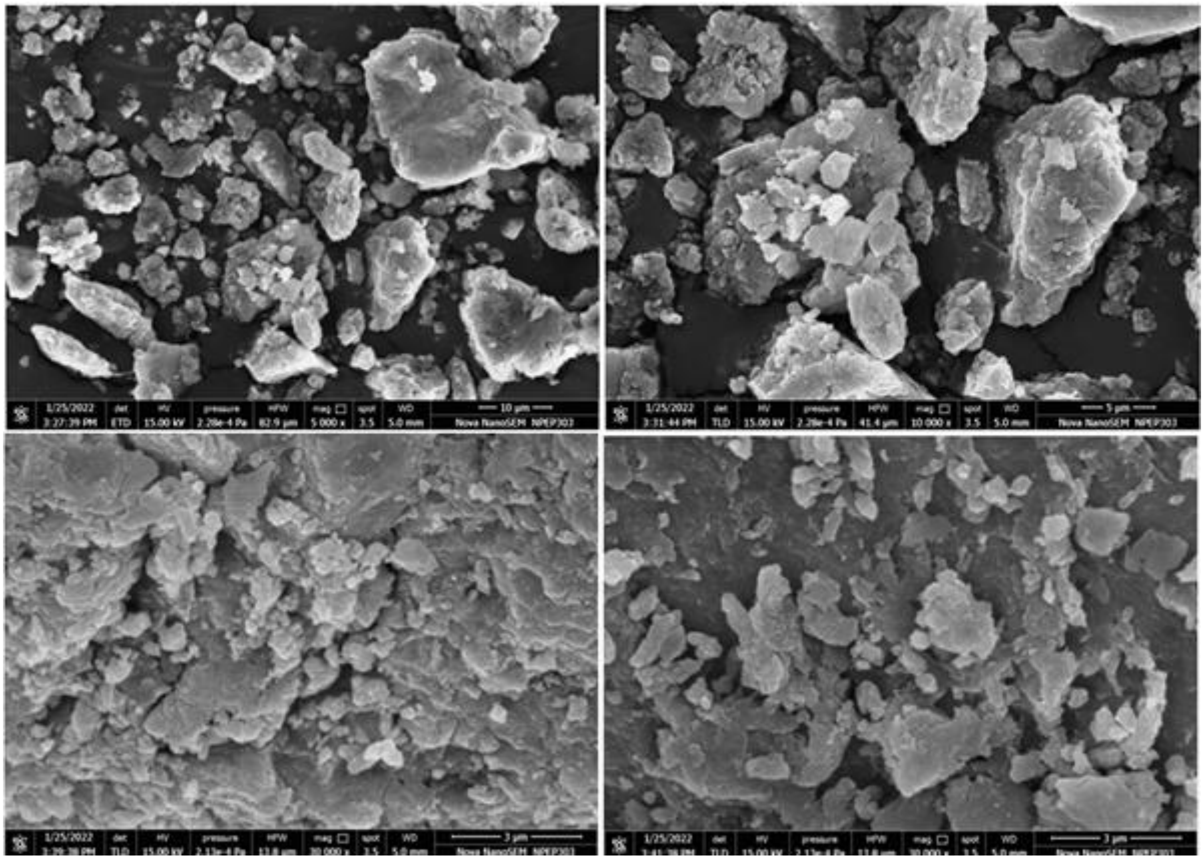

Figure 2: FESEM images of CdS QDs

The synthesized product of CdS QDs characterized by using FESEM technique which is used for the study of surface morphology. CdS QDs shows particles are nearly spherical in shape morphology with slightly agglomeration as shown in the figure 2.

## IV. CONCLUSION

In summary, plant mediated synthesis of nanoparticles have several advantages over physical and chemical methods..CdS QDs synthesized by green synthesis method with leaves extract of *Aegle Marmelos*. The leaves extract bioactive components play vital role for formation of CdS QDs Moreover, the prepared CdS QDs average nanoparticle size was found to be 4 nm determined by using XRD technique. Field emission scanning electron microscope (FE-SEM) reveals a spherical shape of CdS QDs with agglomerate morphology and. Synthesized CdS QDs can be explored for various biomedical applications such as antibacterial, antibiofilm, antifungal, antiviral, anticarcinogenic and anticandidal activities.

## V. ACKNOWLEDGEMENTS

Authors thanks to Principle, KSKW Arts, Science and Commerce College, Nashik for providing instrumental facilities to carry out this research work and Authors also wants to thanks to Vice Principle Dr. Latesh Nikam from Baburanji Gholap College, Sangvi, Pune for providing characterization facility.

## VI. REFERENCES

[1]. Prof. Biogenic synthesis of photocatalyic activity of CdS NPs, A. Bhadwal, et al. , RSC. adv, 2014,4,9484.
[2]. Green synthesis of CeO2 NPs from the abelmoschus esculentus Extract of antioxidant, Anticancer ,Antibacterial and wound- Healing Activities. H. E. Ahemad, et al. Molecules 2021,26,4659.
[3]. Green synthesis of silver NPs using white sugar, S. Mesharam , et al. IET Nanobiotechnology (2013), 7,1, 28-32.
[4]. Green synthesis of ZnO Using S.Frutesences Plant extract for photocatalytic degradation of dye and antibiotics S. Munjai, et al. Mate Res Express, 9, (2022), 015001.
[5]. Green synthesis of SnO2 NPs using delonaelataleaf: Evaluation of its structural, optical, morphological and photocatalytic properties. K.C.Suresh et al, SN applied science (2020)2:1735.
[6]. Photoaucstic study of CdS QDs for application in QDs sensitized solar cells. S. Abdallah, et al., Journal of nanomaterials,498286,1-6, 2012
[7]. One step of hydrothermal synthesis of thioglycolic acid capped CdS QDs as fluroscsnces determination of cobalt ion, Z. wang, et al Scientific Reports, (2018) 8:8953.
[8]. Sol Gel synthesis, characterization and effect of CdS nanoparticles on activity of liver Enzymes, Asmaa. J Al-lamei, Journal of Advanced Sciences and Engineering Technologies, 2019, 35-42.
[9]. W.V. Huynh, J.J. Dittmer, A.P. Alivisatos, "Hybrid nanorod-polymer solar cells", Science 295 (2002), 2425–2427.
[10].One-step biofabrication of copper nanoparticles from Aegle marmelos correa aqueous leaf extract and evaluation of its anti-inflammatory and mosquito larvicidal efficacy, Gangadhara Angajala, Pasupala Pavan and R. Subashini, RSC Adv., 2014, 4, 51459.
[11].Room Temperature Synthesis And Characterization Of Cadmium Sulphide (CdS) Semiconductor Quantum Dots, S.I. Khan, G.K.Kande, L.D.Sonawane, A. S. Mandawade, L.J. Jondhale, P.G.Loke, Journal of Scientific Research in Science and Technology,9,2, 2021.

International e-Conference on Recent Trends in Nano-Materials and Its Applications
In Association with International Journal of Scientific Research in Science and Technology
Volume 9 | Issue 11 | Print ISSN: 2395-6011 | Online ISSN: 2395-602X (www.ijsrst.com)

# Electrodeposited Nanoleaves (NLs) like $Mn_3O_4$ thin film for electrochemical supercapacitor

**P. M. Kharade[1*], J. V. Thombare[2], S. S. Dhasade[2], S. D. Patil[3], P.B.Abhange[4], D. J. Salunkhe[5]**

[1]Department of Physics, Shankarrao Mohite Patil Mahavidyalaya, Akluj, Dist-Solapur (MH), India 413101

[2]Department of Physics, Vidnyan Mahavidyalaya, Sangola, Dist-Solapur (MH), India 413307

[3]Department of Physics, Pratapsinh Mohite Patil Mahavidyalaya, Karmala, Dist-Solapur (MH), India 413203

[4]Department of Physics, G.M. Vedak College of Science, Tala, Raigad (MH), India 402111

[5]Nanocomposite Research Laboratory, K.B.P. Mahavidyalaya, Pandharpur, Dist-Solapur (MH), India 413303

*Corresponding Author E-mail:pravink150@gmail.com

## ABSTRACT

In the present study, we report here synthesis and characterization ofmanganese oxide ($Mn_3O_4$) thin films by potentiostatic electrodeposition for supercapacitor application. The structural and surface morphological behaviour of $Mn_3O_4$ thin film were carried out by using X-ray diffraction (XRD) and Scanning Electron Microscopy (SEM) study. The structural study of $Mn_3O_4$ thin film shows hausmannite tetragonal crystal structure. The surface morphological study showed that the formation of nanoleaves (NLs) of $Mn_3O_4$ thin film. The electrochemical supercapacitive performance of $Mn_3O_4$NLs was characterized by using cyclic voltammetry (CV), charging-discharging (CD) and electrochemical impedance spectroscopy (EIS) techniques. The $Mn_3O_4$NLs shows maximum specific capacitance of 460 $F.g^{-1}$ at scan rate 5 $mV.s^{-1}$and 92% cycling stability in 0.5 M $Na_2SO_4$ electrolyte solution. Hence, potentiostatically deposited $Mn_3O_4$NLs is best for energy storage application.

**Keywords:** supercapacitor, electrodeposition, $Mn_3O_4$, XRD, FESEM, CV.

## I. INTRODUCTION

In the 21th century more and more research focused on highly renewable and sustainable energy storage devices. Electrochemical capacitor or supercapacitor have gained more attention due to their excellent electrochemical properties such as, environmental friendly, fast charging and discharging rate, good reversibility, high power density, long cycle life and safety in operation. Due to this features electrochemical capacitor can be used in variety of potential applications such as, memory back up devices, portable electronic devices, hybrid electric vehicles, elevator, forklifts, cranes, lasers and industry [1-4]. The Electrochemical capacitor or supercapacitor mainly categorized into two typesviz, electrochemical double layer capacitor (EDLC) and Pseudocapacitor (PC). In EDLC, charge is stored electrostatistically, i.e charge accumulation takes place at the electrode/electrolyte interface. Example, carbon materials. In pseudocapacitor (PCs) faradic process takes place. Example, conducting polymers and Transition metal oxides (TMOs) etc. Electrode materials used in TMOs are $RuO_2$ [5], $MnO_2$ [6], $Co_3O_4$ [7], NiO [8], $IrO_2$ [9], $Cr_2O_3$ [10] and CuO [11] etc. Among these TMOs, Manganese oxide electrode is widely studied in supercapacitor because of better electrochemical performance, natural abundant, low cost, easy synthesis and non-toxic [12-13]. Manganese oxide also have several oxidation states such as, MnO, $MnO_2$, $Mn_2O_3$ and $Mn_3O_4$ etc. Among these oxides, $Mn_3O_4$ is one of the most stable state of manganese oxide and have attracted considerable attention due to its low cost, environmental friendly, natural abundant and good electrochemical properties [14-15].

Manganese oxide have been synthesized by different physical and chemical methods such as, hydrothermal method [16], co-precipitation method [17], sol-gel method [18], chemical bath deposition method [19], self-reacting microemulsion method [20], sonochemical method [21], electrodeposition method [22], room-temperature solid reaction [23] and SILAR method [24] etc. Among all the various methods, electrodeposition method is one of the best method for synthesis of metal oxides because of low cost, binder free, single step and large scale production. It also leads direct deposition of oxide/hydroxide electrodes on low cost substrates.Nguyen et al. [22] have reported nanoflakes like morphology of $Mn_3O_4$ thin film by cathodic electrodeposition method for supercapacitor application. Yousefi et al. [25] have reported porous nanospheres of $Mn_3O_4$ by cathodic electrodeposition method and studied their electrochemical properties. Porous and nanostructured material is key requirement for electrochemical capacitor because it provides large surface area, shorten the diffusion path of electrons and ions, which promotes the fast insertion and extraction of electrons and ions. Which improves the specific capacitance of the electrode [26].

In the present report, efforts have been taken to study structural, morphological and electrochemical supercapacitive behaviour of potentiostatically deposited $Mn_3O_4$ NLs for supercapacitor application.

## 2. Experimental:

### 2.2 (a) Characterization techniques

The crystal structural study of $Mn_3O_4$ NLs was carried out with the help of XRD using Bruker axes D8 Advance Model with copper radiation ($K_\alpha$ of $\lambda = 1.54\ A^\circ$) within 2θ range between $20^\circ$ to $80^\circ$. The surface morphology of$Mn_3O_4$ NLs was carried out by using field emission scanning electron microscopy (FESEM) technique (Model: JSM-6160). The electrochemical supercapacitive study of $Mn_3O_4$ NLs was studied by using CV, GCD and EIS techniques by using electrochemical workstation (CHI 660 A).The electrochemical cell includes three electrode systems. $Mn_3O_4$ NLs was used as a working electrode, graphite was used as a counter electrode and saturated calomel electrode (SCE) was used as a reference electrode. The 0.5 M $Na_2SO_4$ was used an electrolyte solution for overall measurements.

## 3. Result and Discussion

### 3.1 XRD Study:

X-ray diffraction (XRD) techniques have been carried out to examine the crystal structure of the $Mn_3O_4$ NLs. Fig.1 shows the XRD pattern of $Mn_3O_4$ NLs in the 2θ range from 20° to 80°. The observed diffraction peaks indexed in the XRD pattern of $Mn_3O_4$ NLs was well matched with JCPDs card no.89-4837. The XRD study shows hausmannite tetragonal crystal structure of electrodeposited $Mn_3O_4$ NLs. The peak marked with (SS) in the XRD spectrum is due to stainless steel substrate only.

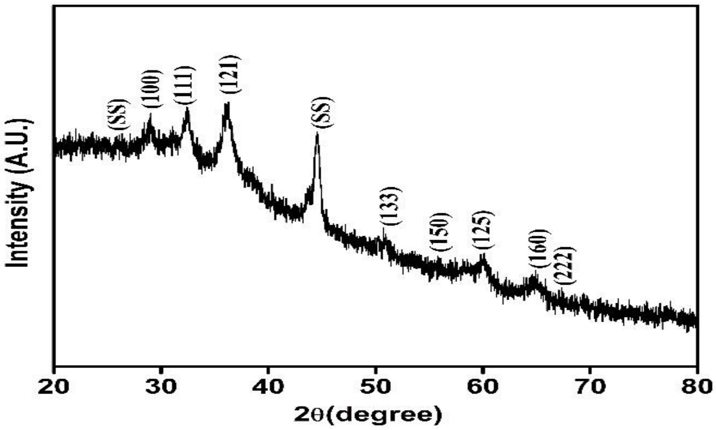

**Figure 1.** X-ray Diffraction (XRD) spectra of $Mn_3O_4$ NLs.

The average crystallite size of $Mn_3O_4$ NLs was calculated by using the Debye's Scherer's equation,

$$D = \frac{0.9\lambda}{\beta\cos\theta} \text{ ------- } (3)$$

Where, D is the crystallite size, λ is the wavelength of X-ray (1.54.4 A°) and β is full width at half maximum (FWHM).For determination of crystallite size, the most intense peak (121) is centered at FWHM in term of radian is 0.807. The crystallite size of $Mn_3O_4$ NLs is found to be 34 nm.

### 3.2. Surface Morphological Studies

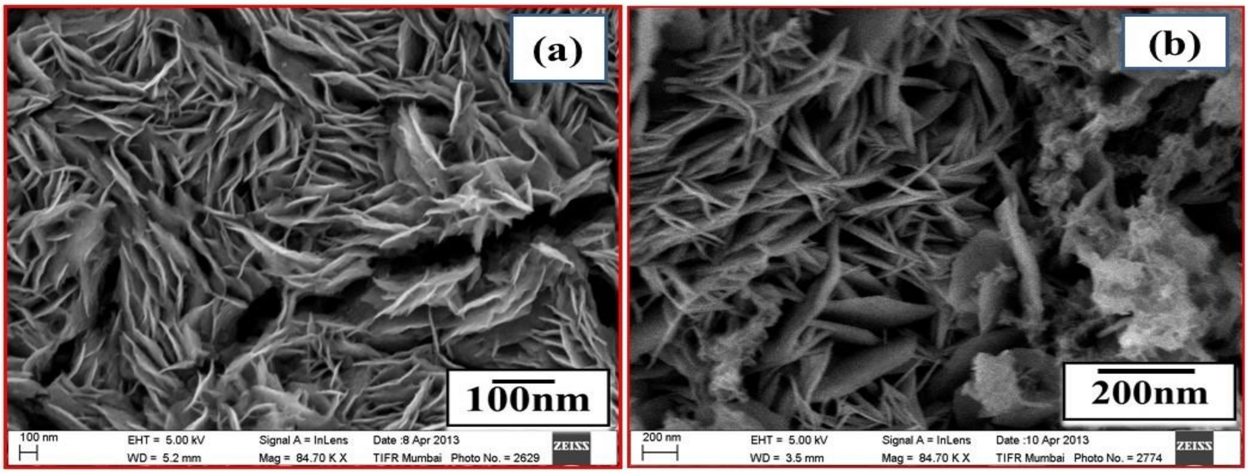

**Figure 2 :** Scanning Electron Microscope (SEM) images of $Mn_3O_4$ thin film at (a) 100kX and (b) 200kX magnifications respectively.

Surface morphology of the $Mn_3O_4$ NLs was studied by using FESEM technique. Fig. 2(a-b) demonstrate the FESEM micrographs of $Mn_3O_4$ thin film with two different magnifications (100 kX and 200 kX) respectively. In Fig. 2(a) SEM micrograph of $Mn_3O_4$ thin film at low magnifications shows the compact and nanoflakes like morphology [28]. At high magnification in Fig. 2(b), the $Mn_3O_4$ thin film gives highly resolved, porous and interconnected Nano leaves (NLs) like structure.Such structures have a larger specific surface area, providing the active material to sufficiently react with ions in the solution, and hence reducing the electron transport distance [29]. Therefore, it enhances the electrochemical supercapacitive properties.

### 3.3 Supercapacitive studies:

### 3.3.1 Cyclic voltammetry (CV) studies:

The specific capacity of $Mn_3O_4$ NLs was carried out by using CV study. Fig. 3(a) display typical CV curves of $Mn_3O_4$ NLs at different scan rates such as; 5, 10, 50 and 100 mV/s within potential limit of +1.2 V to -1.2 V vs SCE, respectively.From CV curves, it is observed that as scan rate increases current under curve increases and the cathodic and anodic peaks shifts more towards positive and negative sideward. This result shows that current is directly proportional to scan rate, i.e. scan rate dependent current-voltage indicate that ideal capacitive behaviour of $Mn_3O_4$ NLs. Similar results reported by Dubal and More et al. prepared by $Mn_3O_4$ thin film by chemical bath deposition and spray pyrolysis method for supercapacitor application respectively [19, 30].

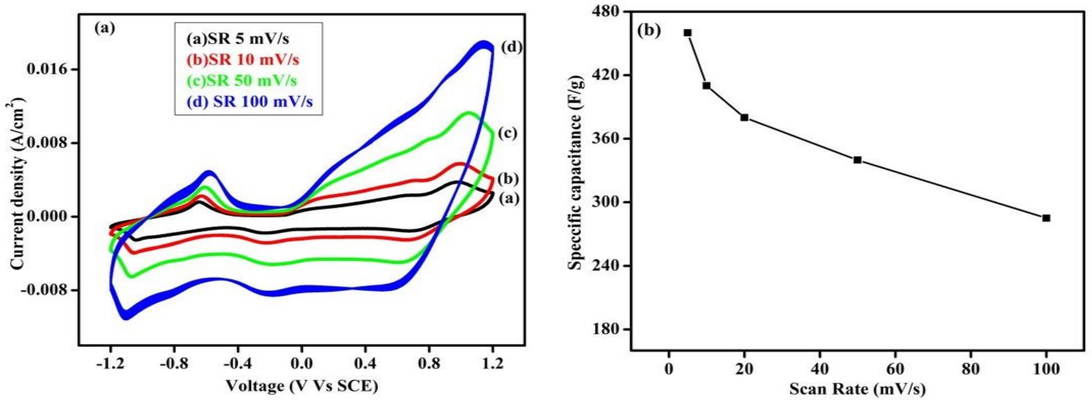

**Figure 3** (a) Cyclic Voltammetry (CV) study of $Mn_3O_4$ NLs at scan rate of 5, 10, 50 and 100 mV/s and 4 (b) Variation of specific capacitance vs scan rate of $Mn_3O_4$ NLs.

The capacitance of $Mn_3O_4$ thin film wascalculated by using the following relation,

$$C = \frac{\int Idt}{dv/dt} \text{ --------- } (4)$$

Where, ∫Idt is area under curve of CV and dv/dt is voltage scanning rate in mV/s.

The specific capacitance of $Mn_3O_4$ NLs was calculated by following relation,

$$\text{Specific capacitance } (C_s) = \frac{C}{W} \text{ ------ } (5)$$

Where, C–capacitance in farad and W – the mass of active electrode materials in gm.The active mass of $Mn_3O_4$ NLs was 0.0024 gm, calculated from weight difference method. The $Mn_3O_4$ NLs show specific capacitance of 460 F.g$^{-1}$ at scan rate of 5 mV.s$^{-1}$. It was observed that as scan rate increases specific capacitance decreases shown in Fig. 3 (b). Decrease in specific capacitance suggests that at higher scan rate most of the inner active sites of nanoflakes network are not involved in the reaction. So, specific capacitance obtained at low scan rate are due to full utilization of the active electrode materials.

| Material | Specific Capacitance (F.g$^{-1}$) | Electrolyte | Method of synthesis | Reference |
|---|---|---|---|---|
| $Mn_3O_4$ Nano leaves | 460 | 0.5 M $Na_2SO_4$ | Potentiostatic Electrodeposition | Our work |
| $Mn_3O_4$ nanoparticles | 375 | 1.0 M $Na_2SO_4$ | SILAR | [31] |
| $Mn_3O_4$ nanocubes | 223 | 1.0 M $Na_2SO_4$ | CBD | [32] |
| $Mn_3O_4$ nanograins | 314 | 1.0 M $Na_2SO_4$ | SILAR | [24] |
| $Mn_3O_4$ nanograins | 289 | 1.0 M $Na_2SO_4$ | SILAR | [33] |

**Table: 1**Comparison of specific capacitance between our work and previously reported work to synthesis the $Mn_3O_4$ electrodes by considering scan rate of 5 mV/s.

Table 1 represents a comparison of specific capacitance between our work and previously reported work by keeping scan rate of 5 mV/s vs SCE. The specific capacitance obtained in the present study is higher due nanostructured and porous morphology of $Mn_3O_4$ NLs.It depends upon optimum electrodeposition time.

### 3.3.3Galvanostatic charging-discharging (GCD) studies:

The specific energy and specific power associated with $Mn_3O_4$ NLs was carried with the help of GCD techniques. Fig 4 (a) shows typical charge-discharge curves of $Mn_3O_4$ NLs at constant current density of 5 mA.cm$^{-2}$ in 0.5 M $Na_2SO_4$ electrolyte solution. The charging-discharging curves of $Mn_3O_4$ NLs show symmetrical characteristics, which reveals that $Mn_3O_4$ NLsthin film have good capacitive behaviour and the reversible redox process.The GCD curve of $Mn_3O_4$ NLs shows very small voltage drop at the initial of the discharge curve which is due to very low internal resistance between the current collector and $Mn_3O_4$ NLs.

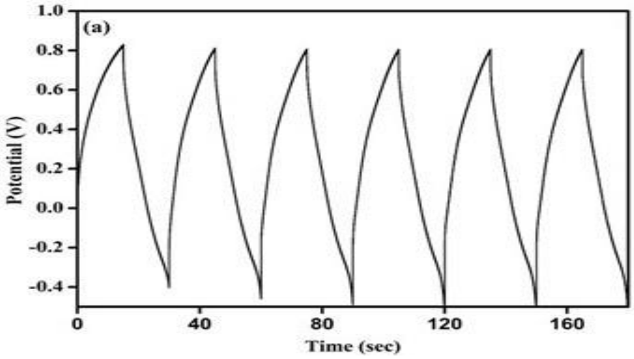

**Figure 4** Galvanostatic charge-discharge (GCD) study of $Mn_3O_4$ NLs

The coulombic efficiency, specific energy and power of $Mn_3O_4$ NLs was calculated using following formulae:

Coulombic Efficiency $(\eta) = \frac{T_d}{T_c} x100$ ----------- (6)

Specific power $(P) = \frac{V \, X \, I_d}{W}$ ---------------(7)

Specific energy (E) $= \frac{V\,X\,I_d X\,T_d}{W}$ ------------- (8)

Where, $T_d$and $T_c$ is discharge and charge time in sec, V is voltage window in volt, $I_d$ is discharge current mA and W is the mass of the active material in gm.The coulombic efficiency of $Mn_3O_4$ NLs was found to be 98.42% whereas the specific power and specific energy were observed to be 6.40 kW.kg$^{-1}$ and 3.85 Wh.kg$^{-1}$, respectively.

## 4. Conclusions:

In summary, we have successfully synthesized $Mn_3O_4$ NLs by electrodeposition method on low cost conducting stainless steel substrate for supercapacitor application. The XRD study reveals that hausmannite tetragonal crystal structure with average crystallite size of 34 nm. The surface morphology study $Mn_3O_4$ thin film shows NLs type morphology at higher magnification. The electrodeposited $Mn_3O_4$NLsshows higher specific capacitance of 460 F.g$^{-1}$ with 92% cyclic stability, which is better achievement than earlier reported values because of nano structured materials. The GCD study shows better values specific energy and specific power and coulombic efficiency of $Mn_3O_4$NLs. EIS study reveals that small values of $R_s$ and $R_{ct}$ of $Mn_3O_4$NLs based thin film electrode, providing better ability of electronic and ionic conductivity of $Mn_3O_4$materials. Thus, electrodeposited $Mn_3O_4$NLs based thin film electrode is suitable material for electrochemical supercapacitor device.

## References:

[1] G. Wee, W.F. Mak, iN. Phonthammacha, A. Kiebele,M.V. Reddy, B.V.R. Chowdari, G. Gruner, M. Srinivasan,
S.G.Mhaisalkar, J. Electrochem. Soc. 157,A179 (2010)
[2]J.K. Chang, Y.L. Chen, W.T.T.Sai, J. Power Sources. 135,344(2004)
[3] P. Simon, Y.Gogotsi, Nat. Mater. 7,845(2008)
[4]D. Wei, Scherer MR, Bower C, Andrew P, Ryhanen T, U.Steiner, Nano Lett.12,1857 (2012)
[5] K.H. Chang,C.C. Hu,C.Y.Chou, Chem. Mater.19,2112 (2007)
[6]Z. Yu,B. Duong,D. Abbott, J.Thomas, Adv. Mater.25, 3302(2013)
[7] P.M. Kharade, J.V. Thombare, A.R. Babar, R.N. Bulakhe, S.B. Kulkarni, D.J.Salunkhe, J Phys Chem Solids. 120,207(2018)
[8]L. Gu,Y. Wang, R. Lu, L. Guan,X. Peng, J.Sha J. Mater. Chem. A. 2,1761(2014)
[9] D.Q. Liu, S.H. Yu, S.W. Son, andS.K.Joo, ECS Trans.16,103(2008)
[10] P.M. Kharade, A.R. Babar, S.S. Dhasade, B.R. Karche, D.J. Salunkhe, Mater. 7, 342(2018)
[11]A.S. Patil, M.D.Patil, G.M.Lohar, S.T. Jadhav, V.J. Fulari, Ionics. 23, 1259 (2017)
[12] S.F. Chin, S.C. Pang, and M.A. Anderson,J. Electrochemical Society. 149, A379 (2002)
[13]S.F. Chin, and S.C.Pang, Mater. Chem. Phys.124,29 (2010)
[14]X. Zhang, X. Sun,Y. Chen,D. Zhang,Y.Ma, Mater. Lett.68, 336(2012)
[15] X. Zhang, P. Yu, D. Zhang,H. Zhang, X. Sun, Y.Ma, Mater. Lett. **92**401(2013)
[16] J.L. Liu, L.Z. Fan, X.Qu, Electrochim. Acta. 66, 302(2012)
[17] R. Jiang, T. Huang, J. Liu, J. Zhuang, A.Yu, Electrochim. Acta.54, 3047(2009)
[18]C.K. Lin, K.H. Chuang, C.Y. Lin, C.Y. Tsay, C.Y.Chen, Surf. Coat. Technol.202,1272 (2007)

[19]D.P. Dubal, D.S. Dhawale, R.R. Salunkhe, V.J. Fulari, C.D.Lokhande, J. Alloy. Compd. 497,166(2010)
[20] C. Xu, B. Li, H. Du, F. Kang, and Y.Zeng, J of Power Sources.180,664 (2008)
[21] A. Zolfaghari,F. Ataherian, M. Ghaemi, andA.Gholami, Electrochimica Acta. 52,2806(2007)
[22]T. Nguyen, M.J. Carmezim,M. Boudard, M.Montemor, J. Hydrog. Energy. 40,16355(2015)
[23]A. Yuan, X. Wang, Y. Wang, J.Hu, Electrochim. Acta. 54,1021(2009)
[24] D.P. Dubal, D.S. Dhawale, R.R. Salunkhe, S.M. Pawar, C.D. Lokhande,Appl Surf Sci.256,4411(2010)
[25] T. Yousefi, A.N. Golikand, M.H. Mashhadizadeh, M. Aghazadeh,Curr. Appl. Phys. 12, 544(2012)
[26] M. Kim, Y. Hwang, J. Kim,J. Power Sources. 239, 225(2013)
[27] X. Dai, M. Zhang, J. Li, D.Yang, RSC Adv.10, 15860(2020)
[28]P.M. Kharade, S.G. Chavan, D.J. Salunkhe, P.B. Joshi, S.M. Mane, S.B. Kulkarni, J. Mater. Sci. Mater. Electron. 52, 37(2014)
[29] M. Zhang, X. Dai, C. Zhang, Y. Fuan, D. Yang, J.Li, Mater.13, 181(2020)
[30] P.D. More, P.R. Jadhav, S.M. Ingole,Y.H. Navale,V.B.Patil, J Mater Sci: Mater Electron. 28,707(2017)
[31] A.A. Shaikh, M.R. Waikar, R.G.Sonkawade, Synth. Met. 247, 1(2019)
[32] D.P. Dubal, D.S. Dhawale, R.R. Salunkhe, C.D. Lokhande,J. Electrochem. Soc. 157,A812 (2010)
[33] G.S. Gund, D.P. Dubal, B.H. Patil, S.S. Shinde, C.D.Lokhande, Electrochim. Acta. 92,205 (2013)

International e-Conference on Recent Trends in Nano-Materials and Its Applications
In Association with International Journal of Scientific Research in Science and Technology
Volume 9 | Issue 11 | Print ISSN: 2395-6011 | Online ISSN: 2395-602X (www.ijsrst.com)

# Investigation The Temperature and Volume Fraction Effects on The Thermal and Rheological Properties of The $TiO_2$ Nanofluid

**N B Girhe[1], S N Botewad[2*], P P Pawar[2], A B Kadam[2]**
[1]Department of Physics, Jawahar Science, Commerce and Arts College, Andoor, Tuljapur 413603, Maharashtra, India
[2]Department of Physics, Dr. Babasaheb Ambedkar Marathwada University, Aurangabad 431004, Maharashtra, India

## ABSTRACT

The present investigation has been reported the preparation of water-based TiO2 nanofluid using a two-step method. The temperature and volume fraction dependent thermal conductivity and viscosity TiO2 was studied. The different volume fraction of TiO2 (0.1,0.2,0.3,0.4 and 0.5) were used dispersed in water using harsh ultrasonic treatment and tested the thermal conductivities for temperature range of 20–50 °C. The experimental results reveal that increase in temperature and volume fraction increases the thermal conductivity of nanofluid. The viscosity of the nanofluid with same concentration of TiO2 was measured and shows the decrease viscosity by increasing temperature whereas increases when increase the volume concentration. Thus, the experimental results are much more useful for the practical application of nanofluids in thermal management.

**Keywords:** Nanofluid; Nanoparticles; Thermal Conductivity; Viscosity;

## I. INTRODUCTION

Thermal management becomes the very critical task in various industries for getting the efficient productivity. Worldwide various conventional fluids were used for the thermal management such as water, oil, ethylene glycol etc. But unfortunately, these fluids do not achieve the desired thermal properties for practical application. To improve the thermal conductivities of these conventional fluids firstly in 1873 Maxwell proposed the single-phase fluids with the addition of solid particles [1]. The idea of Maxwell worked and it improves the thermal properties of the conventional fluids but it has the drawbacks such as sedimentation, clogging and erosion during the flow. After this inventive research idea and experimental results in 1995, Choi introduced the idea of nanofluids with his own experimental results. The nanofluid which solely overcomes the sedimentation, clogging and erosion problems [2].

An emerging nanotechnology provides the superior physical, thermal, optoelectronics properties of the material in nanosized dimension. The very new trending application of nanotechnology is the nanofluid research. Nanofluid is an engineering fluid in which nanometre sized solid particles homogeneously dispersed in base fluid such as water, engine oil, propylene glycol, ethylene glycol, etc [3]. Recently various types of nanomaterials were found to be used for the preparation of nanofluid such as metal, metal oxides, carbon materials etc. Nowadays metal oxide nanoparticles (TiO2, SiO2, Fe2O3, Fe3O4, Al2O3, BaTiO3, CuO, etc.) extensively employed for the preparation of nanofluid [4]. The preference for metal oxide nanoparticles is due to the superior physicochemical, optoelectronics, thermal properties, and ease of preparation with tuned properties. The potential of nanofluids to enhances the thermal conductivity and rheological behaviour of base fluid it applicable in heat transfer, including fuel cells, cooling of microelectronic equipment, pharmaceutical processes and hybrid engines etc [5,6].

Worldwide different research groups have been reported the thermal conductivity and viscosity of the nanofluids using the different types of nanoparticles with different volume fraction in the base fluid. M.Kh. Abdolbaqi et. al studied the thermal conductivity and viscosity of BioGlycol/water based TiO2 nanofluids and experimental results shows that enhancement of thermal conductivity depends on volume concentration, temperature and thermal conductivity of base fluid [7]. M.H. Ahmadi et.al investigate the thermal performance of TiO2 nanofluid using four different neural networks [8]. D. Cabaleiro et.al reported the ethylene and propylene glycol-based $TiO_2$ (anatase and rutile) nanofluids. The experimental results shows that thermal conductivity increases 15.4%. and enhancements are higher for propylene than ethylene glycol-based nanofluids [9]. W.H. Azmi et.al investigate the heat transfer performance of $TiO_2$ nanofluids in water-EG mixture at different operating temperatures. On the basis of experimental results concluded that maximum enhancement of thermal conductivity was 15.4% at 1.5% volume concentration and temperature of $60^0$ C. and relative viscosities fluctuate at a range of 4.6 to 33.3% with variation of temperature [10].

## II. EXPERIMENTAL

### 2.1 Materials and Characterization

In present investigation $TiO_2$ (Rutile) nano particles with particles size 20 nm procured from the Sisco Research Laboratory Mumbai, India. KD2 Pro thermal analyser (Decagan Devices Inc., USA) was use to study the thermal conductivity and before measurements the device prob was calibrated with standard fluid. The viscosity of all nanofluid were measured by means of an AR-G2 rheometer (TA Instruments, USA) at different temperatures.

### 2.2 Nanofluid Preparation

Nanofluids reported in the present investigation were prepared via two-step method. TiO2 nanoparticles of volume fraction (0.1, 0.2, 0.3, 0.4, and 0.5 Wt.%) were used for the preparation of nanofluid. The above-mentioned proportion of $TiO_2$ nanoparticles was dispersed in the base fluid double distilled water (DDW) separately and stirred for 2 hours forcefully using magnetic stirrer. Then the stable dispersion was attained by ultrasonic probe via ultrasonication for 6 h.

## III. RESULTS AND DISCUSSION

### 3.1 Thermal conductivity

The thermal conductivity of prepared water based $TiO_2$–nanofluids concentrations of (0.1, 0.2, 0.3 and 0.4) wt. % were measured at temperatures of 300 K-350 K in 15 k interval. Fig. 1 shows the thermal conductivity of prepared nanofluid for different volume concentrations and fig. 2 shows for different temperatures. It is observed that by increasing both parameters volume concentrations and temperatures, thermal conductivity is enhanced of all the studied samples. Increment of the nanoparticles loading in the base fluid reduces the interparticle distances that improves heat conduction and the outcome is enriched thermal conductivity. The basic phenomenon of the increment in the thermal conductivity is propagation of lattice vibration between electrons and phonons. The thermal conductivity significantly increases by increasing temperatures due to the Brownian motion which provide the direct solid-solid transport between the incorporated particles.

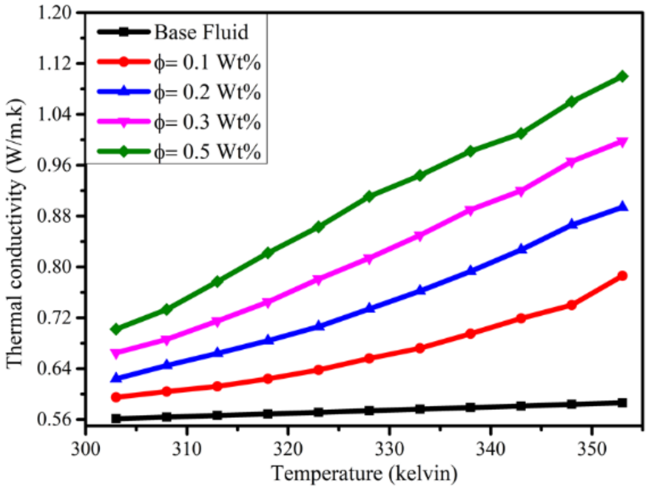

Figure 1. Thermal conductivity for various volume fraction at different temperature

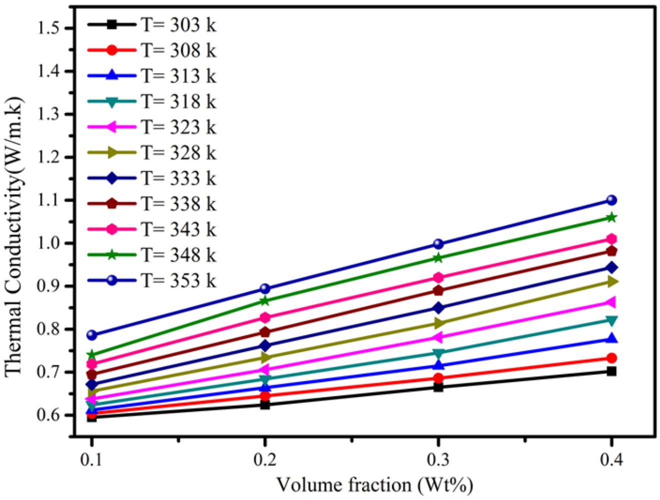

Figure 2. Thermal conductivity for different temperatures of various concentration

### 3.2 Viscosity

Rheological behaviors of all prepared nanofluid samples viscosity were examined at different temperature points of 300 K-360 K at equal interval for each volume concentrations. Fig. 3 shows the dependency of viscosity on the volume concentration and temperature of $TiO_2$ nanofluid. The considerable effects were observed for both parameters, temperature as well as volume concentrations. As concerned to the volume concentration viscosity of all the nanofluid samples observed to be increased. The reason behind the increasing viscosity may be due to the formation of agglomeration of nanoparticles in suspension. The temperature effect slightly reduces the viscosity due to the feeble intermolecular interaction and adhesion forces between molecules which is further attributed to Brownian motion, thermal movement of molecules and their average speed.

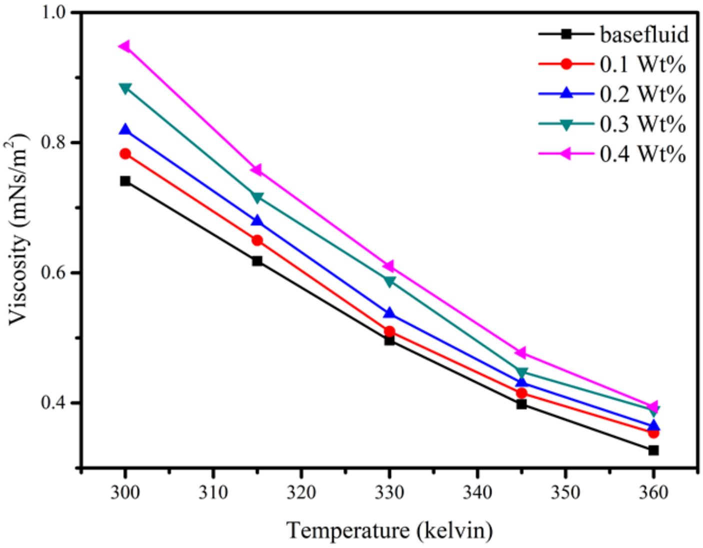

Figure 3. Viscosity of $TiO_2$ nanofluid at different temperature

## IV. CONCLUSION

In short, present investigation successfully encloses the preparation and analysis of the thermal as well as rheological properties of $TiO_2$ nanofluids. The investigational findings reveal the considerable enhanced thermal conductivity of nanofluids with increased temperature and volume concentration. The viscosity of the nanofluid increased with volume concentration whereas decreased with increased temperature. Thus, the present investigation exhibits the applicability of the ternary $TiO_2$ nanofluid for the various application wherever the necessity of cooling.

## V. REFERENCES

[1]. Vanaki, S. M., Ganesan, P., & Mohammed, H. A. (2016). Numerical study of convective heat transfer of nanofluids: a review. Renewable and Sustainable Energy Reviews, 54, 1212-1239.

[2]. Das, S. K., & Stephen, U. S. (2009). A review of heat transfer in nanofluids. Advances in Heat transfer, 41, 81-197.
[3]. Ali, H. M., Babar, H., Shah, T. R., Sajid, M. U., Qasim, M. A., & Javed, S. (2018). Preparation techniques of TiO2 nanofluids and challenges: a review. Applied Sciences, 8(4), 587.
[4]. Sidik, N. A. C., Mohammed, H. A., Alawi, O. A., & Samion, S. (2014). A review on preparation methods and challenges of nanofluids. International Communications in Heat and Mass Transfer, 54, 115-125.
[5]. Puliti, G., Paolucci, S., & Sen, M. (2011). Nanofluids and their properties. Applied Mechanics Reviews, 64(3).
[6]. Suganthi, K. S., & Rajan, K. S. (2017). Metal oxide nanofluids: Review of formulation, thermo-physical properties, mechanisms, and heat transfer performance. Renewable and Sustainable Energy Reviews, 76, 226-255.
[7]. Abdolbaqi, M. K., Sidik, N. A. C., Aziz, A., Mamat, R., Azmi, W. H., Yazid, M. N. A. W. M., & Najafi, G. (2016). An experimental determination of thermal conductivity and viscosity of BioGlycol/water based TiO2 nanofluids. International Communications in Heat and Mass Transfer, 77, 22-32.
[8]. Ahmadi, M. H., Baghban, A., Sadeghzadeh, M., Hadipoor, M., & Ghazvini, M. (2020). Evolving connectionist approaches to compute thermal conductivity of TiO2/water nanofluid. Physica A: Statistical Mechanics and its Applications, 540, 122489.
[9]. Cabaleiro, D., Nimo, J., Pastoriza-Gallego, M. J., Piñeiro, M. M., Legido, J. L., & Lugo, L. (2015). Thermal conductivity of dry anatase and rutile nano-powders and ethylene and propylene glycol-based TiO2 nanofluids. The Journal of Chemical Thermodynamics, 83, 67-76.
[10]. Azmi, W. H., Hamid, K. A., Mamat, R., Sharma, K. V., & Mohamad, M. S. (2016). Effects of working temperature on thermo-physical properties and forced convection heat transfer of TiO2 nanofluids in water–Ethylene glycol mixture. Applied Thermal Engineering, 106, 1190-1199.

International e-Conference on Recent Trends in Nano-Materials and Its Applications
In Association with International Journal of Scientific Research in Science and Technology
Volume 9 | Issue 11 | Print ISSN: 2395-6011 | Online ISSN: 2395-602X (www.ijsrst.com)

# Variation of Magnetic Susceptibility of Nanoparticle Sized Copper Cobalt Ferrites

**S. S. Karande[1], M. S. Kavale[1], B. R. Karche[2]**
[1]Department of Physics, Sangameshwar College, Solapur, Maharashtra, India
[2]Material Science and Thin Film Laboratory, Shankarrao Mohite Mahavidyalaya, Akluj, Dist. Solapur, Maharashtra, India

## ABSTRACT

The polycrystalline aluminium substituted nano-particle sized copper cobalt ferrite samples CuxCo1-xFe2-2yAl2yO4 (where x= 0.0, 0.2, 0.4, 0.6, 0.8, 1.0; y= 0.05, 0.15 and 0.25) have been prepared by standard ceramic technique. Phase formation is investigated using X-ray diffraction, Infrared absorption technique and Scanning electron microscope technique. The lattice constants of the all samples are evaluated from x-ray diffraction data. The Magnetic susceptibility decreases with aluminium and copper content.

**Keywords:** Polycrystalline, nanoparticle size, standard ceramic technique and Inverse cubic spinel, Magnetic susceptibility

## I. INTRODUCTION

In a way, every material utilized today is a composite. Composite materials are a physical mixture of two or more compatible micro or macro constituent particles which differ in form and chemical composition and are essentially insoluble in each other. Composite materials are best suited for scientific applications which could not be achieved by any one component acting on its own. Ferrite / ferroelectric composites are termed as magneto electric (ME) composites due to the coupling between the electric and magnetic fields in the materials. The conversion of magnetic to electric fields in such ME composite originates from the elastic interaction between ferrite and ferroelectric subsystems [1]. In the presence of the magnetic field, the magnetostriction in the ferrite phase gives rise to mechanical stresses that are transferred to the ferroelectric phase, resulting in electric polarization of the ferroelectric phase owing to its magneto electric effect. ME materials find applications as smart materials in actuators, sensors, magnetic probes, phase inverters, rectifiers, modulators, and transducers in solid state microelectronics and microwave devices [2,3].

Spinel ferrite nanoparticles are being intensively investigated in recent years because of their remarkable electrical and magnetic properties and wide practical applications in information storage system, ferro-fluid technology, magnetiocaloric refrigeration and medical diagnosis [4]. Among the spinels, mixed Zn ferrites and especially Ni–Zn ferrites are widely used in applications like transformer cores, chokes, coils, noise filters recording heads etc. [5]. While Ni–Zn ferrite posses higher resistivity and saturation magnetization, cobalt ferrite possess high cubic magneto crystalline anisotropy and hence high coercivity. The high coercivity is driven by large anisotropy of the cobalt ions due to its important spin orbit coupling. It is ferromagnetic with a Curie temperature ($T_c$) around 520°C, [6] and shows a relatively large magnetic hysteresis which distinguishes it from rest of the spinels. The synthesis of ultra fine magnetic particles has been extensively investigated in recent years because of their potential applications in high density magnetic recording and magnetic fluids [7]. Among the current methods for synthesis of mixed ferrite the combustion reaction method stands out as an alternative and highly promising method for the synthesis of these ferrites [8]. Magnetic properties measured at room temperature by vibrating sample magnetometer (VSM) reveal an increase in saturation magnetization with increase in cobalt concentration [9].

## II. EXPERIMENTAL

**Materials:**

High purity starting materials are used as Cobalt Oxide (CoO):- 74.9326 gm, Copper Oxide (CuO):- 74.5454 gm, Ferric oxide($Fe_2O_3$):- 159.6922 gm, Aluminum Oxide ($Al_2O_3$):- 101.9612 gm

**Preparation of ferrite**:

Nano crystalline powder samples of $Cu_xCo_{1-x}Fe_{2-2y}Al_{2y}O_4$ (where x= 0.0, 0.2, 0.4, 0.6, 0.8, 1.0; y = 0.05, 0.15 and 0.25) were prepared by the standard ceramic technique. Starting materials CuO, CoO, $Fe_2O_3$ and $Al_2O_3$ of AR grade obtained from Sigma – Aldrich, India were used. These samples were heated at ramping rate of 80 $^0$C hr $^{-1}$ at 1000$^0$C for 48 hours. XRD and IR analysis revealed the cubic spinel structure of the synthesized samples and functional groups in the samples respectively. The absence of any extra line confirms the formation of single phase ferrite. The average particle size 'D' was determined from line broadening (311) reflection using the Debye Scherer formula discussed elsewhere [10]. Calculations of lattice constant, physical density, X-ray density, porosity, site radii and ionic bond lengths on both sites were calculated by using formulae discussed elsewhere [11] and graphically shown in fig.4. Infrared absorption spectra of powdered samples were recorded in the range 350-800 cm$^{-1}$ using Perkin-Elmer FTIR spectrum and spectrometer by KBr pellet technique and presented in (fig.2). The scanning electron microscopes are shown in fig.3

## III. RESULTS AND DISCUSSION

The X-ray diffraction patterns of the samples are presented in (fig.1). Powder X-ray diffractometer of the ferrite samples reveals the single phase spinel structure, as well defined reflection is observed without any ambiguity. The diffraction peaks are corresponding to (200), (311), (400), (422), (333/511), (440) and (533) planes. The lattice constants ‘a’ and ‘c’ for all prepared samples are calculated by using prominent (311) XRD peak. The calculated and observed values of inter planer distance (d) are found in good agreement with each other for all reflections. The physical density (dB), x-ray density (dx), and porosity (p), are calculated from the formulae given by Gadkari et.al [12].

From the calculations of lattice constants ‘a’ and ‘c’ for all the prepared ferrites it is observed that c >a and tetragonality ratio (c/a) is found in the range of 1.03 to 1.07. This result is in good agreement with previous report [13-14].In this present report tetragonality ratio for copper ferrite is 1.06. It means 70% copper resides on B site and it exhibits prorate type distortions in the crystal lattice. The previous report [15] well supports the present results reported this communication. Both $Fe^{3+}$ and $Cu^{2+}$ are John-Teller ion which produces prolate type distortions on (B) site and hence c >a and (c/a) = 1.06. Therefore copper ferrite exhibits tetragonal spinel structure in host crystal lattice of cobalt ferrite. In addition of copper content in tetragonality ratio is found increasing but due to addition of aluminium tetragonality ratio deceases. It means that $Al^{3+}$ and copper suppress the tetragonal prolate type.

The crystallite sizes (t) of all the prepared samples were computed by Scherer rule utilizing the peak width at one-half intensity of the maximum intensity peak (311).

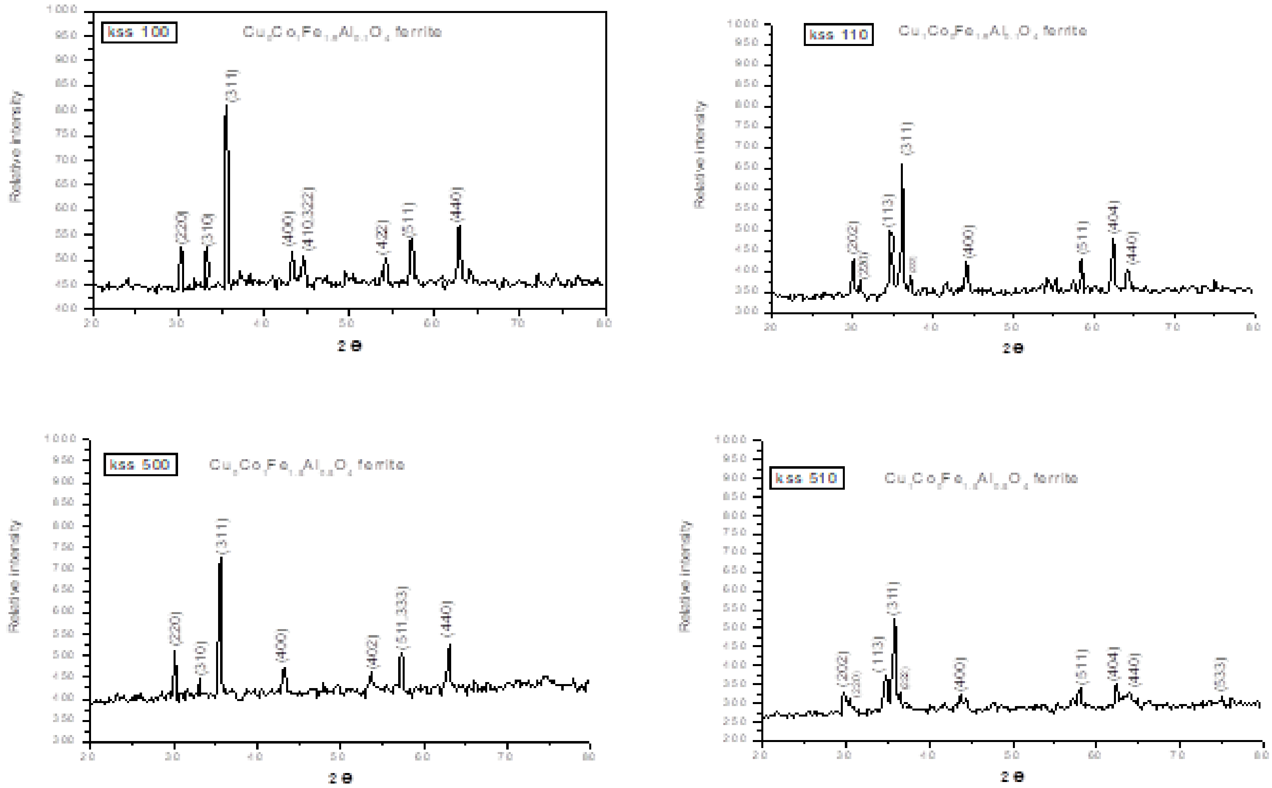

**Fig: 1 XRD patterns of system $Cu_xCo_{1-x}Fe_{2-2y}Al_{2y}O_4$**

The Al (y = 0.05-0.25) doped copper cobalt ferrite samples show a higher grain growth and the crystallite size (t) lies in the extent of 52.53-94.4 nm. The mean particle size calculated from diffractograms is in the range of 50 to 100 nm. That suggest the particles in the ferrites samples are fine and there is continuous grain growth in all compositions. It gives the confirmation of suitable microstructure formation in all compositions.

The width of the reflection peak (311) for all the compositions is approximately the same due to the nearly equal particle size.

The infrared absorption spectra are showing two distinct absorption bands $\nu_1$ due to tetrahedral (A) site interstitial voids near 600 cm$^{-1}$ and other $\nu_2$ due to octahedral (B) site interstitials voids near 400 cm$^{-1}$. Our results in this present communication are well supported by previous reports [16, 17].

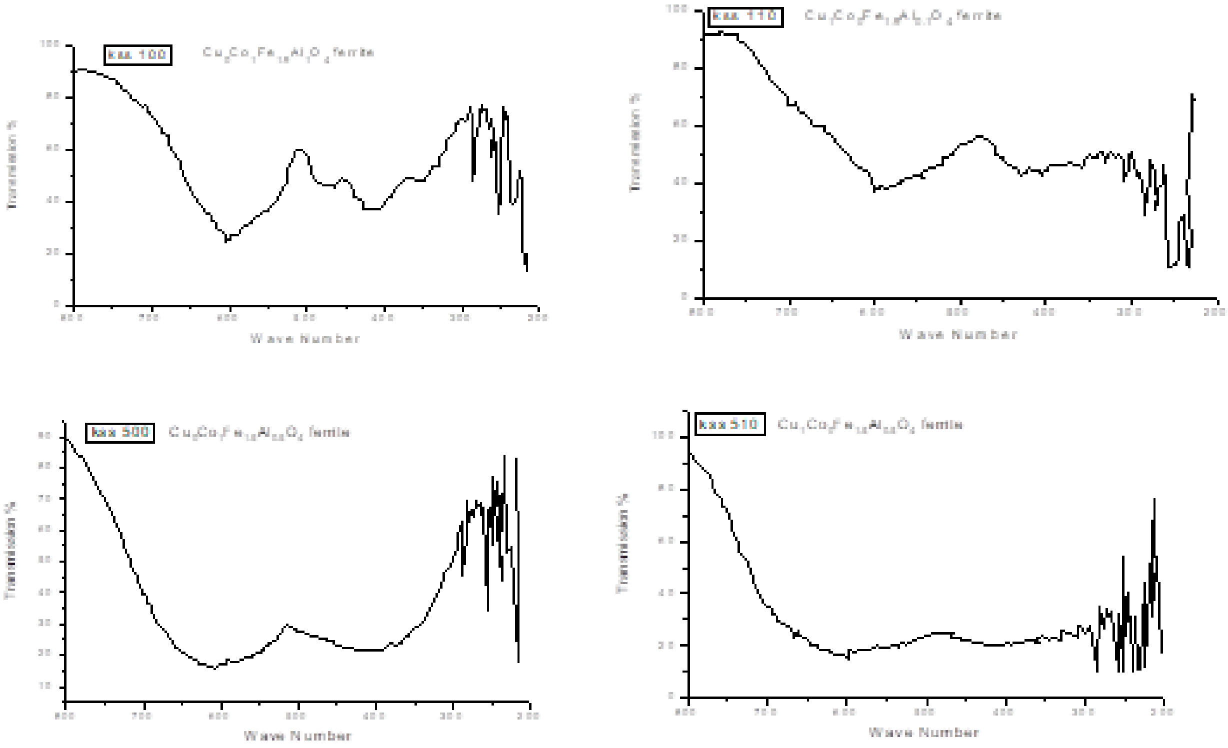

**Figure 2: Absorption spectra for system $Cu_xCo_{1-x}Fe_{2-2y}Al_{2y}O_4$**

The close inspection of all micrographs revealed that there is continuous grain growth with well – defined grain boundaries formed. The present system shows multi domain behavior. No exaggerated grain growth is observed in any composition. The average grain size is found to decrease with increase in Al content in copper cobalt ferrite. However in the present system the grain growth shows generally a decreasing trend with aluminum content, which is rather expected because of multi-domain behavior of these compositions in copper cobalt ferrite. Grain growth is almost accompanied with grain size, which is increasing with copper and aluminum content. So it appears that copper and aluminum content favors the grain growth. The scanning electron micrographs shown below

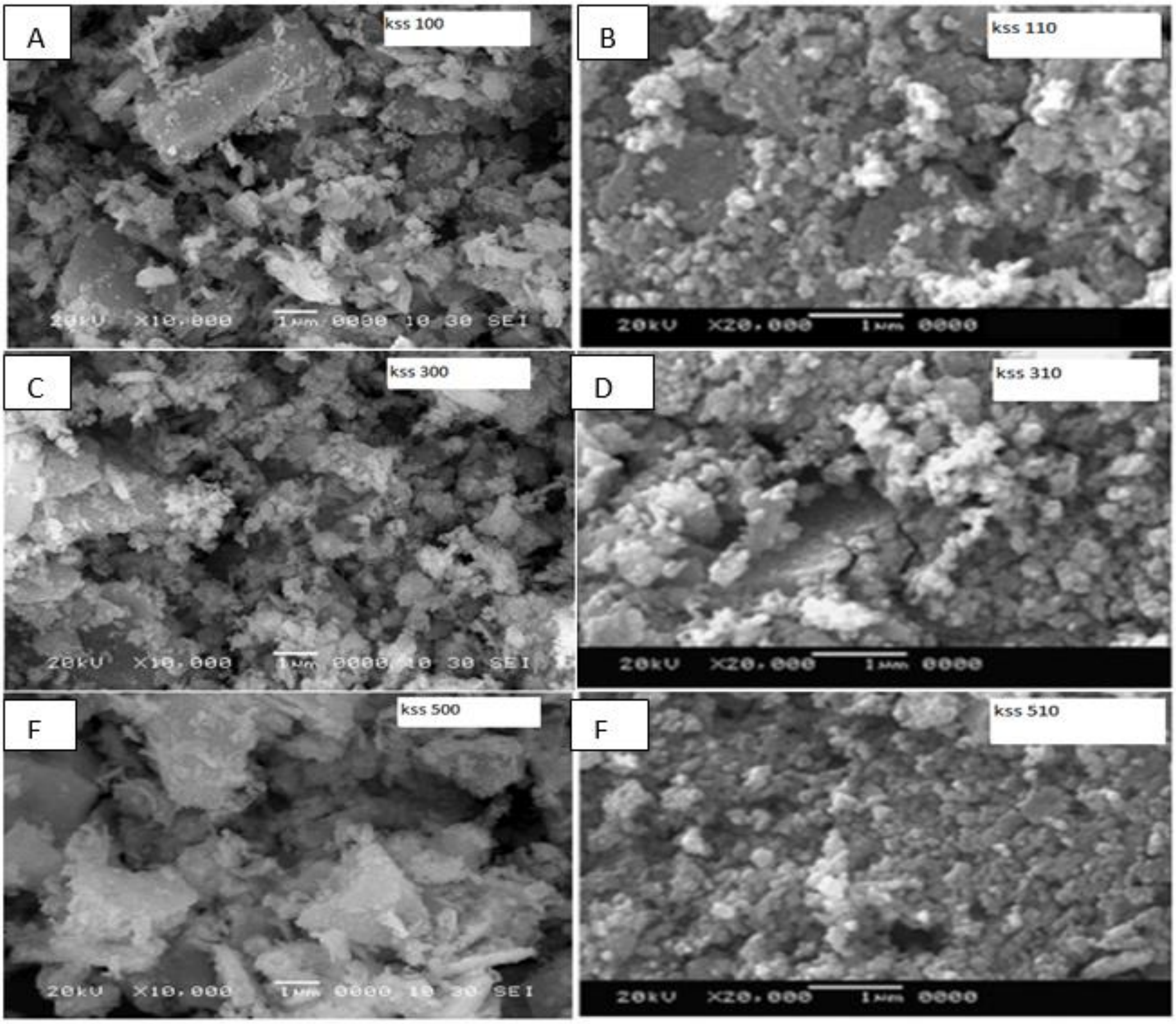

**Fig: 3 (A) to (F) scanning electron microscopes of $Cu_xCo_{1-x}Fe_{2-2y}Al_{2y}O_4$ :**
**(A) KSS 100-$Cu_0Co_1Fe_{1.9}Al_{0.1}O_4$, (B) KSS 110- $Cu_1Co_0Fe_{1.9}Al_{0.1}O_4$,**
**(C) KSS 300- $Cu_0Co_1Fe_{1.7}Al_{0.3}O_4$, (D) KSS 310- $Cu_1Co_0Fe_{1.7}Al_{0.3}O_4$,**
**(E) KSS 500- $Cu_0Co_1Fe_{1.5}Al_{0.5}O_4$ & (F) KSS 510- $Cu_1Co_0Fe_{1.5}Al_{0.5}O_4$**

The susceptibility is measured at room temperature [Fig. 2(a)] then susceptibility is found increasing up to 20 % of copper content and thereafter decreases. The susceptibility is measured at various temperatures [Fig. 2(b)], the compositions shows gradual decrease in normalized susceptibility with temperature which suggest that they exhibit super paramagnetic (SP) structure having fine particles. The susceptibility is decreases and curie temperature also shifts towards minimum value as copper as well as aluminum content increases.

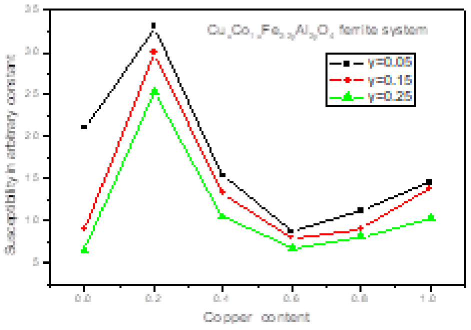

Fig. 4(a)

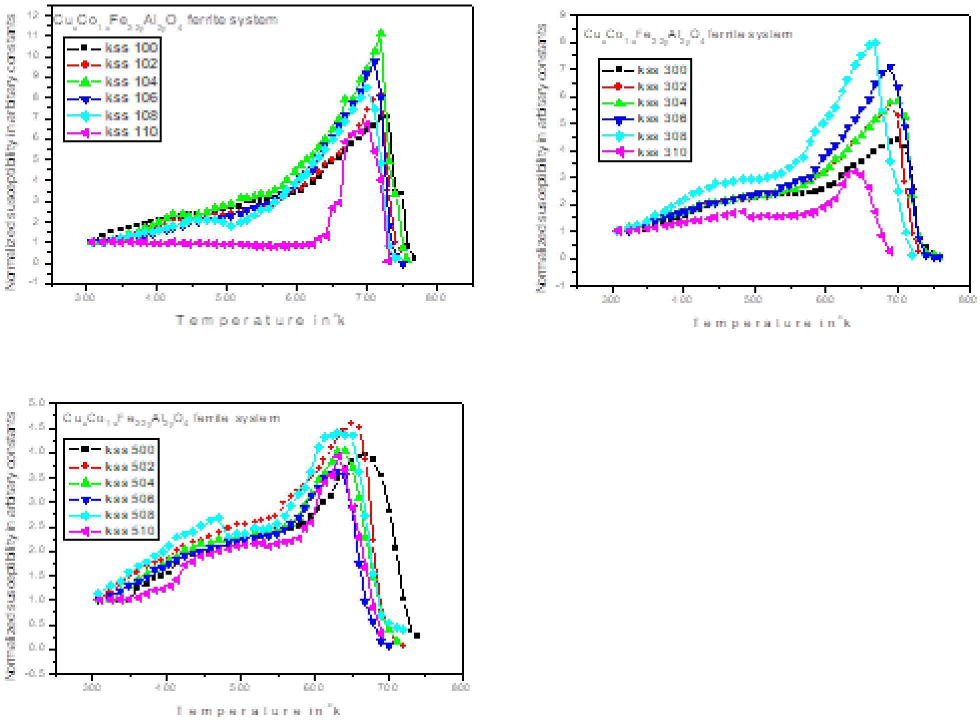

Fig. 4(b)

**Fig 4: Variation of A. C. susceptibility with copper and aluminum content at room temperature and various temperature for $Cu_xCo_{1-x}Fe_{2-2y}Al_{2y}O_4$ ferrite system**

## IV. CONCLUSIONS

Copper cobalt ferrite is partially inverse spinel ferrite. Addition of $Al^{3+}$ ions replaces $Fe^{3+}$ on (B) site resulting in increase of lattice constant a, decrease in ionic radii($R_A$) and bond length(O-A). The lattice constant obtained from XRD data shows increases. The A. C. susceptibility goes on decreasing with copper and aluminum content.

## V. REFERENCES

[1]. R. S. Devan, S. A. Lokare, S. S. Chougule, D. R. Patil, Y. D. Kolekar, andB. K. Chougule, J. Phys. Chem. Solids 67, 1524 (2006).

[2]. K. Zhao, K. Chen, Y. R. Dai, J. G. Wan, and J. S. Zhu, Appl. Phys. Lett. 87, 162901 (2005).

[3]. S. R. Kulkarni, C. M. Kanamadi, and B. K. Chougule, Mater. Res. Bull. 40, 2064 (2005).

[4]. Zhao L, Yang H, Yu L, Cui Y, Zhao X, Zou B, Feng SJ. MagnMagn Mater2006;301:445–51.

[5]. Rath C, Sahu KK, Anand S, Date SK, Mishra NC, Das RP. J MagnMagn Mater 1999;202:77–84.

[6]. Rajendran M, Pullar RC, Bhattacharya AK, Das D, Chintalapudi SN, Majumdar CK. J MagnMagn Mater 2001;232:71–83.

[7]. Ozaki M. Mater Res Bull 1989;12:35–43.

[8]. Costa ACM, Tortella E, Morelli MR, Kaufman M, Kiminami RHGA. J Mater Sci2002;37:3569–72.

[9]. M.M. Mallapur, B.K. Chougule; Materials Letters; Vol. 64 (2010); P. 231–234.

[10].H. P. Klug, L. E. Alexander, X-ray diffraction procedure for polycrystalline and amorphous materials, Willey N.Y, 1997, 637.

[11].A. B. Gadkari, T. J. Shinde, P. N. Vasambekar, J. Mater Sci: Mater Electron 21 2010, 96 , 103.

[12].Prince E., Treuting R.G; Acta Crystallographica, 1956, 9, 1025.

[13].Sagal K., Tabellen F. Rontegenstrukturanalyse, Springer, Berlin, 1958.

[14].Borisenko A., Toropov N. A; Z. Prikl Chem, 1950, 23, 1165.

[15].Goodenough J.B and Loeb A. L ,Phys. Rev., 1955, 98, 391.

[16].Waldron R.D, Phy. Rev, 1955, 99(6), 1727.

[17].K. V. S. Badarinath, Phys. Stat. Solidi (a) 1985, 91, 19-23.

International e-Conference on Recent Trends in Nano-Materials and Its Applications
In Association with International Journal of Scientific Research in Science and Technology
Volume 9 | Issue 11 | Print ISSN: 2395-6011 | Online ISSN: 2395-602X (www.ijsrst.com)

# DC Resistivity of La3+ Substituted Mg-Zn Ferrite Nanoparticles by Co-Precipitation Method

**R.A. Bugad[1]*, B.G. Pawar[1], B.B. Navale[2], P.G. Pawar[3]**
[1]Department of Science, Sangola Mahavidyalaya, Sangola, Dist. Solapur 413307, Maharashtra, India
[2]Department of Science, Vidnyan Mahavidyalaya, Sangola, Dist. Solapur 413307, Maharashtra, India
[3]Department of Science, Shivaji Polytechnic College, Sangola, Dist. Solapur 413307, Maharashtra, India

## ABSTRACT

Lanthanum (La) substituted magnesium zinc ferrite nanoparticles with general formula Mg0.6Zn0.4La2yFe2-2yO4 (where y = 0.00, 0.05, 0.10, 0.15, 0.20 and 0.25) have been synthesized by co-precipitation method. The XRD analysis was carried out to confirm the single –phase cubic structure of La3+ substituted Mg-Zn ferrite. The nature of DC resistivity of ferrite was studied with substitution of La3+ content. The effects of La3+ substitution in Mg-Zn ferrite on structural and electric properties were studied.

**Keywords:** Lanthanum, Mg-Zn ferrites, Co-precipitation, DC Resistivity,

## I. INTRODUCTION

Ferrites are usually non-conductive ferrimagnetic ceramic material. Most of the ferrites have a spinel structure [1]. The general formula of a spinel can be written as $AB_2O_4$. Nano-particles of mixed spinel ferrites have been the subject of current interest because of their interesting electric, optical and magnetic properties, which are considerably different from that of their bulk ferrites [2]. The ferrites are also widely used in high frequency cores, antennas, high frequency transformers, deflecting coil, motor generator and microwave devices such as modulators, phase shifter and circulators etc.[3]. The coercive force is related with saturation magnetization, anisotropy, internal stresses and porosity. The ferrites having low coercive force (HC) is known as Soft ferrites [4]. Generally, soft ferrite shows high electrical resistivity, superior magnetic and structural properties and hence they have low eddy current losses at high frequency [5]. Demand for electronic and computer components with high density and light weight performance is greatly increasing, which step up the demand for soft ferrites with high performance and thus contributes to the development of soft magnetic ferrites on the direction of higher frequency and lower power consumption [6].

## II. EXPERIMENTAL

### 2.1. Synthesis of $La^{3+}$ substituted Mg-Zn ferrite

The $Mg_{0.6}Zn_{0.4}La_{2y}Fe_{2-2y}O_4$ (where y= 0.00, 0.05, 0.10, 0.15, 0.20 & 0.25) have been prepared by the oxalate co-precipitation method as per reported in earlier literature [7]. The high purity AR grade starting materials $MgSO_4.7H_2O$, $ZnSO_4.7H_2O$, $LaSO_4.7H_2O$ and $Fe_2SO_4.7H_2O$ were used for preparation of samples. These chemicals were weighted in desired stoichiometric proportion and dissolved in distilled water. The pH of the solution was maintained at 4.8 by drop wise addition of concentrated $H_2SO_4$. The resulting solution was heated at 80 $^0$C for 1 h in order to complete the ionization of metal sulfates. The precipitating regent was prepared in distilled water by adding required proportion of AR grade ammonium oxalate. Ammonium oxalate was taken in burette and was added drop by drop until the precipitation was formed. The co-precipitate product was dried and calcined at 450 $^0$C for 5h in air. The calcined powders were milled in an agate mortar with AR grade acetone as a base. The powders were pre-sintered at 700 $^0$C for 5h.The pre-sintered powders were pressed under hydraulic pressure of 5 tones /cm$^3$ to form pellet using polyvinyl alcohol as binder. Then pellets were finally sintered at 900 $^0$C for 12h.

### 2.2. Characterization Techniques

XRD patterns of lanthanum substituted magnesium zinc ferrites sintered at 900$^0$C for 12h were recorded by Philips X-Ray Diffractometer model PW 1710 using Cu Ka radiation ( $\lambda$ = 1.5405 A$^0$ ). Two probe method was used for measurement of the dc electrical resistivity of ferrite in the temperature range 25$^0$C to 575$^0$C. The resistivity was obtained by using formula $\rho = \frac{\pi r^2}{t} \times \frac{V}{I} = \frac{\pi r^2 R}{t}$ , Where, t is thickness and r is radius of the pellet in cm.

## III. RESULTS AND DISCUSSIONS

### 3.1. XRD studies

The XRD patterns of $Mg_{0.6}Zn_{0.4}La_{2y}Fe_{2-2y}O_4$ (where y = 0.00, 0.05, 0.10, 0.15, 0.20, 0.25) ferrite system sintered at temperature 900$^0$C for 12h are shown in Fig. 1. The XRD patterns reveals the well resolved, sharp and intense peaks corresponding to planes (220), (311), (222), (400), (422), (511), (440), (620) and (533). The peaks obtained in the diffractogram closely match the data in the JCPDS file card number (04-002-5442). The XRD peak pattern corresponds to all allowed planes, which hint outs single phase cubic structure with the traces of secondary phase. Moreover, the peak at $2\theta$= 32.10° corresponds to plane (121) which is attributed to secondary phase for $LaFeO_3$ indexed as per ICDD file No. 01-74-9045. With increase in La content, intensity of characteristics peak (311) for $Fe_2O_4$ gradually decreases, while intensity of peak (121) of $LaFeO_3$ increases. It implies that the substituted $La^{3+}$ ion has a solubility limit in the spinel lattice.

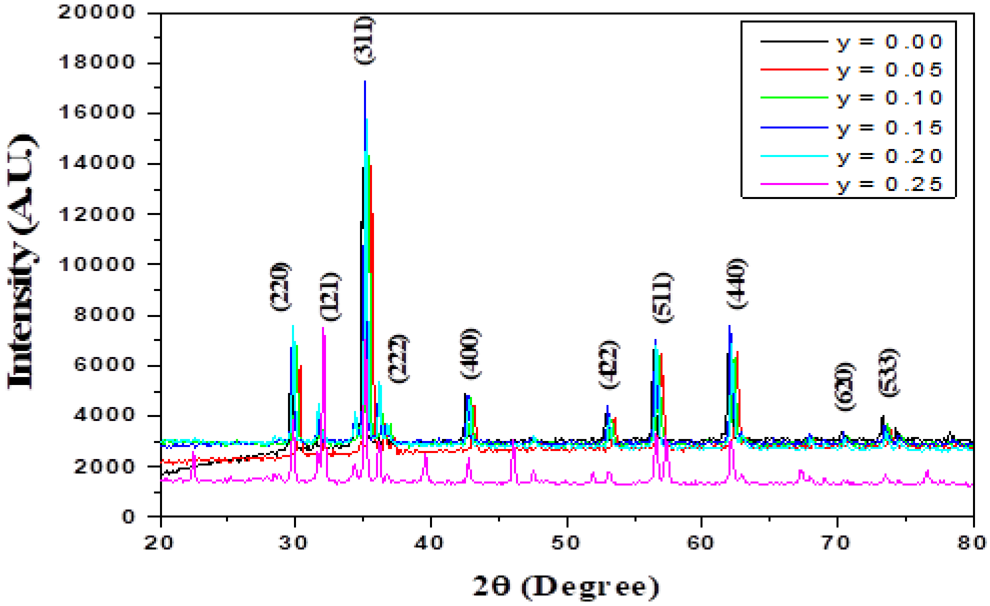

**Fig.1** : XRD patterns of $Mg_{0.6}Zn_{0.4}La_{2y}Fe_{2-2y}O_4$ ferrite system

The degree of substitution of $Fe^{3+}$by $La^{3+}$ ion is limited in the spinel lattice due to larger ionic radii of $La^{3+}$ ions compared to $Fe^{3+}$ions. There is always some $La^{3+}$ ions do not enter into spinel lattice. These $La^{3+}$ ions react with $Fe^{3+}$ ions and form second phase $LaFeO_3$ usually locating at the grain boundaries. Similar observation have been reported in lanthanum substituted nickel [8], Cadmium [9] and Ni-Zi ferrites [10, 11].

### 3.2. DC Resistivity study

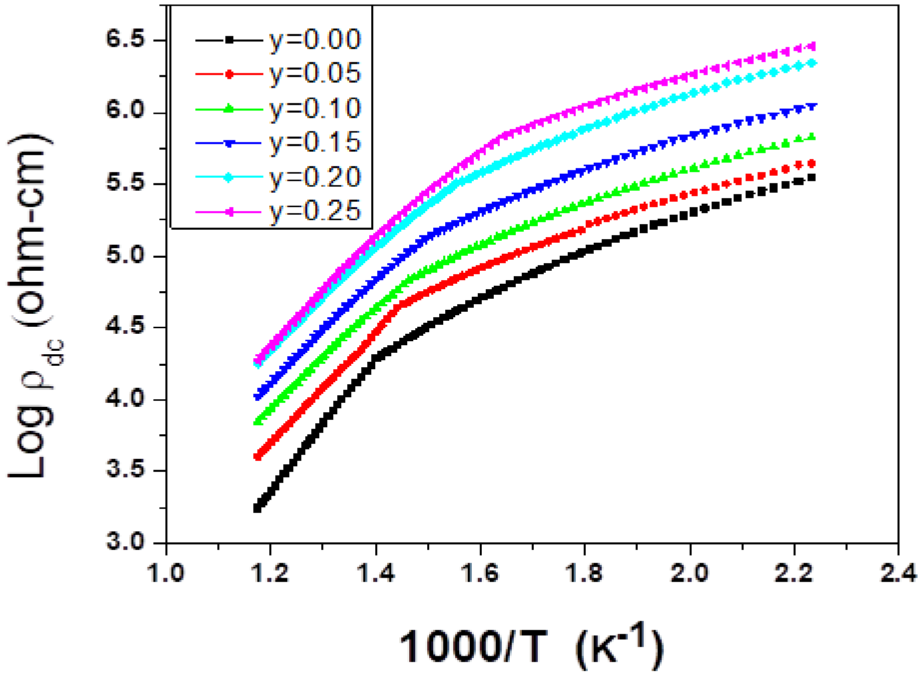

**Fig.2:** Variation of dc resistivity with inverse temperature for $Mg_{0.6}Zn_{0.4}La_{2y}Fe_{2-2y}O_4$ ferrite system

The variation of log of dc electrical resistivity (log$\rho_{dc}$) as a function of inverse of temperature (1000/T) for various composition of $Mg_{0.6}Zn_{0.4}La_{2y}Fe_{2-2y}O_4$ ferrite is shown in Fig.2, The dc resistivity of the ferrites gets decreased with an increase in temperature indicates semiconducting behavior of the ferrites. All the samples show the break at Curie temperatures due to the change in conduction mechanism [12]. The slope change at Curie temperature corresponds to the samples transform from an ordered ferrimagnetic state to disordered paramagnetic state [13]. The value of Curie temperature obtained from the graph of log$\rho_{dc}$ verses 1/T is calculated. The Curie temperature decreases with increase of $La^{3+}$ content. It is due to the nonmagnetic nature of $La^{3+}$ ions, which may break linkage between magnetic cations [14]. Rare earth $La^{3+}$ ions have a strong preference to occupy on octahedral site and therefore replace $Fe^{3+}$ ions at octahedral site (B) in spinel lattice by $La^{3+}$. Upon increase in the $La^{3+}$ ions in B-site, A-B interaction weakens. Thus the decrease in Curie temperature is probably due to weakening of the A-B interaction. Similar observations have also been reported by Patil et al. [15]. The conduction phenomenon in polycrystalline ferrites was explained on the basis of Verwey and de Boer mechanism [16]. The conduction in ferrites is due to hopping of electrons between $Fe^{2+}$ and $Fe^{3+}$ ions on the octahedral (B) sites. In addition of lanthanum in Mg-Zn ferrite, it found that, $Zn^{2+}$ ion have strong tendancy to occupy A-site and $Mg^{2+}$ ion have strong preference to occupy B-site, While $La^{3+}$ preferencelly occupy to octahedral B site, where it replaced $Fe^{3+}$ ions in the B-site as per the modified cation distribution in magnetic study. The resistivity of the ferrite is controlled by $Fe^{3+}$ concentration on B-site. The increase in resistivity with $La^{3+}$ content is due to overall decrease in $Fe^{3+}$ ions concentration on B-site. It causes decrease in hopping of electrons between $Fe^{2+}$ and $Fe^{3+}$ ions, results in decrease in conduction in ferrite with increase of resistivity [17]. Several researchers have been reported that resistivity of ferrites increases with the substitution of rare earth [18]. Gul and Ahmed also reported the effect of grain size, porosity and grain boundary area on resistivity of ferrite [19]. It is found that one of the factors for higher resistivity in ferrite is the decrease in grain size upon the addition of lanthanum. Smaller grain size produces larger number of insulating grain boundaries which produces inhomogeneous structure and greater energy is required for electron conduction which affects on AC and DC resistivity of ferrites [20].

## IV. CONCLUSIONS

In conclusion, we report the preparation of lanthanum substituted magnesium zinc ferrites by co-precipitation method. A study on DC resistivity shows all sample have semiconducting behavior and break at Curie temperature. The conduction phenomenon in polycrystalline ferrites was explained on the basis of Verwey and de Boer mechanism. The increase in DC resistivity is due to low concentration of $Fe^{2+}$ ions, which is responsible for decrease in electronic polarization. The increase of dc resistivity with La content was mainly attributed to decreases in drift mobility with lanthanum content. This study reveals that Lathanum substitution alters the structural and electric properties of Mg-Zn ferrites.

## V. REFERENCES

[1]. M. Kaur, B.S. Randhawa, J. Singh, D. Utreja , Thermolysis studies on magnesium zinc bis(citrato)ferrate pentahydrate precursor for synthesis of ferrite nanoparticles, J. Ceramics Int., 39 (2013) 325-328.

[2]. V. Provenzano, & R. L. Holtz, Nanocomposites for high temperature applications. Mat.Sci. and Eng. A, 204(1-2) (1995)125-134.

[3]. S. R. Hoh, “Evaluation of High Performance Core Materials”, Tele. Tech. 2 (1953) 86.

[4]. E.W. Lee, Soft magnetic material, Advances in Physics, 8 (1959) 292.

[5]. E.E. Richards and A.C. Lynch, “Soft Magnetic Materials for Telecommunications”, Pergamon Press Ltd. (1953).

[6]. A. Sharma, K.S. Pallavi, R. Sharma, “Optical Properties of Tin Oxide Nanoparticles”, ISST Journal of Applied Physics, 2(2)(2011) 13-14.

[7]. R. A. Bugad, T. R. Mane, B. B. Navale, J. V. Thombare, A. R. Babar, B. R. Karche, Structural, morphological and compositional properties of La3+ substituted Mg-Zn ferrite interlocked nanoparticles by co-precipitation method, J. Mater. Sci.: Mater. Electron. 28 (2017) 1590-1596.

[8]. S. E. Shirsath, B. G. Toksha, K. M. Jadhav, Structural and Magnetic properties of La^(3+) substituted NiFe2O4, Mater. Chem. Phys. 117(2009)163-168.

[9]. A. Gadkari, T. Shinde, P. Vasambekar, Influence of rare-earth ions on structural and Magnetic properties of CdFe2O4, Rare Metal, 29(2) (2010)148.

[10].Y. K. Dasan, B. H. Guan, M. H. Zahari, L. K. Chuan, Influence of La^(3+) substitution on structure, Morphology and Magnetic properties of Nanocrystalline Ni-Zn ferrite, PLoS ONE 12(1) (2017)75.

[11].M. Soka, M. Usakova, R. Dosoudil, E. Usak, J. Lokaj, Effect of lanthanum substitution on structural and magnetic properties of nickel zinc ferrites, AIP Advances 8 (2018) 047802.

[12].D. Ravinder, B. Ravikumar, A study on elastic behaviour of rare earth substituted Mn–Zn ferrites, Mater. Lett. 57 (2003) 4471-4473.

[13].A.A. Sattar, Egypt., Temperature Dependence of the Electrical Resistivity and Thermoelectric Power of Rare Earth Substituted Cu-Cd ferrite J. Sol., 26(2003)113.

[14].A. I. Ali, M. A. Ahmed, N. Okashad, M. Hammam, J. Y. Son, Effect of the La3+ ions substitution on the magnetic properties of spinal Li-Zn-ferrites at low temperature, J. Mater. Res. Technol. 2 (2013) 356–361.

[15].S. B. Patil, R. P. Patil, J. S. Ghodake, B. K. Chougule, Temperature and frequency dependent dielectric properties of Ni–Mg–Zn–Co ferrites, J. Magn. Magn. Mater. 350 (2014) 179-182.

[16].E. J. W. Verwey, F. de Boer and J.H. Van Santen, Cation Arrangement in Spinels, J. Chem. Phys. 16 (1948) 1091.

[17].K. Torkar & O. Fredriksen, The effect of grain size on saturation magnetization of barium ferrite powders, J. Powder Metallurgy, (2014) 105-107.

[18].G. L. Sun, J. B. Li, J. J. Sun, X-Z Yang, The influences of Zn2+ and some rare-earth ions on the magnetic properties of nickel–zinc ferrites, J. Magn. Magn. Mater. 281 (2004)173.

[19].I. H. Gul, W. Ahmed and A. Maqsood, Electrical and magnetic characterization of nanocrystalline Ni–Zn ferrite synthesis by co-precipitation route, J. Magn. Magn. Mater. 320 (2008) 270-275.

[20].T. J. Shinde, A. B. Gadkari, P. N. Vasembekar, Effect of Nd3+ substitution on structural electrical properties of nanocrystalline zinc ferrite, J. Magn. Magn. Mater. 322(2010) 2777–2781.

International e-Conference on Recent Trends in Nano-Materials and Its Applications
In Association with International Journal of Scientific Research in Science and Technology
Volume 9 | Issue 11 | Print ISSN: 2395-6011 | Online ISSN: 2395-602X (www.ijsrst.com)

# Self-Focusing of Gaussian Laser Beam in Collision less Plasma with Linear Absorption

**K.Y. Khandale[1], P.T. Takale[1], T.U. Urunkar[1], S.S. Patil[2], P.P. Nikam[2], M.B. Mane[2], V.S. Pawar[2], S.D. Patil[2], M.V. Takale[1]**

[1]Department of Physics, Shivaji University, Kolhapur 416 004, Maharashtra, India
[2]Department of Physics, Devchand College, Arjunnagar, Kolhapur 591 237, Maharashtra, India

## ABSTRACT

In the present work, authors have studied the effect of linear absorption on the self-focusing of Gaussian laser beam propagating in the collisionless plasma. The non-linear dependence of the dielectric constant inside collisionless plasma is mainly due to the ponderomotive force. The field distribution in the medium is expressed in terms of linear absorption coefficient as well as beam-width parameter. By following Akhmanov's parabolic equation approach under Wentzel-Kramers-Brillouin (WKB) approximation and Paraxial approximations, the differential equation is set up for the beam width parameter f which is solved numerically. It is noticed that the absorption coefficient plays an important role in propagation of Gaussian laser beam in collisionless plasma. The graphical results are presented and are discussed at the end.

**Keywords:** Gaussian laser beam, Collisionless Plasma, Linear absorption, Self-focusing.

## I. INTRODUCTION

With the invention of laser nearly six decades (1960-2020) ago, a fascinating new field of research known by the name "Nonlinear Optics" is introduced to the scientific community. Nonlinear optics has its origin when researchers P.A. Fraken and his co-workers in 1961 noticed that a weak optical signal at 3472 Å could be generated in quartz crystal when the material is illuminated with a high power Ruby laser at 6943 Å on optical second-harmonic generation in 1961 the theoretical work of J.A. Armstrong and his co-workers on optical wave mixing in 19621–3. Self-focusing is one of the phenomena in which the intense beam of laser light incident on material medium changes the optical properties in such a way that beam comes to focus within the medium. There are three major mechanisms that lead to a change in the dielectric constant of plasma in laser-plasma interaction, as follows: (i) the relativistic effect (ii) the collisional and (iii) the ponderomotive force4–6.

With the availability of high power laser beams, a large number of interesting nonlinear phenomena have been studied, both theoretically and experimentally. The redistribution of carriers is caused by the pondermotive force and is mainly important in collisionless plasmas. When an intense laser beam propagates through collisionless plasma, the drift velocity of electrons is relativistic so that their mass is intensity dependant but for long pulse experiments, the relativistic effects can be ignored and ponderomotive force of the beam nonlinearity perturbs electron density resulting in the excitation of electron plasma wave7,8. Light absorption has played an important role in studies on the self-focusing of laser beams in different situations. The contribution of light absorption has been ignored in the most of investigations on self-focusing of laser beams in plasmas9–14. Furthermore, Navare et al.15, M. A. Wani et al.16, L. Ouahid et al.17, R. Kashyap et al.18, T. U. Urunkar et al.19, K. M. Gavade et al.20, B. D. Vhanmore et al.21 and S. D. Patil et al.22–25 have investigated the effect of linear absorption on the self-focusing of a Gaussian, Chirped Gaussian, Airy–Gaussian, q-Gaussian, Gaussian, Cosh-Gaussian, elegant Hermite-cosh-Gaussian, Cosh-Gaussian, Gaussian laser beam respectively by considering the different nonlinearities in different situations. The aim of the present investigation is to study the effect of linear absorption on the self-focusing of Gaussian laser beam propagating in the collisionless plasma. The present analysis is carried through parabolic equation approach under WKB and paraxial approximations.

## II. THEORETICAL FRAMEWORK

Consider the propagation of Gaussian laser beam in homogeneous collisionless plasma along the z-direction, initial intensity distribution of Gaussian laser beam at z = 0 can be expressed as

$$\bar{E}\bar{E}^{*} = E_0^2 \exp\left(-\frac{r^2}{{r_0}^2}\right), \qquad (1)$$

where E_0 is the amplitude of Gaussian intensity distribution, r is the radial coordinate of cylindrical coordinate system, r_0 is the initial beam width of the laser beam. The wave equation governing the electric field Ē of the laser beam in homogeneous plasma along with the effective dielectric constant ε, in the cylindrical co-ordinate system is given by,

$$\frac{\partial^2 \bar{E}}{\partial z^2} + \frac{\partial^2 \bar{E}}{\partial r^2} + \frac{1}{r}\frac{\partial \bar{E}}{\partial r} + \frac{\omega^2}{c^2}\varepsilon\, \bar{E} = 0 \qquad (2)$$

When a laser beam propagates through homogeneous gaseous plasma, the effective dielectric constant changes significantly and can be, in general represented as5

$$\varepsilon = \varepsilon_0 + \phi\,(EE^{*}) - i\varepsilon_i\,, \qquad (3)$$

where ε_0= 1-( 〖ω_p〗 ^2/ ω^2 ) is linear part and ϕ is nonlinear part of the dielectric constant, ω_p is the plasma frequency 〖ω_p〗 ^2=(4π n_e e^2/ m_0) , here e, m_0 and n_e are the charge of electron, rest mass of electron and density of plasma electrons in the absence of laser beam respectively and ε_i takes care of absorption. The second term in the equation (3) is the nonlinear dielectric constant for collisionless plasma can be represented as5

$$\phi\,(EE^{*}) = \frac{{\omega_p}^2}{\omega^2}\left[1 - \exp\left(-\frac{3m\,\alpha EE^{*}}{4M}\right)\right], \qquad (4)$$

with $\alpha = \left(\frac{e^2 M}{6\,k_B T_0 \omega^2 m^2}\right)$, where M, m, k_B and T_0 are mass of ion, mass of electron, Boltzmann constant and equilibrium plasma temperature respectively. By using WKB and paraxial approximations the coupled equations in terms of eikonal S and intensity of laser beam A_0^2 can be expressed as

$$2\frac{\partial S}{\partial z}+\left(\frac{\partial S}{\partial r}\right)^2=\frac{{\omega_p}^2}{\varepsilon_0\,\omega^2}\left[1-\exp\left(-\frac{3m\,\alpha EE^*}{4M}\right)\right]+\frac{1}{k^2A_0}\,{\nabla_\perp}^2A_0 \qquad (5)$$

And

$$\frac{\partial A_0^2}{\partial z}+\frac{\partial S}{\partial r}\frac{\partial A_0^2}{\partial r}+\left(\frac{\partial^2 S}{\partial r^2}+\frac{1}{r}\frac{\partial S}{\partial r}-k\frac{\varepsilon_i}{\varepsilon_0}\right)A_0^2=0. \qquad (6)$$

The solution for equations (5) and (6) which satisfies the initial conditions for a Gaussian beam's intensity distribution is as follows:

$$S=\frac{r^2}{2\,f}\frac{\partial f}{\partial z}+\phi(z), \qquad (7)$$

And

$$A_0^2=\frac{E_0^2}{f^2}\exp\left(-\frac{r^2}{{r_0}^2f^2}-2k_iz\right), \qquad (8)$$

where ϕ is the axial phase and k_i is the absorption coefficient. By following the approach given by Akhmanov et al.4 and its simple extension by Sodha et al.5 the dimensionless beamwidth parameter f is obtained as,

$$\frac{d^2f}{d\xi^2}=\frac{1}{f^3}-\frac{3m\,p\,\rho_0\,e^{-\frac{3m\,p\,e^{-2k_i'\xi}}{4Mf}-4k_i'\xi}}{4\,M\,f^3} \qquad (9)$$

where ξ= z/ R_d known as dimensionless distance of propagation, p = αE02 is the initial intensity parameter, R_d=k r_0^2 is known as Rayleigh diffraction length, ρ_0= (ω_p r_0)/c is the normalized equilibrium beam radius and k_i^'=k_i R_d is the normalized absorption coefficient. The equation (9) can be solved numerically with appropriate boundary conditions such as f = 1, ξ=0 and ∂f/∂z=0. By using critical condition in equation (9) one may obtain equilibrium beam radius as follows. Here p is known as critical beam power.

$$\rho_0=\sqrt{\frac{4M}{3m\,p\,e^{-\frac{3m\,p\,e^{-2{k_i}'\xi}}{4M}-4\,{k_i}'\xi}}} \qquad (10)$$

## III. RESULT AND DISCUSSION

Equation (9) is a nonlinear, ordinary second order differential equation which shows the variation of dimensionless beam-width parameter f with respect to normalized propagation distance ξ into the collisionless plasma. First term on the right hand side of the equation (9) is the diffraction divergence which is responsible for defocusing and second term is the convergence arising from the collisionless nonlinearity and also depends on normalized absorption coefficient k_i^' which is responsible for self-focusing of the beam. The equation (9) is a second order nonlinear ordinary differential equation and is solved numerically by choosing following laser-plasma parameters: ω_p= 1.7760 × 1015 rad/s, r_0 = 20 × 10-4 cm, c = 3 × 1010 cm/s, n0 = 1018 cm–3, ρ_0=65, p = αE0 2 = 10, to study the effect of linear absorption on the self-focusing of the beam in collisionless plasma.

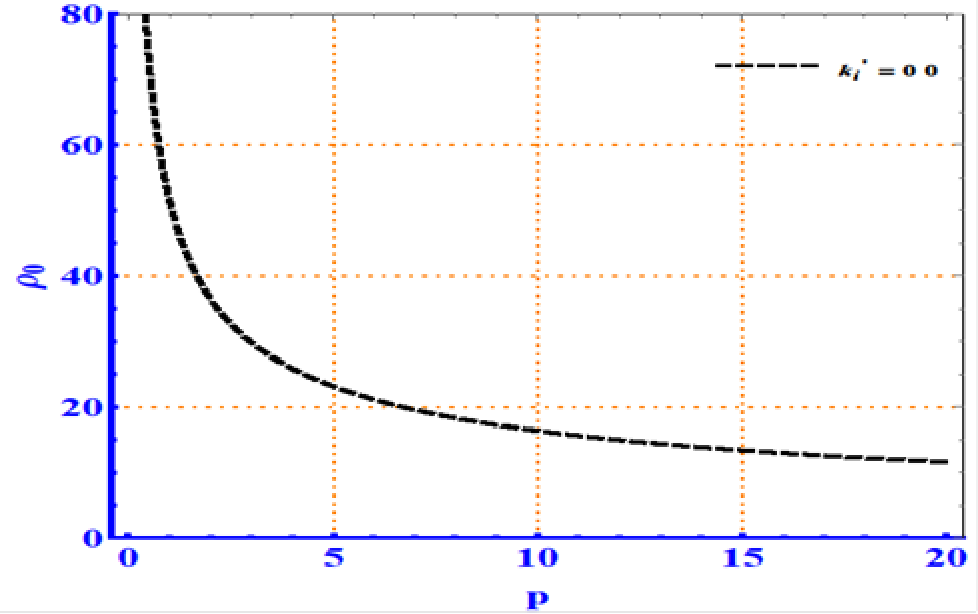

Figure 1: Dependence of normalized equilibrium beam radius ρ_0 as a function of initial intensity parameter p. ω_p = 1.7760 × 1015 rad/s, r_0 = 20 × 10-4 cm, n0 = 1018 cm−3, ρ_0=65, p = αE0 2 = 10.

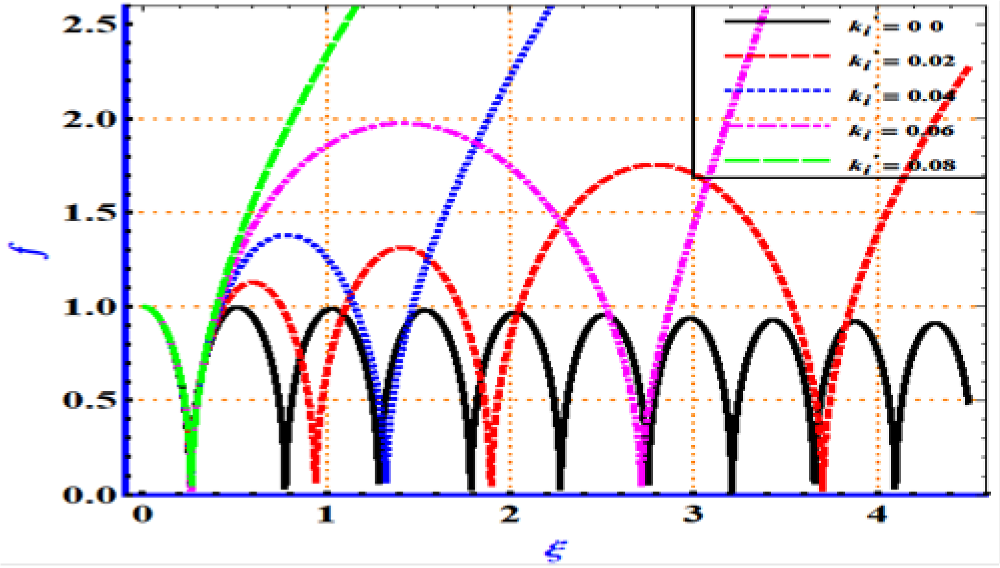

Figure 2: Variation of beam-width parameter f as a function of normalized propagation distance  for different linear absorption coefficients in collisionless plasma (k_i^'=0.00,0.02,0.04,0.06,0.08).

Figure 1 shows critical curve which is plotted from Equation (10). In figure 1 three distinct regions are observed. The region above the critical curve (supercritical region) corresponds to self-focusing region while the region below the critical curve (subcritical region) corresponds to defocusing region and for any point on the critical curve the self-trapping of the laser beam is observed. Figure 2 shows the variation of beam-width parameter f as a function of normalized propagation distance  for different absorption coefficients in collisionless plasma (k_i^'=0.00,0.02,0.04,0.06 and 0.06). In figure 2 for k_i^'=0.00, i.e. in the absence of linear absorption, the oscillatory self-focusing of the laser beam in collisionless plasma is observed. By taking into consideration the absorption, the self-focusing of the laser beam gets destroyed. As a result, the linear absorption defeats the effect of self-focusing, and the beam subsequently becomes too weak to control diffraction, resulting in quick divergence due to high energy attenuation. The longer propagation of laser beam in plasmas decreases due to absorption. In presence of absorption alone the energy of the beam decreases as 〖 exp〗 ⁡(- 2k_i z), which is equivalent to a weakening of the nonlinearity effect.

## IV. CONCLUSION

We have studied the effect of linear absorption on the self-focusing of Gaussian laser beam propagating through collisionless plasma by using parabolic equation approach under WKB and paraxial approximations. The following important conclusions are drawn from the present analysis:

- In the propagation dynamics of the laser beam in collisionless plasma, the controlling factors such as linear absorption coefficient, equilibrium beam radius, and initial intensity parameter play a vital role.
- With an increase in linear absorption in collisionless plasma, the self-focusing effect weakens.

The present results are of importance in various laser-plasma applications, where propagation of laser beam with confined energy over several Rayleigh lengths is required.

Acknowledgement: Authors are thankful to DST-PURSE Phase-II (2018-2023) and UGC DSA -Phase II (2018-2023) Programme for providing research facilities at Dept. of Physics, Shivaji University, Kolhapur, M.S., India.

## V. REFERENCES

[1]. Prof. Franken, P. A., Hill, A. E., Peters, C. W. and Weinreich, G. Phys. Rev. Lett. 7, 118–119 (1961).
[2]. Armstrong, J. A., Bloembergen, N., Ducuing, J. and Pershan, P. S., Phys. Rev. 127, 1918–1939 (1962).
[3]. Sodha, M. S., Ghatak, A. K. and Tripathi, V. K., Tata McGraw-Hill, New Delhi, (1974).
[4]. Akhmanov, S. A., Sukhorukov, A. P. and Khokhlov, R. V. , Sov. Phys. Uspekhi 10, 609–636 (1968).
[5]. Sodha, M. S., Ghatak, A. K. and Tripathi, V. K. , Prog. Opt. 13, 169–265 (1976).
[6]. Nayyar, V. P. and Soni, V. S., J. Phys. D. Appl. Phys. 12, 239–247 (1979).
[7]. Takale. M.V, Navare. S.T, Patil. S.D, Fulari. V.J. & Dongare. M.B, Opt. Commun. 282, 3157–3162 (2009).
[8]. Valkunde. A.T., Vhanmore. B.D., Urunkar. T.U., Gavade. K.M., Patil. S.D. and Takale. M.V., AIP Conf. Proc. 1953, 140088, (2018).
[9]. Sodha. M. S. and Sharma, A., Phys. Plasmas 13, 053105 (2006).
[10].Patil. S.D, Takale. M.V, Fulari. V. J., Gupta. D. N. and Suk. H., Appl. Phys. B Lasers Opt. 111, 1–6 (2013).
[11].Patil, S.D., Takale, M.V., Navare, S. T., Dongare, M. B. and Fulari, V. J., Optik 124, 180–183 (2013).
[12].Patil, S.D. and Takale, M.V. , Phys. Plasmas 20, 072703 (2013).
[13].Patil, S.D. and Takale, M.V., Phys. Plasmas 20, 083101 (2013).
[14].Aggarwal, M., Kumar, H. and Kant, N., Optik 127, 2212–2216 (2016).

[15].Navare. S.T, Takale. M.V, Patil. S.D, Fulari. V.J. & Dongare. M.B, Opt. Lasers Eng.50,1316–1320 (2012).

[16].Wani. M.A. and Kant. N., Commun. Theor. Phys. 66, 349–354 (2016).

[17].Ouahid. L., Dalil-Essakali, L. and Belafhal, A., Opt. Quantum Electron. 50, (2018).

[18].Kashyap. R, Aggarwal. M, Gill. T.S, Arora. N.S, Kumar. H. and Deepshikha. M., Optik 182, 1030–1038 (2019).

[19].Urunkar. T.U., Gavade. K.M., Vhanmore, B.D., Valkunde. A.T., Patil. S.D. and Takale. M.V., AIP Conf. Proc. 2142, (2019).

[20].Gavade. K.M., Vhanmore. B.D., Valkunde. A.T., Urunkar. T.U., Patil. S.D. and Takale. M.V., AIP Conf. Proc. 2142, 110016 (2019).

[21].Vhanmore. B.D., Takale. M.V. and Patil. S.D., Phys. Plasmas 27, 063104, (2020).

[22].Patil. S.D., Navare. S.T., Takale. M.V. and Dongare. M.B., Opt. Lasers Eng. 47, 604–606 (2009).

[23].Patil. S.D., Takale. M.V. and Gill, T.S., Eur. Phys. J. D 69: 163, (2015).

[24].Patil. S.D. and Takale. M.V., AIP Conf. Proc. 1728, 020129 (2016).

[25].Patil. S.D., Valkunde. A.T., Vhanmore. B.D., Urunkar. T.U., Gavade. K.M., Takale. M.V., AIP Conf. Proc. 1953, 140046 (2018).

International e-Conference on Recent Trends in Nano-Materials and Its Applications
In Association with International Journal of Scientific Research in Science and Technology
Volume 9 | Issue 11 | Print ISSN: 2395-6011 | Online ISSN: 2395-602X (www.ijsrst.com)

# Simulations Commercial BJT with Temperature for Space and Radiation Rich Environment Applications

**C M Dinesh[1]*, K S Krishna Kumar[2], M Sathish[3], R. Chandrashekar[1], Shivaprakash Y[4]**
[1]Department of Physics, Govt. First Grade College and PG centre, Chintamani-563125, Karnataka, India
[2]Department of Physics, Raja Rajeshwari College of Engineering, Bengaluru-560074, Karnataka, India
[3]Department of Physics, Govt. First Grade College, Doddaballapur – 561203, Karnataka, India
[4]Department of Physics, Govt. First Grade College, Devanahalli – 562110, Karnataka, India

## ABSTRACT

The temperature variations on electronic circuits employed to onboard plays a significant impact. In this investigation silicon NPN BJT response to irradiation has been studied at room temperature and temperature variation. A temperature variation dependent analytical model for total ionising dose induced excess base current in BJT's is tested. In this model base current dependent on temperature in irradiation parts have been captured. During irradiation all the three terminals of the devices are grounded. After irradiation, the base current is captured and the concentrations of oxide defects like oxide trapped charges and interface traps created during irradiations are calculated using simulated monte-carlo programming. The base current and defect density resulting from room temperature irradiations are used as inputs to simulations and analytical model experimental data obtained from measurements at room temperature and high temperature on irradiation parts are compared with the simulated results. This work shows that the simulations can support qualifications of the chosen devices for space applications and are functional at various temperatures.

**Keywords:** Bipolar Transistor, NPN, Temperature, Total ionizing dose, Base current.

## I. INTRODUCTION

Bipolar circuits used for comparators and regulators used for large percentage of a space system's are important to understand as a part invention. The operation of the components used for these circuits can be significantly degraded by Total Ionizing Dose (TID) [1]. It has been observed that Low Dose Rate (LDR) Irradiation causes more degradation than High Dose Rate (HDR) Irradiation, for the same TID [2]. Space is a Low Radiation Dose Rate (LDR) environment. Since LDR exposures required long test time, part qualification at this rate can introduce prohibitively high costs to mission assurance. Due to this, the identification of numeral models, accelerated techniques, and test method to assist in the characterization of LDR sensitivity in linear bipolar circuits [3] has been proposed. BJT's and Bipolar circuits show degradation mainly due to emitter – base interface traps ($N_{IT}$) and passivation layer oxide trapped charge ($N_{OT}$) defect build up in oxides.

These build up defects in BJTs can increase recombination at the bipolar base surface can lead to an increasing in the base current ($I_B$)[3].

In this paper we describe the temperature dependence of BJTs current voltage characteristics after the irradiation with 108 MeV $Si^{8+}$ ions. We also calculate the defects produced in the irradiation region using Monte-Carlo code (SRIM- Stopping and range of ions in matter). These results has been correlated to electrical degradation.

## II. EXPERIMENTAL METHODS

### BJTs Device and Oxide Defects

The transistors considered for this study are of vertical NPN BJTs the experimental devices were fabricated in BEL (Bharath Electronics Limited, India). Radiation-induced degradation due to defects that build up in base bipolar oxides alter surface recombination, which results in the increase of base current in NPN BJTs. These defects are net positive oxide trapped charge ($N_{DT}$) and interface trap ($N_{IT}$). The data obtained from (SRIM) and data from the transistors were used to extract Non Ionising Energy Loss (NIEL) calculations as a function of TID.

### SRIM Data

**Table 1** SRIM simulated results for 110 MeV Si ion irradiation on silicon target.

| **Parameter** | **Value** |
|---|---|
| R (μm) | 39.62 |
| $S_e$ (MeV cm$^2$/mg) | 10.21 |
| $S_n$ (MeV cm$^2$/mg) | $7.698\times10^{-03}$ |
| NIEL up to R (MeV cm$^2$/g) | 42.67 |

| **Fluence (ions/cm$^2$)** | **$5x10^9$** | **$1x10^{11}$** | **$1x10^{12}$** | **$1x10^{13}$** |
|---|---|---|---|---|
| TID (rad) | 0.8174 | 16.348 | 163.482 | 1634.82 |
| $D_d$ (rad) | 3143.4 | 68268 | $6.8268\times10^5$ | $6.8268\times10^6$ |

Table 1 depicts that the nuclear energy loss of 110 MeV $Si^{8+}$ ion is much smaller than the electronic energy loss (3 orders of magnitude, Table. 1) in a Si-target material due to smaller elastic scattering cross-section. Therefore the maximum energy deposited to the material is expected mainly due to the electronic energy loss during its passage through the Si-material [5]. The device suffers non-uniform irradiation effects as the projected ion range (39.46 μm) is lower than the device thickness (˜ 600 μm) and it is expected to implant at base-collector region. The damage caused due to the linear energy transfer [LET = $S_e + S_n$ ˜ 10.2177 MeV/(mg/cm$^2$)] in the Si target is obtained using TRIM calculations. LET dependent TID and NIEL dependent $D_d$ are tabulated in table 1.

### Pre-and post-irradiation test results

Radiation testing was performed at Inter University accelerating Centre (IUAC) New Delhi, India. Three devices were irradiated at room temperature (RT) LDR irradiation was performed 1PNA (particle nano ampere current) to get desired irradiation fluence. The energy of irradiating ion as choosing so that it could penetrate into emitter base junction.

The fluence has been calculated by counting the charge collected at the Faraday cup placed at the target. The anther advantage of selecting low irradiation current is that BJTs are not damage due to the loss of irradiated ion energy (110 MeV $Si^{8+}$ heavy ion) in the BJTs, (Heating effect will not be produced/the heat produced during the irradiation get transferred to the target).

Figure.1 show the base current $I_B$ responses exposed at 110 MeV $Si^{8+}$ ions for NPN BJTs. The data in these plots were collected at room temperature, 50 and 100 $^0$C. The increase in base current with radiation can be fit approximately to

$$\Delta I_B = I_{SE}\exp\left(\frac{q|VBE|}{n_E\ kT}\right), \qquad (1)$$

Where $I_{SE}$ is the radiation-induced change in low-injection base leakage current, $n_E$ is the change in the low injection ideality factor, k is Boltzmann's constant , T is the junction temperature, and q is the magnitude of electronic charge. Plots of $I_B$ and $V_{BE}$ at constant $V_{CE}$=4V.

**Temperature data on BJT devices**

Figure 1 – 3 shows the temperature dependent base current as a function of base – emitter voltage measured for un-irradiated and irradiated NPN BJTs to characterize the impact of thermal variation prior to and after ionizing radiation dose. The temperature testing was performed approximately 300 months after the radiation tests. No significant change was observed in the electrical response at room temperature between the end of the radiation testing and temperature testing. This showed that the defects produced during irradiations are permanent. Pre- and post unirradiated and irradiated devices were placed in a thermal chamber (hot air oven) with an internal thermocouple to automatically monitor the temperature near the devices during the tests. Temperature response testing was performed from 27 °C up to a maximum temperature of 100 °C in order to avoid annealing effects. Temperatures above 100 °C may lead to the annealing of some oxide defects (both interface and oxide traps) and a reduction in the excess base current measured for BJT [4]. Electrical measurements are performed a few minutes after the temperature is fixed in order to ensure thermal equilibrium during measurement. Each devices has been tested for electrical measurements before and after irradiation in order to test the effect of irradiation, it has been observed all devices show approximately same I-V characteristics before and after irradiation. Hence one devices were tested for each condition, electrical characterization at room temperature were performed after each temperature step in order to ensure no significant temperature dependent annealing of the parts of NPN BJTs [5].

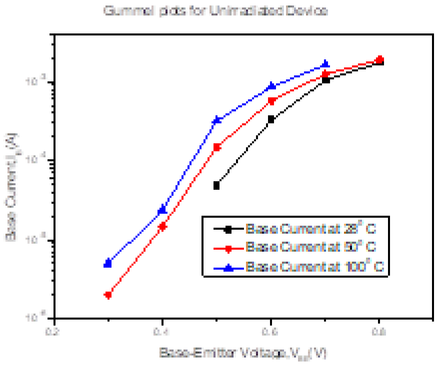

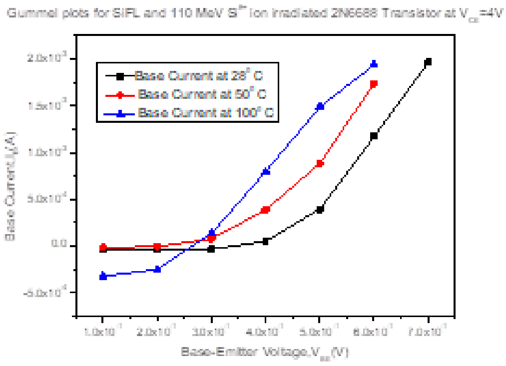

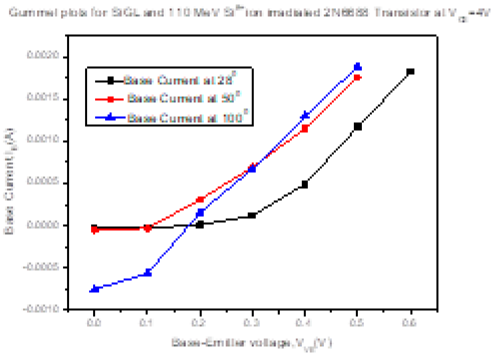

Figure. 1, 2 and 3 show the pre-irradiation, 1×10$^{11}$ and 1×10$^{12}$ ions/cm$^2$ LDR irradiated base currents for NPN BJTs over the specified temperature range (27$^0$, 50$^0$C 100$^0$C).

It can be observed that both the pre- and post-irradiated PNP BJTs show similar trends, i.e., a monotonic increase in base current with increasing temperature. Similar trend can be observed for the pre- and post-irradiated NPN BJTs. Most of the earlier studies have indicated that the impact of displacement damage is marginal compaed with the total dose effect. However, it has been shown that total – dose irradiation may indirectly affect the silicon substrate by reducing the active p-type base dopant concentration, may lead to an increase in base current as shown in figure 4.

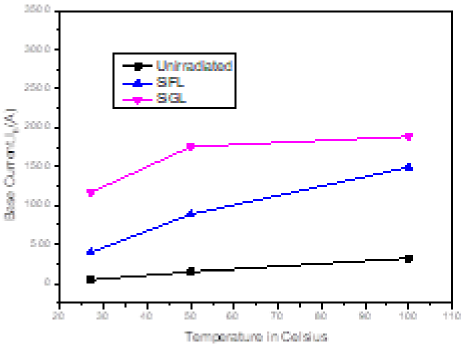

Figure. 4 show the base currents at $|VBE|$ = 0.5 V as a function of temperature for un-irradiated and irradiated NPN BJTs respectively.

Table 2: Variation in base current, $I_B$ of BJT tested for different fluence of 110 MeV $Si^{8+}$ ions at specified temperature range ($27^0$, $50^0$C $100^0$C)

| **Temperature** | | **$I_B$(A)** | | |
|---|---|---|---|---|
| **$^0$C** | **Un irradiated** | **$5\times10^9$** | **$1\times10^{11}$** | **$1\times10^{12}$** |
| **27** | **48.66** | **126.666** | **394.66** | **1165.66** |
| **50** | **147** | **161** | **884** | **1755** |
| **100** | **317.66** | **3200** | **1488.33** | **1885.333** |

The enhabced $I_B$ is related to an increase in the surface recombination velocity, as the density of electrons and holes is coming more comparable, due to base neutralization. From the figure we can also see that there are large increase in the base current tested at higher temperatures ($50^0$C and $100^0$C) due to increased surface recombination current at the base surface. An increase in the midgap-lavel interface-trap density in the low-field, thick oxide over the p-type base increases the recombination current, more importantly an increase in the positive-oxide-charge density modulates the base surface potential to even more strongly increases the surfaces recombination current [6-9].

The current gain of modern bipolar transistors in an ionizing radiation environment decreases due to increased recombination in the emitter-base depletion region [7-8,10-11]. The recombination centers are related to the net charge introduced into the oxide by ionizing radiation, since it is positive the depletion region spreads on the p-side of a PN junction. For NPN transistors, this means that the deplition region seperatres into relatively lightly dopped P-type base region. As the deplition region increases in size, recombination current increases at the oxide interface over the base and in the newly-deplitted silicon bulk. In BJTs the excess basee current depends on the number of interface states (recombination centers) near midgap and threshold. The excess base current due to changes in surface potential depends on the total radiation induced oxide charge at the bias condition these variations in excess base current is as shown in table 2.

## III. CONCLUSIONS

This work reports the effect of 110MeV $Si^{8+}$ ion irradiation on silicon NPN transistors devices with fluences of $5\times10^9$ ions $cm^{-2}$ to $1\times10^{13}$ ions $cm^{-2}$. An effort is made successfully to correlate the electrical degradation with the non –ionizing energy deposition due to MeV ion irradiation using TRIM Monte Carlo Code. Fluence dependent TID and $D_d$is calculated for 100 MeV silicon ion in silicon target. The shift in collector saturation current and collector emitter voltage is mainly due to the total displacement dose. In addition to these shifts, Si-ion irradiation causes increase in forward resistance of the collector emitter region.

The current gain of the transistors decreases with increases in silicon ion fluences. It has in addition been observed that the base current increases with increase in TID and test temperature. The excess base current due to changes in surface potential depends on the total radiation induced oxide charge at the bais condition. This is again related to the reduction of the base doping concentration after exposure. In BJTs the excess base current depends on number of interface traps (recombition centres) near the midgap. At higher total doses, sufficient charge as the accumulated in the oxide to cause significant recombination to occur through-out the lightly doped based region. The swift heavy ion irradiation on silicon will result in increase in lattice temperature. Hence in the present device case the transistor performance is severely affected due to silicon ion irradiation. The switching time of the transistor may decrease due to an increased base currents as a function of silicon ion fluence.

## IV. REFERENCES

[1]. H.J. Barnaby, R.D. Schrimpf, R.L. Pease, P Cole, T.Turflinger, J.Krieg, J.T.Titus, D. Emily, M. Gehlhausen, S.C. Witczak, M.C. Maher, D.Van Nort, Identification of degradation mechanisms in a bipolar linear voltage comparator through correalation of transistor circuit response, IEEE Trans, Nucl. Sci. 46(6)(Dec.1999) 1666-1673.

[2]. A.H. Johnston, B.G. Rax, C.I. Lee, Enhanced damage in linear bipolar integrated circuits at low dose rate, IEEE Trans. Nucl.Sci. 42(6)(Dec 1995)1650-1659.

[3]. P.C. Adell, R.L. Pease, H.J. Barnby, B.Rax, X.J. Chen, S.McClure, Irradiation with molecular hydrogen as an accelerator total dose hardness occurrence test method for bipolar linear circuits, IEEE Trans. Nucl. Sci. 56(6)(Dec.2009) 3326-3333.

[4]. X.Li,W.Lu, Q.Guo, D.M. Fleetwood, C.He, X.Wang, X.Yu, J.Sun, M.Liu, S.Yao, Temperature-switching during irradiation as a test for ELDRS in linear bipolar devices, IEEE trans. Nucl. Sci.66(1)(Jan. 2019)199-206.

[5]. H.J. Barnaby, B.Vermeire, M.J. Campola, Improved model for increased surface recombination current in irradiated bipolar junction transistors, IEEE Trans Nucl. Sci.62(4)(Aug.2015) 1658-1664.

[6]. B.S. Tolleson, P.G. Adell, B.Rax, H.J. Barnaby, A.Privat, X.Han, A.Mahmud, I.Livingston, Improved model for excess base current in irradiated lateral PNP bipolar junction transistors, IEEE Trans. Nucl.sci, Aug,2018.

[7]. C. M. Dinesh, Ramani, M. C. Radhakrishna et al., Nucl. Instr. and Meth. in Phys. Res. B 266, (2008) 1713.

[8]. K.S. Krishnakumar, C.M. Dinesh, KV Madhu, et al., Carbon ion irradiation damage effects on electrical characteristics of silicon PNP power BJTs, IEEE Trans. On Device and Mat. Relia. 15 (1), (2015), 101-108.

[9]. R. Nathan Nowlin, D. M. Fleetwood, and R. D. Schrimpf, IEEE Trans. Nucl. Sci. 41, (6), (1994) 2637.

[10].R. L. Pease, R. M. Turfler, D. Platteter, D. Emily, and R. Blice, IEEE Trans. Nucl. Sci. NS-30, (1983) 4216.

[11].A. R. Hart, J. B. Smyth Jr. V. A. J van Lint, D. P. Snowden, and R. E. Leadon, IEEE Trans. Nucl. Sci. NS-25, (1978) 1502.

[12].J. Boch, F. Faigne, T. Maurel, F. Giustino, L. Dusseau, R.D. Schrimpf, K.F. Galloway, J. P. David, R. Ecoffet, J. Fesquet et.al. IEEE Trans. Nucl. Sci. 49, (3), (2002) 1474.

International e-Conference on Recent Trends in Nano-Materials and Its Applications
In Association with International Journal of Scientific Research in Science and Technology
Volume 9 | Issue 11 | Print ISSN: 2395-6011 | Online ISSN: 2395-602X (www.ijsrst.com)

# Green Synthesis and Characterization of CDS Quantum Dots Mediated by Aegle Marmelos Leaves

**M.D. Dhiware1, T.R. Deore2, S.B. Nahire3, A.B. Gawande2***
[1]Department of Physics, KVNN Arts, Commerce and Science College, Nashik, Maharashtra, India
[2]Department of Physics, K.S.K.W. Arts, Science and Commerce College, CIDCO, Nashik, Maharashtra, India
[3]Department of Physics, National Senior College, Nashik, Maharashtra, India

## ABSTRACT

Herein, we report the green synthesis of CdS quantum dots (QDs) by Aegle Marmelos leaves extract. Green synthesis method is novel, simple, eco-friendly, nontoxic compared to conventional physical and chemical methods. Aegle Marmelos used as a capping and reducing agent owing to their extraordinary medical applications. The synthesized CdS QDs characterized by various characterization techniques Such as X-Ray Diffraction (XRD) showing cubic structure with average particle size about 4 nm determined by using Debye Scherrer formula. Field emission scanning electron microscope (FE-SEM) reveals a spherical shape of CdS QDs.

## I. INTRODUCTION

In past two decades green synthesis method is drawing more attention owing to its facile, nontoxic, eco-friendly and low temperature characteristics compared other methods. Green synthesis approach uses bioactive agents such as plant materials, microorganism and various biogases etc. The various nanomaterials are synthesized by green method such as CdS, $CeO_2$ , Ag, ZnS, SnO2 etc.[1-5]. There are different methods are used for synthesis of CdS QDs by like chemical deposition [6], Hydrothermal [7], Sol-Gel [8], etc. In this method uses the collides with harmful chemicals. These can be avoiding if we used green synthesis plant extract approach.

Cadmium sulfide (CdS) is a direct band gap semiconductor with energy band gap $E_g$ = 2.42 eV. The colour tunability of semiconductor QDs as a function of size is one of their most attractive characteristics. CdS is a promising material because of their applications in optoelectronics, photocatalysts, x-ray detectors, nonlinear optical material and as a window material for hetro-junction solar cells [9].

*Aegle Marmelos* leaves contains broadly alkoids, prphynols, terepnoids and other polyphenols, which are well recognized for their healing power toward variety of bacterial and fungal infections [10]. In the present research work we report green synthesis of CdS QDs mediated by *Aegle Marmelos*.

## II. MATERIALS AND METHODS

Cadmium Chloride ($CdCl_2.H_2O$), Sodium sulphide ($Na_2S.H_2O$) and Ethanol are easily available commercial materials. *Aegle Marmelos* leaves were gathered from local trees. Distilled water used as solvent in the method.

### 2.1 Synthesis of CdS QDs:

CdS QDs synthesized greens approach, typical synthesis in 5 ml extract of *Aegle Marmelos* leaves added 90 ml of distilled water in the proceeding step 0.2 gm of $CdCl_2$ was added and placed on hot plate with magnetic stirring at temperature 100°C for 2 hrs. After that 0.078 gm of $Na_2S$ was added in the mixture and again kept for constant magnetic stirring for 2 hrs. Then final yellow colour product was filtered, centrifuged and finally dried at room temperature 12 Hrs. The final yellow powder was used for further characterisation.

## III. RESULT AND DISCUSSION

### X-ray Diffraction (XRD):

XRD pattern as shown in the figure 1. X-ray diffraction used to study crystal structure, nanoparticle size, interplanar spacing. The XRD peaks was found to be very broad which indicates formation of very small size QDs The diffraction peaks assigns at $2\theta = 26.9^\circ$, $46.78^\circ$ and $53.5^\circ$ which corresponds to the miller indices for the crystal plane of (111), (220) and (311) with cubic crystalline structures of synthesized CdS QDs, respectively, (JCPDS Card no.00-010-0454). XRD of prepared sample materials was found to be in good agreement with (JCPDS file no.00-010-0454). The average particle size was found to be 4 nm which was determined by using the Debye Scherrer formula i. e. nanoparticle size (D) = (k λ)/ (dcosθ) Where, D is the particle in nm, K is crystallite shape factor a good approximation is 0.9 for spherical shape nanoparticles, λ is the X-ray wavelength used for X-ray diffraction, d is the full width at half the maximum (FWHM) in radians of the X-ray diffraction peak and θ is the Braggs' angle (deg.). [11]

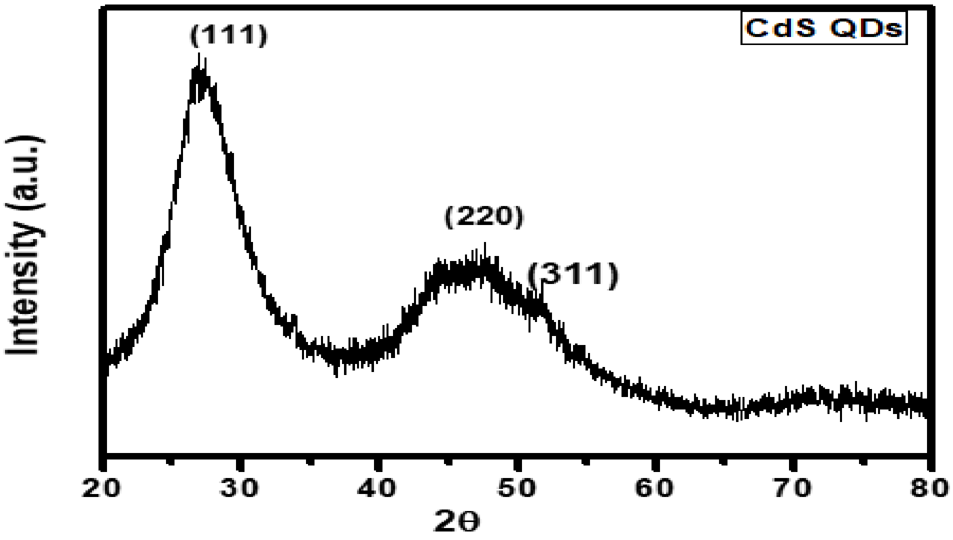

Figure 1: XRD pattern of CdS QDs

**Field Emission Scanning Electron Microscope (FESEM) study:**

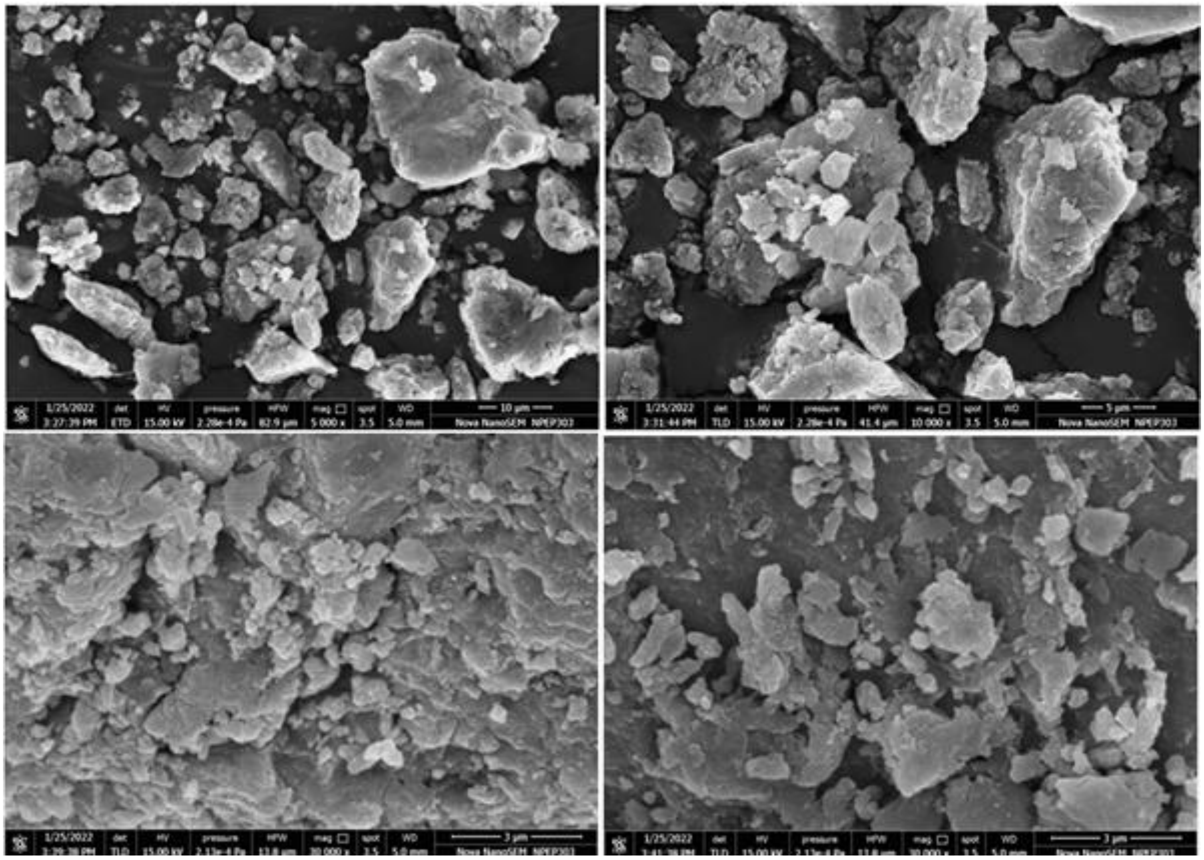

Figure 2: FESEM images of CdS QDs

The synthesized product of CdS QDs characterized by using FESEM technique which is used for the study of surface morphology. CdS QDs shows particles are nearly spherical in shape morphology with slightly agglomeration as shown in the figure 2.

## IV. CONCLUSION

In summary, plant mediated synthesis of nanoparticles have several advantages over physical and chemical methods..CdS QDs synthesized by green synthesis method with leaves extract of *Aegle Marmelos*. The leaves extract bioactive components play vital role for formation of CdS QDs Moreover, the prepared CdS QDs average nanoparticle size was found to be 4 nm determined by using XRD technique. Field emission scanning electron microscope (FE-SEM) reveals a spherical shape of CdS QDs with agglomerate morphology and. Synthesized CdS QDs can be explored for various biomedical applications such as antibacterial, antibiofilm, antifungal, antiviral, anticarcinogenic and anticandidal activities.

## V. ACKNOWLEDGEMENTS

Authors thanks to Principle, KSKW Arts, Science and Commerce College, Nashik for providing instrumental facilities to carry out this research work and Authors also wants to thanks to Vice Principle Dr. Latesh Nikam from Baburanji Gholap College, Sangvi, Pune for providing characterization facility.

## VI. REFERENCES

[1]. Prof. Biogenic synthesis of photocatalyic activity of CdS NPs, A. Bhadwal, et al. , RSC. adv, 2014,4,9484.

[2]. Green synthesis of CeO2 NPs from the abelmoschus esculentus Extract of antioxidant, Anticancer ,Antibacterial and wound- Healing Activities. H. E. Ahemad, et al. Molecules 2021,26,4659.

[3]. Green synthesis of silver NPs using white sugar, S. Mesharam , et al. IET Nanobiotechnology (2013), 7,1, 28-32.

[4]. Green synthesis of ZnO Using S.Frutesences Plant extract for photocatalytic degradation of dye and antibiotics S. Munjai, et al. Mate Res Express, 9, (2022), 015001.

[5]. Green synthesis of SnO2 NPs using delonaelataleaf: Evaluation of its structural, optical, morphological and photocatalytic properties. K.C.Suresh et al, SN applied science (2020)2:1735.

[6]. Photoaucstic study of CdS QDs for application in QDs sensitized solar cells. S. Abdallah, et al., Journal of nanomaterials,498286,1-6, 2012

[7]. One step of hydrothermal synthesis of thioglycolic acid capped CdS QDs as fluroscsnces determination of cobalt ion, Z. wang, et al Scientific Reports, (2018) 8:8953.

[8]. Sol Gel synthesis, characterization and effect of CdS nanoparticles on activity of liver Enzymes, Asmaa. J Al-lamei, Journal of Advanced Sciences and Engineering Technologies, 2019, 35-42.

[9]. W.V. Huynh, J.J. Dittmer, A.P. Alivisatos, "Hybrid nanorod-polymer solar cells", Science 295 (2002), 2425–2427.

[10].One-step biofabrication of copper nanoparticles from Aegle marmelos correa aqueous leaf extract and evaluation of its anti-inflammatory and mosquito larvicidal efficacy, Gangadhara Angajala, Pasupala Pavan and R. Subashini, RSC Adv., 2014, 4, 51459.

[11].Room Temperature Synthesis And Characterization Of Cadmium Sulphide (CdS) Semiconductor Quantum Dots, S.I. Khan, G.K.Kande, L.D.Sonawane, A. S. Mandawade, L.J. Jondhale, P.G.Loke, Journal of Scientific Research in Science and Technology,9,2, 2021.

International e-Conference on Recent Trends in Nano-Materials and Its Applications
In Association with International Journal of Scientific Research in Science and Technology
Volume 9 | Issue 11 | Print ISSN: 2395-6011 | Online ISSN: 2395-602X (www.ijsrst.com)

# Electrodeposited Nanoleaves (NLs) like $Mn_3O_4$ thin film for electrochemical supercapacitor

**P. M. Kharade[1*], J. V. Thombare[2], S. S. Dhasade[2], S. D. Patil[3], P.B.Abhange[4], D. J. Salunkhe[5]**

[1]Department of Physics, Shankarrao Mohite Patil Mahavidyalaya, Akluj, Dist-Solapur (MH), India 413101

[2]Department of Physics, Vidnyan Mahavidyalaya, Sangola, Dist-Solapur (MH), India 413307

[3]Department of Physics, Pratapsinh Mohite Patil Mahavidyalaya, Karmala, Dist-Solapur (MH), India 413203

[4]Department of Physics, G.M. Vedak College of Science, Tala, Raigad (MH), India 402111

[5]Nanocomposite Research Laboratory, K.B.P. Mahavidyalaya, Pandharpur, Dist-Solapur (MH), India 413303

*Corresponding Author E-mail:pravink150@gmail.com

## ABSTRACT

In the present study, we report here synthesis and characterization ofmanganese oxide ($Mn_3O_4$) thin films by potentiostatic electrodeposition for supercapacitor application. The structural and surface morphological behaviour of $Mn_3O_4$ thin film were carried out by using X-ray diffraction (XRD) and Scanning Electron Microscopy (SEM) study. The structural study of $Mn_3O_4$ thin film shows hausmannite tetragonal crystal structure. The surface morphological study showed that the formation of nanoleaves (NLs) of $Mn_3O_4$ thin film. The electrochemical supercapacitive performance of $Mn_3O_4$NLs was characterized by using cyclic voltammetry (CV), charging-discharging (CD) and electrochemical impedance spectroscopy (EIS) techniques. The $Mn_3O_4$NLs shows maximum specific capacitance of 460 $F.g^{-1}$ at scan rate 5 $mV.s^{-1}$and 92% cycling stability in 0.5 M $Na_2SO_4$ electrolyte solution. Hence, potentiostatically deposited $Mn_3O_4$NLs is best for energy storage application.

**Keywords:** supercapacitor, electrodeposition, $Mn_3O_4$, XRD, FESEM, CV.

## I. INTRODUCTION

In the 21th century more and more research focused on highly renewable and sustainable energy storage devices. Electrochemical capacitor or supercapacitor have gained more attention due to their excellent electrochemical properties such as, environmental friendly, fast charging and discharging rate, good reversibility, high power density, long cycle life and safety in operation. Due to this features electrochemical capacitor can be used in variety of potential applications such as, memory back up devices, portable electronic devices, hybrid electric vehicles, elevator, forklifts, cranes, lasers and industry [1-4]. The Electrochemical capacitor or supercapacitor mainly categorized into two typesviz, electrochemical double layer capacitor (EDLC) and Pseudocapacitor (PC). In EDLC, charge is stored electrostatistically, i.e charge accumulation takes place at the electrode/electrolyte interface. Example, carbon materials. In pseudocapacitor (PCs) faradic process takes place. Example, conducting polymers and Transition metal oxides (TMOs) etc. Electrode materials used in TMOs are $RuO_2$ [5], $MnO_2$ [6], $Co_3O_4$ [7], NiO [8], $IrO_2$ [9], $Cr_2O_3$ [10] and CuO [11] etc. Among these TMOs, Manganese oxide electrode is widely studied in supercapacitor because of better electrochemical performance, natural abundant, low cost, easy synthesis and non-toxic [12-13]. Manganese oxide also have several oxidation states such as, MnO, $MnO_2$, $Mn_2O_3$ and $Mn_3O_4$ etc. Among these oxides, $Mn_3O_4$ is one of the most stable state of manganese oxide and have attracted considerable attention due to its low cost, environmental friendly, natural abundant and good electrochemical properties [14-15].

Manganese oxide have been synthesized by different physical and chemical methods such as, hydrothermal method [16], co-precipitation method [17], sol-gel method [18], chemical bath deposition method [19], self-reacting microemulsion method [20], sonochemical method [21], electrodeposition method [22], room-temperature solid reaction [23] and SILAR method [24] etc. Among all the various methods, electrodeposition method is one of the best method for synthesis of metal oxides because of low cost, binder free, single step and large scale production. It also leads direct deposition of oxide/hydroxide electrodes on low cost substrates.Nguyen et al. [22] have reported nanoflakes like morphology of $Mn_3O_4$ thin film by cathodic electrodeposition method for supercapacitor application. Yousefi et al. [25] have reported porous nanospheres of $Mn_3O_4$ by cathodic electrodeposition method and studied their electrochemical properties. Porous and nanostructured material is key requirement for electrochemical capacitor because it provides large surface area, shorten the diffusion path of electrons and ions, which promotes the fast insertion and extraction of electrons and ions. Which improves the specific capacitance of the electrode [26].

In the present report, efforts have been taken to study structural, morphological and electrochemical supercapacitive behaviour of potentiostatically deposited $Mn_3O_4$ NLs for supercapacitor application.

## 2. Experimental:

### 2.2 (a) Characterization techniques

The crystal structural study of $Mn_3O_4$ NLs was carried out with the help of XRD using Bruker axes D8 Advance Model with copper radiation ($K_\alpha$ of $\lambda = 1.54$ A°) within 2θ range between 20° to 80°. The surface morphology of$Mn_3O_4$ NLs was carried out by using field emission scanning electron microscopy (FESEM) technique (Model: JSM-6160). The electrochemical supercapacitive study of $Mn_3O_4$ NLs was studied by using CV, GCD and EIS techniques by using electrochemical workstation (CHI 660 A).The electrochemical cell includes three electrode systems. $Mn_3O_4$ NLs was used as a working electrode, graphite was used as a counter electrode and saturated calomel electrode (SCE) was used as a reference electrode. The 0.5 M $Na_2SO_4$ was used an electrolyte solution for overall measurements.

## 3. Result and Discussion

### 3.1 XRD Study:

X-ray diffraction (XRD) techniques have been carried out to examine the crystal structure of the $Mn_3O_4$ NLs. Fig.1 shows the XRD pattern of $Mn_3O_4$ NLs in the 2θ range from 20° to 80°. The observed diffraction peaks indexed in the XRD pattern of $Mn_3O_4$ NLs was well matched with JCPDs card no.89-4837. The XRD study shows hausmannite tetragonal crystal structure of electrodeposited $Mn_3O_4$ NLs. The peak marked with (SS) in the XRD spectrum is due to stainless steel substrate only.

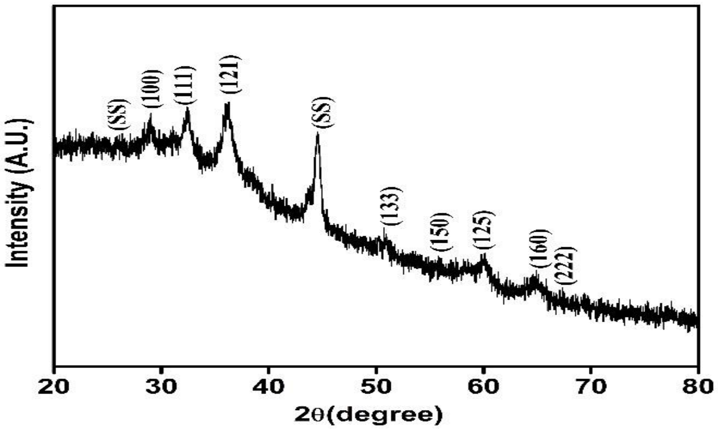

**Figure 1.** X-ray Diffraction (XRD) spectra of $Mn_3O_4$ NLs.

The average crystallite size of $Mn_3O_4$ NLs was calculated by using the Debye's Scherer's equation,

$$D = \frac{0.9\lambda}{\beta\cos\theta} \text{ ------- (3)}$$

Where, D is the crystallite size, λ is the wavelength of X-ray (1.54.4 A°) and β is full width at half maximum (FWHM).For determination of crystallite size, the most intense peak (121) is centered at FWHM in term of radian is 0.807. The crystallite size of $Mn_3O_4$ NLs is found to be 34 nm.

### 3.2. Surface Morphological Studies

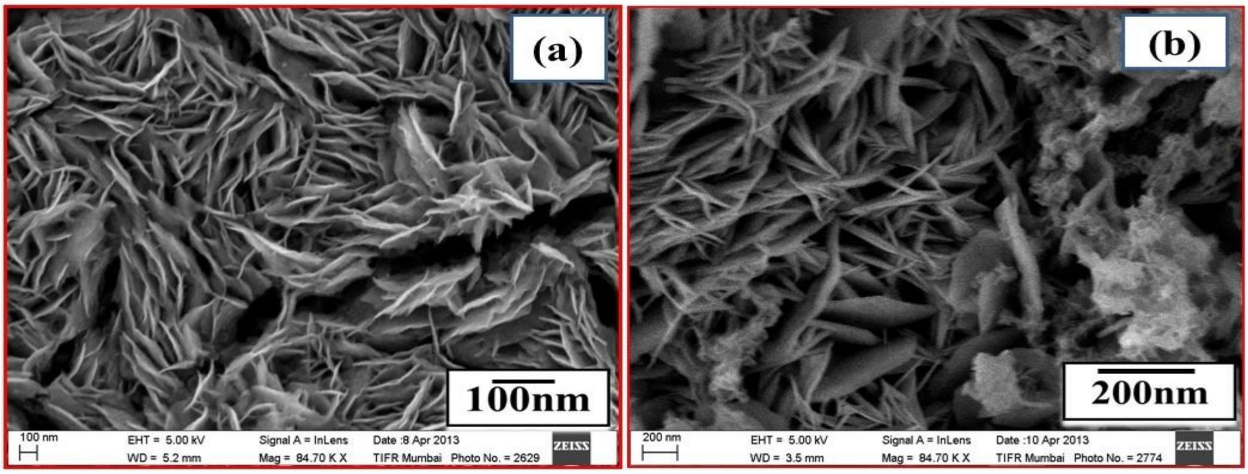

**Figure 2 :** Scanning Electron Microscope (SEM) images of $Mn_3O_4$ thin film at (a) 100kX and (b) 200kX magnifications respectively.

Surface morphology of the $Mn_3O_4$ NLs was studied by using FESEM technique. Fig. 2(a-b) demonstrate the FESEM micrographs of $Mn_3O_4$ thin film with two different magnifications (100 kX and 200 kX) respectively. In Fig. 2(a) SEM micrograph of $Mn_3O_4$ thin film at low magnifications shows the compact and nanoflakes like morphology [28]. At high magnification in Fig. 2(b), the $Mn_3O_4$ thin film gives highly resolved, porous and interconnected Nano leaves (NLs) like structure.Such structures have a larger specific surface area, providing the active material to sufficiently react with ions in the solution, and hence reducing the electron transport distance [29]. Therefore, it enhances the electrochemical supercapacitive properties.

### 3.3 Supercapacitive studies:

### 3.3.1 Cyclic voltammetry (CV) studies:

The specific capacity of $Mn_3O_4$ NLs was carried out by using CV study. Fig. 3(a) display typical CV curves of $Mn_3O_4$ NLs at different scan rates such as; 5, 10, 50 and 100 mV/s within potential limit of +1.2 V to -1.2 V vs SCE, respectively.From CV curves, it is observed that as scan rate increases current under curve increases and the cathodic and anodic peaks shifts more towards positive and negative sideward. This result shows that current is directly proportional to scan rate, i.e. scan rate dependent current-voltage indicate that ideal capacitive behaviour of $Mn_3O_4$ NLs. Similar results reported by Dubal and More et al. prepared by $Mn_3O_4$ thin film by chemical bath deposition and spray pyrolysis method for supercapacitor application respectively [19, 30].

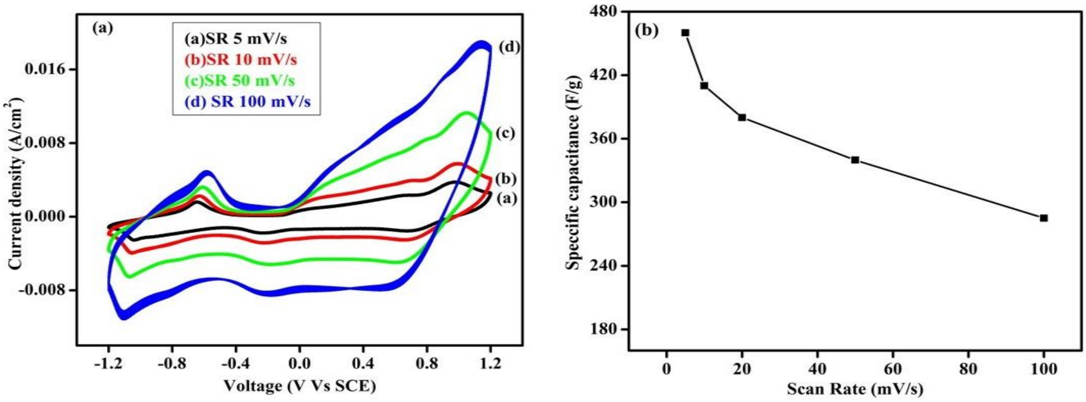

**Figure 3** (a) Cyclic Voltammetry (CV) study of $Mn_3O_4$ NLs at scan rate of 5, 10, 50 and 100 mV/s and 4 (b) Variation of specific capacitance vs scan rate of $Mn_3O_4$ NLs.

The capacitance of $Mn_3O_4$ thin film wascalculated by using the following relation,

$$C = \frac{\int Idt}{dv/dt} \text{ --------- } (4)$$

Where, ∫Idt is area under curve of CV and dv/dt is voltage scanning rate in mV/s.

The specific capacitance of $Mn_3O_4$ NLs was calculated by following relation,

$$\text{Specific capacitance } (C_s) = \frac{C}{W} \text{ ------ } (5)$$

Where, C–capacitance in farad and W – the mass of active electrode materials in gm.The active mass of $Mn_3O_4$ NLs was 0.0024 gm, calculated from weight difference method. The $Mn_3O_4$ NLs show specific capacitance of 460 F.g$^{-1}$ at scan rate of 5 mV.s$^{-1}$. It was observed that as scan rate increases specific capacitance decreases shown in Fig. 3 (b). Decrease in specific capacitance suggests that at higher scan rate most of the inner active sites of nanoflakes network are not involved in the reaction. So, specific capacitance obtained at low scan rate are due to full utilization of the active electrode materials.

| **Material** | **Specific Capacitance (F.g$^{-1}$)** | **Electrolyte** | **Method of synthesis** | **Reference** |
|---|---|---|---|---|
| $Mn_3O_4$ Nano leaves | 460 | 0.5 M $Na_2SO_4$ | Potentiostatic Electrodeposition | Our work |
| $Mn_3O_4$ nanoparticles | 375 | 1.0 M $Na_2SO_4$ | SILAR | [31] |
| $Mn_3O_4$ nanocubes | 223 | 1.0 M $Na_2SO_4$ | CBD | [32] |
| $Mn_3O_4$ nanograins | 314 | 1.0 M $Na_2SO_4$ | SILAR | [24] |
| $Mn_3O_4$ nanograins | 289 | 1.0 M $Na_2SO_4$ | SILAR | [33] |

**Table: 1**Comparison of specific capacitance between our work and previously reported work to synthesis the $Mn_3O_4$ electrodes by considering scan rate of 5 mV/s.

Table 1 represents a comparison of specific capacitance between our work and previously reported work by keeping scan rate of 5 mV/s vs SCE. The specific capacitance obtained in the present study is higher due nanostructured and porous morphology of $Mn_3O_4$ NLs.It depends upon optimum electrodeposition time.

### 3.3.3Galvanostatic charging-discharging (GCD) studies:

The specific energy and specific power associated with $Mn_3O_4$ NLs was carried with the help of GCD techniques. Fig 4 (a) shows typical charge-discharge curves of $Mn_3O_4$ NLs at constant current density of 5 mA.cm$^{-2}$ in 0.5 M $Na_2SO_4$ electrolyte solution. The charging-discharging curves of $Mn_3O_4$ NLs show symmetrical characteristics, which reveals that $Mn_3O_4$ NLsthin film have good capacitive behaviour and the reversible redox process.The GCD curve of $Mn_3O_4$ NLs shows very small voltage drop at the initial of the discharge curve which is due to very low internal resistance between the current collector and $Mn_3O_4$ NLs.

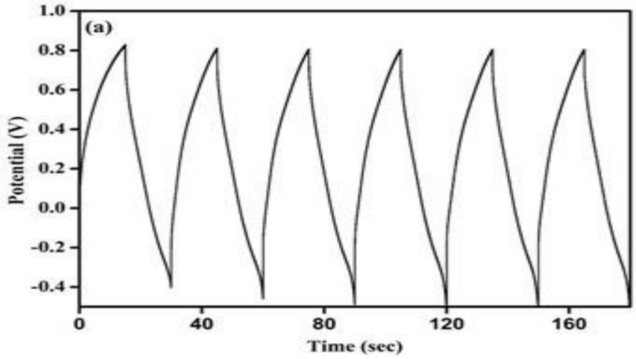

**Figure 4** Galvanostatic charge-discharge (GCD) study of $Mn_3O_4$ NLs

The coulombic efficiency, specific energy and power of $Mn_3O_4$ NLs was calculated using following formulae:

Coulombic Efficiency (η) $= \frac{T_d}{T_c} x100$ ----------- (6)

Specific power (P) $= \frac{V \, X \, I_d}{W}$ ---------------(7)

Specific energy (E) $= \frac{V \, X \, I_d X \, T_d}{W}$ ------------- (8)

Where, $T_d$and $T_c$ is discharge and charge time in sec, V is voltage window in volt, $I_d$ is discharge current mA and W is the mass of the active material in gm.The coulombic efficiency of $Mn_3O_4$ NLs was found to be 98.42% whereas the specific power and specific energy were observed to be 6.40 kW.kg$^{-1}$ and 3.85 Wh.kg$^{-1}$, respectively.

## 4. Conclusions:

In summary, we have successfully synthesized $Mn_3O_4$ NLs by electrodeposition method on low cost conducting stainless steel substrate for supercapacitor application. The XRD study reveals that hausmannite tetragonal crystal structure with average crystallite size of 34 nm. The surface morphology study $Mn_3O_4$ thin film shows NLs type morphology at higher magnification. The electrodeposited $Mn_3O_4$NLsshows higher specific capacitance of 460 F.g$^{-1}$ with 92% cyclic stability, which is better achievement than earlier reported values because of nano structured materials. The GCD study shows better values specific energy and specific power and coulombic efficiency of $Mn_3O_4$NLs. EIS study reveals that small values of $R_s$ and $R_{ct}$ of $Mn_3O_4$NLs based thin film electrode, providing better ability of electronic and ionic conductivity of $Mn_3O_4$materials. Thus, electrodeposited $Mn_3O_4$NLs based thin film electrode is suitable material for electrochemical supercapacitor device.

## References:

[1] G. Wee, W.F. Mak, iN. Phonthammacha, A. Kiebele,M.V. Reddy, B.V.R. Chowdari, G. Gruner, M. Srinivasan,
S.G.Mhaisalkar, J. Electrochem. Soc. 157,A179 (2010)
[2]J.K. Chang, Y.L. Chen, W.T.T.Sai, J. Power Sources. 135,344(2004)
[3] P. Simon, Y.Gogotsi, Nat. Mater. 7,845(2008)
[4]D. Wei, Scherer MR, Bower C, Andrew P, Ryhanen T, U.Steiner, Nano Lett.12,1857 (2012)
[5] K.H. Chang,C.C. Hu,C.Y.Chou, Chem. Mater.19,2112 (2007)
[6]Z. Yu,B. Duong,D. Abbott, J.Thomas, Adv. Mater.25, 3302(2013)
[7] P.M. Kharade, J.V. Thombare, A.R. Babar, R.N. Bulakhe, S.B. Kulkarni, D.J.Salunkhe, J Phys Chem Solids. 120,207(2018)
[8]L. Gu,Y. Wang, R. Lu, L. Guan,X. Peng, J.Sha J. Mater. Chem. A. 2,1761(2014)
[9] D.Q. Liu, S.H. Yu, S.W. Son, andS.K.Joo, ECS Trans.16,103(2008)
[10] P.M. Kharade, A.R. Babar, S.S. Dhasade, B.R. Karche, D.J. Salunkhe, Mater. 7, 342(2018)
[11]A.S. Patil, M.D.Patil, G.M.Lohar, S.T. Jadhav, V.J. Fulari, Ionics. 23, 1259 (2017)
[12] S.F. Chin, S.C. Pang, and M.A. Anderson,J. Electrochemical Society. 149, A379 (2002)
[13]S.F. Chin, and S.C.Pang, Mater. Chem. Phys.124,29 (2010)
[14]X. Zhang, X. Sun,Y. Chen,D. Zhang,Y.Ma, Mater. Lett.68, 336(2012)
[15] X. Zhang, P. Yu, D. Zhang,H. Zhang, X. Sun, Y.Ma, Mater. Lett. **92**401(2013)
[16] J.L. Liu, L.Z. Fan, X.Qu, Electrochim. Acta. 66, 302(2012)
[17] R. Jiang, T. Huang, J. Liu, J. Zhuang, A.Yu, Electrochim. Acta.54, 3047(2009)
[18]C.K. Lin, K.H. Chuang, C.Y. Lin, C.Y. Tsay, C.Y.Chen, Surf. Coat. Technol.202,1272 (2007)

[19]D.P. Dubal, D.S. Dhawale, R.R. Salunkhe, V.J. Fulari, C.D.Lokhande, J. Alloy. Compd. 497,166(2010)
[20] C. Xu, B. Li, H. Du, F. Kang, and Y.Zeng, J of Power Sources.180,664 (2008)
[21] A. Zolfaghari,F. Ataherian, M. Ghaemi, andA.Gholami, Electrochimica Acta. 52,2806(2007)
[22]T. Nguyen, M.J. Carmezim,M. Boudard, M.Montemor, J. Hydrog. Energy. 40,16355(2015)
[23]A. Yuan, X. Wang, Y. Wang, J.Hu, Electrochim. Acta. 54,1021(2009)
[24] D.P. Dubal, D.S. Dhawale, R.R. Salunkhe, S.M. Pawar, C.D. Lokhande,Appl Surf Sci.256,4411(2010)
[25] T. Yousefi, A.N. Golikand, M.H. Mashhadizadeh, M. Aghazadeh,Curr. Appl. Phys. 12, 544(2012)
[26] M. Kim, Y. Hwang, J. Kim,J. Power Sources. 239, 225(2013)
[27] X. Dai, M. Zhang, J. Li, D.Yang, RSC Adv.10, 15860(2020)
[28]P.M. Kharade, S.G. Chavan, D.J. Salunkhe, P.B. Joshi, S.M. Mane, S.B. Kulkarni, J. Mater. Sci. Mater. Elect ron. 52, 37(2014)
[29] M. Zhang, X. Dai, C. Zhang, Y. Fuan, D. Yang, J.Li, Mater.13, 181(2020)
[30] P.D. More, P.R. Jadhav, S.M. Ingole,Y.H. Navale,V.B.Patil, J Mater Sci: Mater Electron. 28,707(2017)
[31] A.A. Shaikh, M.R. Waikar, R.G.Sonkawade, Synth. Met. 247, 1(2019)
[32] D.P. Dubal, D.S. Dhawale, R.R. Salunkhe, C.D. Lokhande,J. Electrochem. Soc. 157,A812 (2010)
[33] G.S. Gund, D.P. Dubal, B.H. Patil, S.S. Shinde, C.D.Lokhande, Electrochim. Acta. 92,205 (2013)

International e-Conference on Recent Trends in Nano-Materials and Its Applications
In Association with International Journal of Scientific Research in Science and Technology
Volume 9 | Issue 11 | Print ISSN: 2395-6011 | Online ISSN: 2395-602X (www.ijsrst.com)

# Investigation The Temperature and Volume Fraction Effects on The Thermal and Rheological Properties of The $TiO_2$ Nanofluid

**N B Girhe[1], S N Botewad[2*], P P Pawar[2], A B Kadam[2]**
[1]Department of Physics, Jawahar Science, Commerce and Arts College, Andoor, Tuljapur 413603, Maharashtra, India
[2]Department of Physics, Dr. Babasaheb Ambedkar Marathwada University, Aurangabad 431004, Maharashtra, India

## ABSTRACT

The present investigation has been reported the preparation of water-based TiO2 nanofluid using a two-step method. The temperature and volume fraction dependent thermal conductivity and viscosity TiO2 was studied. The different volume fraction of TiO2 (0.1,0.2,0.3,0.4 and 0.5) were used dispersed in water using harsh ultrasonic treatment and tested the thermal conductivities for temperature range of 20–50 °C. The experimental results reveal that increase in temperature and volume fraction increases the thermal conductivity of nanofluid. The viscosity of the nanofluid with same concentration of TiO2 was measured and shows the decrease viscosity by increasing temperature whereas increases when increase the volume concentration. Thus, the experimental results are much more useful for the practical application of nanofluids in thermal management.

**Keywords:** Nanofluid; Nanoparticles; Thermal Conductivity; Viscosity;

## I. INTRODUCTION

Thermal management becomes the very critical task in various industries for getting the efficient productivity. Worldwide various conventional fluids were used for the thermal management such as water, oil, ethylene glycol etc. But unfortunately, these fluids do not achieve the desired thermal properties for practical application. To improve the thermal conductivities of these conventional fluids firstly in 1873 Maxwell proposed the single-phase fluids with the addition of solid particles [1]. The idea of Maxwell worked and it improves the thermal properties of the conventional fluids but it has the drawbacks such as sedimentation, clogging and erosion during the flow. After this inventive research idea and experimental results in 1995, Choi introduced the idea of nanofluids with his own experimental results. The nanofluid which solely overcomes the sedimentation, clogging and erosion problems [2].

An emerging nanotechnology provides the superior physical, thermal, optoelectronics properties of the material in nanosized dimension. The very new trending application of nanotechnology is the nanofluid research. Nanofluid is an engineering fluid in which nanometre sized solid particles homogeneously dispersed in base fluid such as water, engine oil, propylene glycol, ethylene glycol, etc [3]. Recently various types of nanomaterials were found to be used for the preparation of nanofluid such as metal, metal oxides, carbon materials etc. Nowadays metal oxide nanoparticles (TiO2, SiO2, Fe2O3, Fe3O4, Al2O3, BaTiO3, CuO, etc.) extensively employed for the preparation of nanofluid [4]. The preference for metal oxide nanoparticles is due to the superior physicochemical, optoelectronics, thermal properties, and ease of preparation with tuned properties. The potential of nanofluids to enhances the thermal conductivity and rheological behaviour of base fluid it applicable in heat transfer, including fuel cells, cooling of microelectronic equipment, pharmaceutical processes and hybrid engines etc [5,6].

Worldwide different research groups have been reported the thermal conductivity and viscosity of the nanofluids using the different types of nanoparticles with different volume fraction in the base fluid. M.Kh. Abdolbaqi et. al studied the thermal conductivity and viscosity of BioGlycol/water based TiO2 nanofluids and experimental results shows that enhancement of thermal conductivity depends on volume concentration, temperature and thermal conductivity of base fluid [7]. M.H. Ahmadi et.al investigate the thermal performance of TiO2 nanofluid using four different neural networks [8]. D. Cabaleiro et.al reported the ethylene and propylene glycol-based $TiO_2$ (anatase and rutile) nanofluids. The experimental results shows that thermal conductivity increases 15.4%. and enhancements are higher for propylene than ethylene glycol-based nanofluids [9]. W.H. Azmi et.al investigate the heat transfer performance of $TiO_2$ nanofluids in water-EG mixture at different operating temperatures. On the basis of experimental results concluded that maximum enhancement of thermal conductivity was 15.4% at 1.5% volume concentration and temperature of $60^0$ C. and relative viscosities fluctuate at a range of 4.6 to 33.3% with variation of temperature [10].

## II. EXPERIMENTAL

### 2.1 Materials and Characterization

In present investigation $TiO_2$ (Rutile) nano particles with particles size 20 nm procured from the Sisco Research Laboratory Mumbai, India. KD2 Pro thermal analyser (Decagan Devices Inc., USA) was use to study the thermal conductivity and before measurements the device prob was calibrated with standard fluid. The viscosity of all nanofluid were measured by means of an AR-G2 rheometer (TA Instruments, USA) at different temperatures.

### 2.2 Nanofluid Preparation

Nanofluids reported in the present investigation were prepared via two-step method. TiO2 nanoparticles of volume fraction (0.1, 0.2, 0.3, 0.4, and 0.5 Wt.%) were used for the preparation of nanofluid. The above-mentioned proportion of $TiO_2$ nanoparticles was dispersed in the base fluid double distilled water (DDW) separately and stirred for 2 hours forcefully using magnetic stirrer. Then the stable dispersion was attained by ultrasonic probe via ultrasonication for 6 h.

## III. RESULTS AND DISCUSSION

### 3.1 Thermal conductivity

The thermal conductivity of prepared water based $TiO_2$–nanofluids concentrations of (0.1, 0.2, 0.3 and 0.4) wt. % were measured at temperatures of 300 K-350 K in 15 k interval. Fig. 1 shows the thermal conductivity of prepared nanofluid for different volume concentrations and fig. 2 shows for different temperatures. It is observed that by increasing both parameters volume concentrations and temperatures, thermal conductivity is enhanced of all the studied samples. Increment of the nanoparticles loading in the base fluid reduces the interparticle distances that improves heat conduction and the outcome is enriched thermal conductivity. The basic phenomenon of the increment in the thermal conductivity is propagation of lattice vibration between electrons and phonons. The thermal conductivity significantly increases by increasing temperatures due to the Brownian motion which provide the direct solid-solid transport between the incorporated particles.

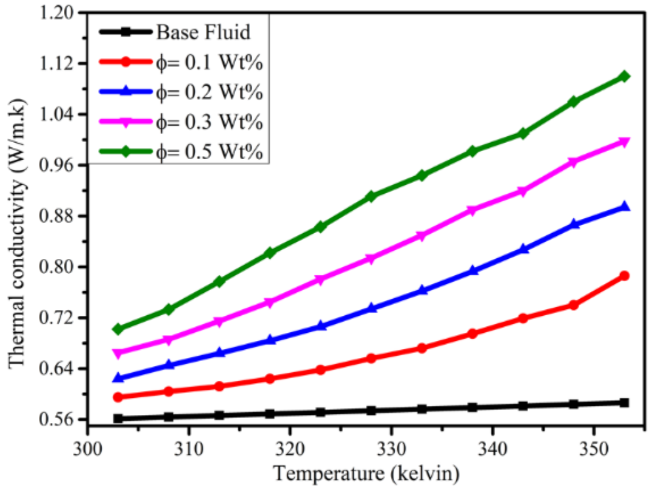

Figure 1. Thermal conductivity for various volume fraction at different temperature

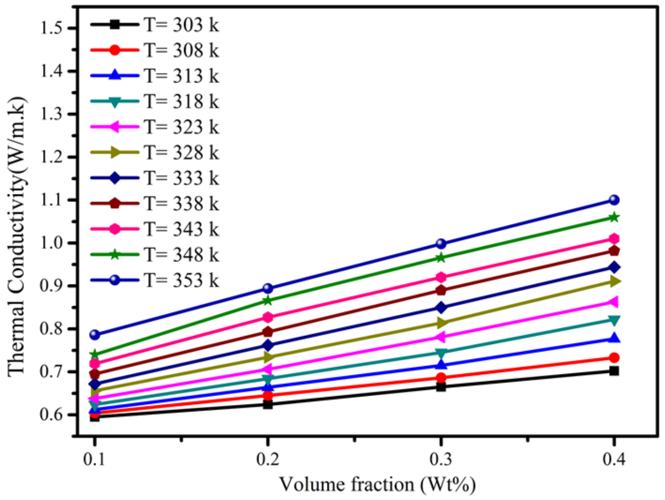

Figure 2. Thermal conductivity for different temperatures of various concentration

### 3.2 Viscosity

Rheological behaviors of all prepared nanofluid samples viscosity were examined at different temperature points of 300 K-360 K at equal interval for each volume concentrations. Fig. 3 shows the dependency of viscosity on the volume concentration and temperature of $TiO_2$ nanofluid. The considerable effects were observed for both parameters, temperature as well as volume concentrations. As concerned to the volume concentration viscosity of all the nanofluid samples observed to be increased. The reason behind the increasing viscosity may be due to the formation of agglomeration of nanoparticles in suspension. The temperature effect slightly reduces the viscosity due to the feeble intermolecular interaction and adhesion forces between molecules which is further attributed to Brownian motion, thermal movement of molecules and their average speed.

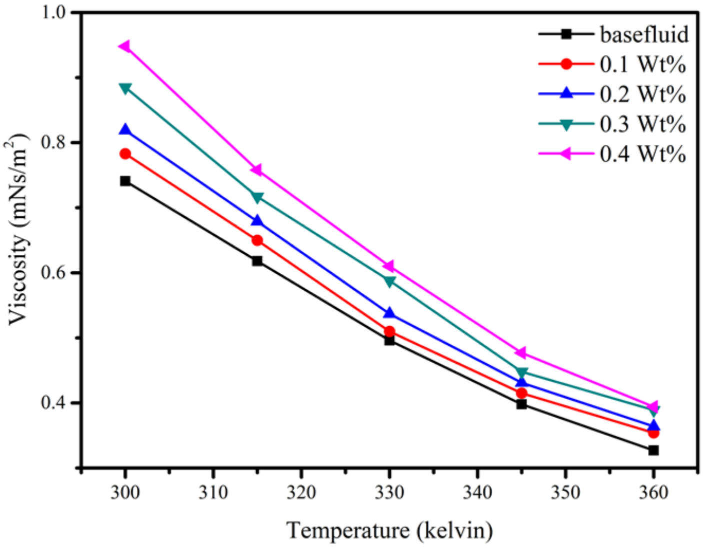

Figure 3. Viscosity of $TiO_2$ nanofluid at different temperature

## IV. CONCLUSION

In short, present investigation successfully encloses the preparation and analysis of the thermal as well as rheological properties of $TiO_2$ nanofluids. The investigational findings reveal the considerable enhanced thermal conductivity of nanofluids with increased temperature and volume concentration. The viscosity of the nanofluid increased with volume concentration whereas decreased with increased temperature. Thus, the present investigation exhibits the applicability of the ternary $TiO_2$ nanofluid for the various application wherever the necessity of cooling.

## V. REFERENCES

[1]. Vanaki, S. M., Ganesan, P., & Mohammed, H. A. (2016). Numerical study of convective heat transfer of nanofluids: a review. Renewable and Sustainable Energy Reviews, 54, 1212-1239.

[2]. Das, S. K., & Stephen, U. S. (2009). A review of heat transfer in nanofluids. Advances in Heat transfer, 41, 81-197.

[3]. Ali, H. M., Babar, H., Shah, T. R., Sajid, M. U., Qasim, M. A., & Javed, S. (2018). Preparation techniques of TiO2 nanofluids and challenges: a review. Applied Sciences, 8(4), 587.

[4]. Sidik, N. A. C., Mohammed, H. A., Alawi, O. A., & Samion, S. (2014). A review on preparation methods and challenges of nanofluids. International Communications in Heat and Mass Transfer, 54, 115-125.

[5]. Puliti, G., Paolucci, S., & Sen, M. (2011). Nanofluids and their properties. Applied Mechanics Reviews, 64(3).

[6]. Suganthi, K. S., & Rajan, K. S. (2017). Metal oxide nanofluids: Review of formulation, thermo-physical properties, mechanisms, and heat transfer performance. Renewable and Sustainable Energy Reviews, 76, 226-255.

[7]. Abdolbaqi, M. K., Sidik, N. A. C., Aziz, A., Mamat, R., Azmi, W. H., Yazid, M. N. A. W. M., & Najafi, G. (2016). An experimental determination of thermal conductivity and viscosity of BioGlycol/water based TiO2 nanofluids. International Communications in Heat and Mass Transfer, 77, 22-32.

[8]. Ahmadi, M. H., Baghban, A., Sadeghzadeh, M., Hadipoor, M., & Ghazvini, M. (2020). Evolving connectionist approaches to compute thermal conductivity of TiO2/water nanofluid. Physica A: Statistical Mechanics and its Applications, 540, 122489.

[9]. Cabaleiro, D., Nimo, J., Pastoriza-Gallego, M. J., Piñeiro, M. M., Legido, J. L., & Lugo, L. (2015). Thermal conductivity of dry anatase and rutile nano-powders and ethylene and propylene glycol-based TiO2 nanofluids. The Journal of Chemical Thermodynamics, 83, 67-76.

[10]. Azmi, W. H., Hamid, K. A., Mamat, R., Sharma, K. V., & Mohamad, M. S. (2016). Effects of working temperature on thermo-physical properties and forced convection heat transfer of TiO2 nanofluids in water–Ethylene glycol mixture. Applied Thermal Engineering, 106, 1190-1199.

IJSRST

# International e-Conference on Recent Trends in Nano-Materials and Its Applications

## RTNA-2022

Organized By
Department of Physics,
Sangola Taluka Shetkari Shikshan Prasarak
Mandal Sangola's, Vidnyan Mahavidyalaya, Sangola
Tal-Sangola, Dist-Solapur, MH-413307, India
Collaboration with
Internal Quality Assurance Cell (IQAC)

**Publisher**

Technoscience Academy

Techno Science Academy
The International Open Access Publisher

Website : www.technoscienceacademy.com

Email : editor@ijsrst.com  Website : http://ijsrst.com